# Nonlinear Modal Substructuring of Geometrically Nonlinear Finite Element Models

by

## Robert John Kuether

A dissertation submitted in partial fulfillment of the requirements for the degree of

#### DOCTOR OF PHILOSOPHY

(Engineering Mechanics)

at the

#### UNIVERSITY OF WISCONSIN-MADISON

2014

Date of final oral examination: 12/11/2014

The dissertation is approved by the following members of the Final Oral Committee:

Matthew S. Allen, Associate Professor, Engineering Physics

Daniel C. Kammer, Professor, Engineering Physics

Melih Eriten, Assistant Professor, Mechanical Engineering

Krishnan Suresh, Associate Professor, Mechanical Engineering

Joseph J. Hollkamp, Senior Aerospace Engineer, Air Force Research Laboratory

© Copyright by Robert J. Kuether 2015

All Rights Reserved

#### Abstract

In the past few decades reduced order modeling (ROM) strategies have been developed to create low order modal models of geometrically nonlinear structures from detailed finite element models built in commercial software packages. These models are capable of accurately predicting responses at a dramatically reduced computational cost, but it is often not straightforward to determine which modes must be included in the reduction basis. Furthermore, much of the upfront cost associated with these reduced models comes from the static load cases applied to the full order model that are used to estimate the nonlinear stiffness coefficients, and this cost grows in proportion to the number of component modes used to capture the kinematics. Hence, there is strong motivation to include only those modes that are absolutely necessary to predict the response. The accuracy of the ROMs and their identified nonlinear stiffness coefficients are also sensitive to the amplitude of these static loads. Typically, these issues are addressed by directly integrating the full model subject to a small number of representative loading scenarios and its response is then compared with that computed by the candidate ROMs to evaluate their accuracy. These strategies have been successfully used for many engineering applications, but the truth data can be prohibitively expensive to compute and it is difficult to ascertain whether the model would work in different loading scenarios. This dissertation proposes contributions to the existing ROM strategies in two ways.

The first contribution is the use of the nonlinear normal mode (NNM) as a metric to gauge the convergence of candidate ROMs and to observe similarities and differences between them. These may be compared with the NNMs computed from the full order model if it is computationally feasible, although these are not necessary. The undamped NNM is defined as a

not necessarily synchronous periodic response to the undamped nonlinear equations of motion. Since geometric nonlinearities depend only on displacements, the undamped NNM framework serves as an ideal metric for comparison since they are load independent properties of the system and capture a wide range of response amplitudes experienced by the structure. While superposition and orthogonality do not hold for NNMs, many existing works have shown that the NNMs are intimately connected to the damped, forced response of the system. If the NNMs of the ROMs converge and coincide with the true NNMs of the full order model over a range of frequency and energy, then the model is at least guaranteed to represent the full order model in a number of important conditions. This validation framework provides the tools and guidelines to create a reduced order model that is orders of magnitude less expensive to integrate for response prediction.

The second contribution of this work is the development of a modal substructuring framework that utilizes the existing ROM approaches for geometrically nonlinear finite element models. Using the proposed approach, one creates a reduced order model of a large, complicated structure by first dividing it into smaller subcomponents. The efficiency of a modal substructuring procedure strongly depends on the type of subcomponent modes used to create each ROM, and this dissertation explores the use of linear free-interface modes, fixed-interface plus constraint modes, and fixed-interface plus characteristic constraint modes. The Implicit Condensation and Expansion method is used to fit each subcomponent model by applying a series of static forces in the shapes of the subcomponent modes and computing the response using the built-in nonlinear static solver in the finite element code. These forces and responses are used to estimate the nonlinear stiffness coefficients in the subcomponent modal model. Then the geometrically nonlinear, reduced modal equations for each subcomponent are coupled by

satisfying compatibility and force equilibrium. Creating a reduced order model with substructuring allows one to build ROMs of simpler subcomponent models that may require fewer modes, and hence fewer static load cases needed to fit the nonlinear stiffness terms. This procedure is readily applied to geometrically nonlinear models built directly within commercial finite element packages, and the nonlinear normal modes of the assembled ROMs serve as a convergence metric to evaluate the sufficiency of the basis used to create them.

## Acknowledgements

First off, I would like to give thanks to my advisor, Prof. Matt Allen, for his guidance and patience during my time as his Ph.D student. He has taught me many valuable lessons in engineering and structural dynamics, and he has been a great example of an honest, hardworking and kind person.

Thank you to my Ph.D committee for taking the time to review the material in this document and for providing feedback. I'd like to extend a special thanks to Dr. Joe Hollkamp for his helpful insight into reduced order modeling and for sharing his computer codes. His guidance was instrumental in the development of this work, and it was a great pleasure to work with him during my time as a student. I would also like to thank Dr. Matt Brake and Dr. Gaëtan Kerschen for arranging for me to work in their laboratories while I pursued my doctorate.

I am grateful for receiving support from an Air Force Office of Scientific Research grant under grant number FA9550-11-1-0035. I am also thankful for the funding I received from the National Physical Science Consortium (NPSC) Fellowship, as well as the J. Gordon Baker Fellowship.

I have had the great pleasure of meeting so many great and talented colleagues throughout the years. These people have helped make my time as a student much more enjoyable, so thanks to all for our informative conversations about research, and the great memories.

Finally I would like to thank my family and loved ones for all their love and support during my time as a student. I am grateful for the countless times we've shared together and I will keep these memories with me for the rest of my life. This work was made possible because of the support from those close to me so I dedicate this dissertation to them with love.

# **Abbreviations and Nomenclature**

#### **Abbreviations**

AMF Applied Modal Force

CB Craig-Bampton

CB-NLROM Craig-Bampton Nonlinear Reduced Order Model

CC Characteristic Constraint

CC-NLROM Characteristic Constraint Nonlinear Reduced Order Model

CPU Central Processing Unit

DOF Degree-of-freedom

ED Enforced Displacement

EMD Enforced Modal Displacement

EOM Equation of Motion

FEA Finite Element Analysis

FEP Frequency-Energy Plot

ICE Implicit Condensation and Expansion

MC Milman-Chu

MIF Mode Indicator Function

NNM Nonlinear Normal Mode

NLROM Nonlinear Reduced Order Model

ROM Reduced Order Model

#### Nomenclature

 $A_r$ ,  $B_r$  quadratic and cubic nonlinear stiffness coefficient, respectively

**B** modal transformation matrix

 $CD_r$  constant modal displacement scaling factor (ED)

*CLD*<sub>r</sub> constant linear displacement scaling factor (ICE)

 $CS_r$  constant modal scaling factor (ED)

 $\mathbf{f}(t)$  vector of external forces

 $\mathbf{F}_c$ ,  $\mathbf{F}_{static}$  vector of static forces  $\mathbf{f}_{NL}(\mathbf{x})$ 

 $\mathbf{I}_{NL}(\mathbf{X})$  vector of nonlinear restoring forces

 $\hat{f}_r$  scaling for the  $r^{th}$  mode using (ICE)

g(t) half-sine pulse

H shooting function

I identity matrix

K linear stiffness matrix

 $\hat{\mathbf{K}}$  reduced stiffness matrix

L connectivity matrix

M linear mass matrix

**M** reduced mass matrix

 $N_1(q)$  quadratic nonlinear modal stiffness matrix

 $N_2(q)$  cubic nonlinear modal stiffness matrix

P tangent prediction vector

**p** vector of generalized membrane coordinates

**q** vector of modal coordinates

 $\mathbf{q}_{u}$  vector of unconstrained coordinates

 $\hat{q}_r$  scaling for the r<sup>th</sup> mode using (ED)

 $\mathbf{r}(t)$  vector of reaction forces

step size controller

T substructure transformation matrix

 $T_m$  matrix of membrane basis vectors

T integration period

 $w_{\text{max},r}$  maximum linear displacement for  $r^{\text{th}}$  mode

 $w_{\text{max},r,NL}$  maximum nonlinear displacement for  $r^{\text{th}}$  mode

 $\mathbf{X}_{\textit{static}}$ ,  $\mathbf{x}_{\textit{static}}$  matrix/vector of static displacements, respectively

 $\mathbf{x}$ ,  $\dot{\mathbf{x}}$ ,  $\ddot{\mathbf{x}}$ displacement, velocity and acceleration vector of static displacements  $\mathbf{X}_c$ ,  $\mathbf{x}_c$ z, ż state space vectors α, β cubic and quadratic nonlinear modal force vectors, respectively ε tolerance of shooting function Φ mass normalized mode shape matrix  $\Phi_{ik}$ fixed-interface mode shape matrix φ mass normalized mode shape vector  $\gamma_r$ ratio of the nonlinear to linear maximum displacement Λ diagonal matrix of fixed-interface modal frequencies  $\theta(q)$ nonlinear modal restoring force  $\theta_r(\mathbf{q})$  $r^{\rm th}$  nonlinear modal restoring force  $\omega_r$  $r^{\text{th}}$  linear natural frequency Ψ constraint mode shape matrix ψ characteristic constraint mode shape matrix  $\Psi_{CC}$ boundary mode shape matrix  $()^T$ transpose operator

# **Contents**

Abst	ract	i
Ackn	owledgements	iv
Abbı	eviations and Nomenclature	V
Cont	ents	viii
1	Introduction	1
1.1	Motivation	1
1.2	Nonlinear Normal Modes	4
1.3	Nonlinear Reduced Order Models	9
1.4	Review of Substructuring Methods	13
1.5	Scope of the Dissertation	16
2	Indirect Computation of Nonlinear Normal Modes	21
2.1	Introduction	21
2.2	Nonlinear Normal Modes of Large Order Systems	23
,	2.2.1 Enforced Modal Displacements (EMD)	24
	2.2.2 Applied Modal Force Method (AMF)	26
2.3	Shooting and Pseudo-Arclength Continuation Algorithm	27
,	2.3.1 Shooting Technique	28
,	2.3.2 Pseudo-Arclength Continuation: Prediction Step	30
,	2.3.3 Pseudo-Arclength Continuation: Correction Step	31
,	2.3.4 Add Linear Modal Coordinate	32
,	2.3.5 FEA-Interface with NNM Algorithm	33
2 4	Application to Clamped-Clamped Beam with Geometric Nonlinearity	35

	2.5	Applic	cation to Exhaust Cover Panel with Geometric Nonlinearity	43	
	2.6	5 Summary			
3	G	eometr	ically Nonlinear Reduced Order Models	50	
	3.1	Introd	uction	50	
	3.2	Reduc	ed Order Model Equations of Motion	51	
	3.3	Identit	fication of Nonlinear Stiffness Coefficients	54	
	3.	3.1	Enforced Displacements Procedure	54	
	3.	3.2	Applied Loads Procedure or Implicit Condensation and Expansion	55	
	3.4	Mode	Selection	56	
	3.5	Scalin	g Factors for Multi-Mode Models	59	
	3.	5.1	Enforced Displacement Scaling Factors	59	
	3.	5.2	Applied Load Scaling Factors	61	
	3.6	Nonlin	near Normal Modes of Reduced Order Models	62	
	3.7	Expan	sion of In-Plane Displacements for Applied Loads	64	
4	C	onverge	ence Evaluation of Monolithic Nonlinear Reduced Order Models	67	
	4.1	Introd	uction	67	
	4.2	Applic	cation to Clamped-Clamped Beam with Geometric Nonlinearity	68	
	4.	2.1	One-Mode NLROMs.	69	
4		2.2	Multi-Mode NLROMs	76	
	4.3	Applic	cation to Exhaust Cover Panel with Geometric Nonlinearity	82	
	4.4	Simply	y Supported Beam with Contacting Nonlinearity	87	
	4.	4.1	Impulse Loading Validation	96	
	4.	4.2	Random Loading Validation	101	

	4.5	Summ	nary	103
5	N	onlinea	r Modal Substructuring	106
	5.1	Introd	uction	106
	5.2	Comp	onent Mode Basis Selection	107
	5.2.1		Free-interface Modes	107
5.2		2.2	Craig-Bampton Modes	108
	5.	2.3	Craig-Bampton Modes with Interface Reduction	109
	5.3	Reduc	eed Subcomponent Models with Geometric Nonlinearity	111
	5.4	Coupl	ing Nonlinear Subcomponent Models	115
6	$\mathbf{A}$	pplicat	ions of Nonlinear Modal Substructuring	117
	6.1	Coupl	ing Two Beams with Geometric Nonlinearity	117
6		1.1	Linear Substructuring	118
	6.	1.2	Nonlinear Substructuring	121
	6.2	Coupl	ing Geometrically Nonlinear Beam to Axial Spring Element	130
	6.3	Coupl	ing Two Plates with Geometric Nonlinearity	135
	6.	3.1	Linear Substructuring	136
	6.	3.2	Nonlinear Substructuring	141
	6.4	Summ	nary	150
7	C	onclusi	ons	153
8	Fu	uture V	Vork	157
	8.1	Substr	ructuring of Thermal-Structural Models	157
	8.2	Mode	l Updating	157
	8 3	Conne	ection Between NNMs and Response Prediction	158

Appendix – Publications of PhD work	. 159
References	. 161

## 1 Introduction

#### 1.1 Motivation

Linear models are often good approximations of realistic engineering structures, however certain cases may require models with nonlinear physics to represent the structure of interest. In certain load environments a system may operate in its "nonlinear" range, so the analytical and numerical models must include the correct physical models in order to make accurate response predictions. A variety of forms of nonlinearity are common in engineering structures, such as geometric nonlinearity [1-4], nonlinear material constitutive laws [5-7], contact [8-11], frictional damping in joints [12, 13], and buckling [14-16], to name a few. This dissertation focuses on structural models with geometric nonlinearities, caused by large deformations, which are frequently encountered in many thin-walled members while the materials remain linear elastic. These types of systems are commonly found in aerospace and aeronautical applications, for example in the design and analysis of reusable hypersonic aircraft [17, 18]. The external skin panels of these high performance vehicles are expected to vibrate nonlinearly with large amplitudes in response to extreme pressure fluctuations caused by air flow and engine noise during flight [19-22]. These panels can also vibrate about a buckled equilibrium state due to aerothermal loads, leading to highly nonlinear behavior.

The finite element method is one analysis technique commonly used in practice to simulate the time response of these geometrically nonlinear panels, and is able to capture detailed geometric features in the model such as stiffeners or curved surfaces. However, modeling the entire nonlinear vehicle structure as a whole would be prohibitively expensive. This is especially true during the engineering design stage where iterations on various

components of the vehicle may be necessary, requiring the responses to be recomputed many times; even design iterations and analysis on a single component are too expensive to be practical. In order to circumvent these CPU costs, often a reduced order model (ROM) is created from the finite element model of interest. The external loads or forces (e.g. from a computational fluid dynamics simulation or flight test data) can be used as inputs to the ROMs, structural damping can be added, and the response to these forces can then be computed at a significantly lower cost than directly integrating the full order model.

A number of methods have been developed over the last few decades to create ROMs of geometrically nonlinear finite element models built directly within a commercial finite element analysis (FEA) software, as reviewed in [19, 23, 24]. These are known as *indirect* methods because they do not require access to the internals of the FEA code. While these modeling approaches have been successful for many applications, this dissertation expands on these existing strategies in two ways. First, this work proposes to validate the ROM of a geometrically nonlinear FEA model based on the convergence of its nonlinear normal modes (NNMs). Second, a nonlinear modal substructuring approach is developed which allows one to divide a large, complicated finite element model into smaller subcomponents, each of which is far simpler and easier to create a ROM from.

The NNMs are essentially defined as periodic solutions of the undamped, unforced nonlinear equations of motion [25-27], and are conceptually similar to the undamped, linear vibration modes used in linear modal analysis. These solutions span a range of response amplitudes experienced by the structure and are independent of any external loads applied to the system. This idea of validating a ROM using NNMs is a significant departure from the standard practice, where the time integrated responses to a given load are used to compare the results

between the ROM and the full order model. The time histories are complex solutions to the nonlinear equations of motion and are difficult to compare with models that have many degrees-of-freedom (DOF). These solutions tend to evaluate the models at only one (or maybe a few) load levels or response amplitudes, and do not provide insight into how the system may respond in different load environments. The NNMs provide insight into the dynamics of the system and offer a convergence metric that can give guidance as to whether or not an accurate ROM has been obtained. This is similar in spirit to the way in which mesh refinement is performed on a linear finite element model, where the natural frequencies are tracked as the mesh is fined and used to assess the convergence of the discretized model [28].

A novel model reduction strategy is developed by taking a substructuring approach to reduce a set of smaller substructure models from a larger finite element model (such as the aircraft assembly in Fig. 1). The subcomponent models are reduced using an indirect approach and then assembled by satisfying force equilibrium and compatibility to generate a global ROM of the assembly that accounts for the effects of geometric nonlinearity. Often the effects of adjacent components are modeled with simple elements at the boundary (e.g. springs with a tuned stiffness), which ignore the possibility of interactions between two or more structures. A substructuring approach has proven to be an effective tool for linear finite element models, but most existing methods do not accommodate systems with geometric nonlinearities distributed throughout the model. To the best of the author's knowledge, this new approach is the first that can address these types of systems. As suggested earlier, the NNMs can then be used to gauge the convergence of these assembled models created with a substructuring approach without the need to run expensive time simulations on the full order model of the assembly; this becomes important as the order of the finite element model of interest increases.

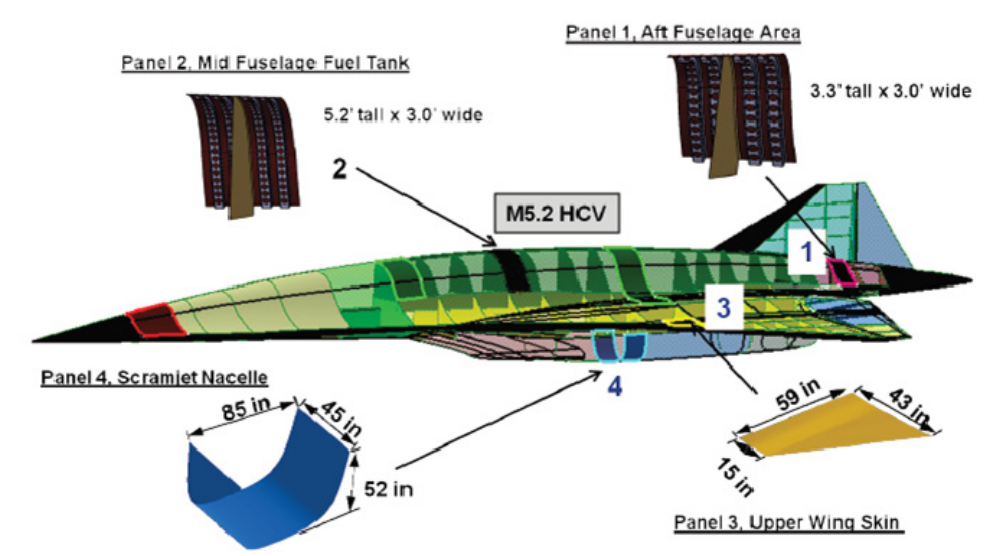


Figure 1. Computer model of the Hypersonic Cruise Vehicle studied in [18].

Since nonlinear normal modes will be used extensively in this dissertation to assess the convergence of candidate reduced order models, the NNM definition used in this work and their properties are reviewed in detail in Section 1.2. The nonlinear reduced order models used throughout are then reviewed in Section 1.3.

## 1.2 Nonlinear Normal Modes

The earliest definition of a nonlinear mode was presented by Rosenberg in 1960 in [29]. He defined the nonlinear mode of a conservative nonlinear system with a symmetric potential function as a periodic motion such that each degree-of-freedom (DOF) of the system passes through the equilibrium position at the same instant in time. This definition was further extended to account for modal interactions, termed internal resonances, by Vakakis, Kerschen, and others [25-27], and is the one used throughout this dissertation. Consider the undamped, *N*-DOF equations of motion of the discretized system in Eq. (1). They defined an undamped, nonlinear normal mode of these equations as a *not necessarily synchronous periodic response*. There exist at least *N* nonlinear normal modes for this *N*-DOF system that capture a branch of solutions that

are extensions of the linearized modes (i.e. by solving  $(\mathbf{K} - \omega_r^2 \mathbf{M}) \mathbf{\varphi}_r$ ) at low energy. Many features emerge with this definition of a vibration mode that cannot be described with linear modal analysis, such as frequency-energy dependence, bifurcations, localization, and modal interactions. It should be noted that other definitions of nonlinear modes exist for damped and undamped systems [30-33], but these are not considered in this work.

$$\mathbf{M}\ddot{\mathbf{x}} + \mathbf{K}\mathbf{x} + \mathbf{f}_{NL}(\mathbf{x}) = \mathbf{0} \tag{1}$$

Modal superposition and orthogonality, two key properties of linear modal analysis, are not applicable to nonlinear modes, however these solutions still provide insight into the physical behavior of a nonlinear system. Take for example the damped, forced, nonlinear equations of motion in Eq. (2). One fundamental property of the undamped NNM is that they can be realized when a harmonic forcing function cancels the damping force in the damped system [34, 35], or when  $\mathbf{f}(t) = \mathbf{C}\dot{\mathbf{x}}$  in Eq. (2). As a result, the NNM forms the backbone of the nonlinear forced response curves [25, 36-39], as shown later in Fig. 3. The NNMs are also intimately connected, qualitatively at least, to the response to transient [40] and random excitation [41], and act as an attractor to the lightly damped free response [25, 26, 42].

$$\mathbf{M}\ddot{\mathbf{x}} + \mathbf{C}\dot{\mathbf{x}} + \mathbf{K}\mathbf{x} + \mathbf{f}_{NL}(\mathbf{x}) = \mathbf{f}(t)$$
(2)

A variety of analytical techniques exist to compute nonlinear normal modes, namely the method of multiple scales [25, 27, 43, 44] and the harmonic balance method [45, 46]. These analytical methods may be restricting in practice since the formulation is mathematically intensive, and requires the equations of motion to be known in closed form. The finite element method allows engineers to model realistic structures within commercial software packages,

where the equations of motion may not be known in closed form. For this reason, a numerical approach to compute the nonlinear normal mode is considered in this work. Slater [47] developed a numerical algorithm that uses time integration, optimization and sequential continuation to track the periodic solutions of the undamped nonlinear system. The initial conditions and period of integration are optimized with a cost function that satisfies the periodicity condition. Another numerical techniques developed by Arquier et al. [48] finds the periodic solutions of a conservative nonlinear system using a global solution technique, rather than shooting, and an asymptotic method as a continuation procedure to predict the next solution along the branch.

Peeters et al. developed an algorithm based on pseudo-arclength continuation and the shooting technique [49], which is capable of capturing modal interactions (or fold bifurcations) along the NNM. This algorithm analytically computes the Jacobian matrix while simultaneously integrating the equations of motion using the approach in [50], and hence it has been successful with structural models having hundreds of DOF [51]. This pseudo-arclength continuation algorithm is used extensively in this work to compute the NNMs of geometrically nonlinear reduced order models whose equations of motion are explicitly known. An extension of this algorithm has been developed by Kuether et al. [52, 53] to compute the NNMs directly from the full finite element model within the native code at a significantly reduced cost. This is a non-intrusive approach because it operates on the input and output of the FEA code and hence it can be used with virtually any code. This algorithm is discussed in detail in Chapter 2, and provides the true NNM of the full order FEA model that will be used later for comparison with the NNMs computed with a set of candidate reduced order models.

In order to demonstrate the concept of the NNM and their connection to the resonance of the harmonically forced response of the damped system, consider the linear cantilever beam model in Fig. 2 with a cubic nonlinear spring attached at the beam tip. This model was studied in detail in [38] to investigate the existence of an isolated resonance curve of the damped system in the neighborhood of one of its nonlinear normal mode interactions. Mass and stiffness proportional damping model [54] was used, defining the damping matrix as  $\mathbf{C} = \alpha \mathbf{M} + \beta \mathbf{K}$  with  $\alpha = -0.0391$  and  $\beta = 1.47 \cdot 10^{-4}$ . These parameters were chosen such that the damping ratios of the first and second linear modes were 1% and 5%, respectively. A lumped mass of 0.5 kg was added  $\alpha = 0.31$  m from the fixed end, and the cubic nonlinear spring had a nonlinear stiffness coefficient of  $\mathbf{K}_{NL} = 6 \cdot 10^9$  N/m<sup>3</sup>.

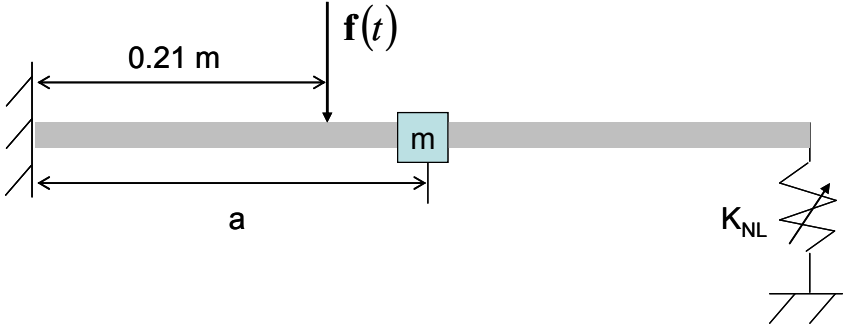


Figure 2. Schematic of a cantilever beam with a cubic nonlinear spring attached to the beam tip and a modifying lumped mass.

Figure 3 shows a frequency-energy plot (FEP) for the system near NNM 1, which was computed using the pseudo-arclength continuation algorithm in [49]. The first NNM (black) increases in frequency as the conserved energy of the response increases, characteristic for hardening type nonlinearities with cubic springs having  $K_{nl}>0$ . Each point along the NNM branch represents a periodic solution to the undamped, nonlinear equations of motion. The damped, forced response was computed using a similar continuation algorithm when a single-point force was applied 0.21 m from the fixed end in the transverse direction, as shown in Fig. 2.

The FEPs of the forced response at four different forcing amplitudes (A = 0.445 N, 0.890 N, 2.22 N and 4.45 N) are also shown in Fig. 3. The NNM was superposed on the plot to show how the forced response wraps around the NNM, acting as the backbone to the damped, forced response.

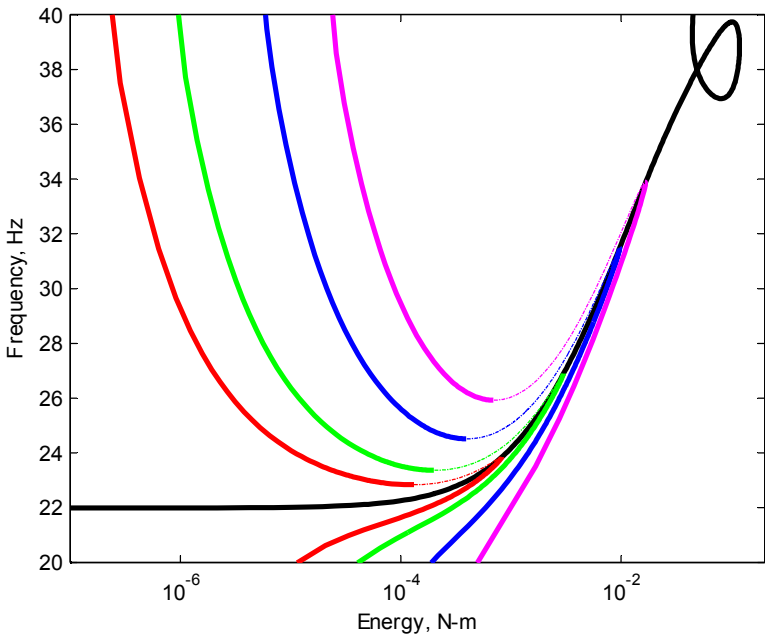


Figure 3. Nonlinear forced response curves at frequencies near the first NNM (black solid) where (colored solid) are stable and (colored dash dot) unstable periodic motions. The force amplitudes for each curve are (red) 0.45 N, (green) 0.89 N, (blue) 2.2 N, and (magenta) 4.5 N.

The backbone of the NNM (black solid) traces the resonant peaks of the forced response (colored) at various forcing amplitudes, even when the curve bends due to the stiffening nonlinearity. The NNM crosses through the turning point (or fold bifurcation) of the forced response, at which point the phase between the force and the displacement is nearly 90 degrees. When resonance occurs for the damped, forced system, the applied force cancels out the damping forces in Eq. (2), so the steady-state response is well approximated by the NNM motion (i.e. the periodic solutions to Eq. (1)). Other works have shown that if the NNM is known, along with the damping matrix, then an energy balancing approach can be used to compute the force amplitude required to excite resonance of the damped system with a single-point harmonic

forcing function [38, 55, 56]. These connections suggest that if a model can accurately predict the NNM backbones of the structure, then the damped forced response near resonance, which is when the structure is at its greatest risk of failure, will also be accurate.

## 1.3 Nonlinear Reduced Order Models

Over the past few decades, a number of non-intrusive strategies have been developed to create a nonlinear reduced order model (NLROM) from a geometrically nonlinear FEA model, as reviewed in [23, 24]. These reduction methods use a Galerkin approach to project the full order equations onto a subset of Ritz vectors, or component modes, to create a set of low order system of (modal) equations of motion. These *indirect* methods assume the FEA model is built directly within a commercial software and the equations of motion are not explicitly known in closed form. Using the linearized component modes as a reduction basis, a low order set of nonlinear modal equations of motion are formulated. For linear elastic finite element models with quadratic strain-displacement relations [1, 4], the nonlinear modal restoring force accounting for geometric nonlinearity is a quadratic and cubic polynomial function of all the modal displacements. These modal equations retain the linear modal mass and stiffness matrices, each of which depend on the component modes used in the transformation. For example, the two-mode model in Eq. (3) shows the form of the ROM reduced with two linear, mass normalized modes  $\varphi_1$  and  $\varphi_2$ . The unknown A and B terms are the nonlinear quadratic and cubic stiffness coefficients, respectively.

$$\begin{bmatrix}
1 & 0 \\
0 & 1
\end{bmatrix} \begin{bmatrix}
\ddot{q}_1 \\
\ddot{q}_2
\end{bmatrix} + \begin{bmatrix}
\omega_1^2 & 0 \\
0 & \omega_2^2
\end{bmatrix} \begin{bmatrix}
q_1 \\
q_2
\end{bmatrix} + \begin{bmatrix}
B_1(1,1)q_1^2 + B_1(1,2)q_1q_2 + B_1(2,2)q_2^2 \\
B_2(1,1)q_1^2 + B_2(1,2)q_1q_2 + B_2(2,2)q_2^2
\end{bmatrix} + \begin{bmatrix}
A_1(1,1,1)q_1^3 + A_1(1,1,2)q_1^2q_2 + A_1(1,2,2)q_1q_2^2 + A_1(2,2,2)q_2^3 \\
A_2(1,1,1)q_1^3 + A_2(1,1,2)q_1^2q_2 + A_2(1,2,2)q_1q_2^2 + A_2(2,2,2)q_2^3
\end{bmatrix} = \begin{bmatrix}
\boldsymbol{\varphi}_1^T \mathbf{f}(t) \\ \boldsymbol{\varphi}_2^T \mathbf{f}(t)
\end{bmatrix}$$
(3)

Direct evaluation methods determine these nonlinear stiffness coefficients by manipulating the full order, nonlinear stiffness matrix in the finite element code [57-59]. These approaches are not considered throughout this work since the nonlinear stiffness matrices within most commercial finite element packages are not readily available. Indirect evaluation methods use a series of nonlinear static solutions to estimate the nonlinear stiffness coefficients. Segalman et al. [60, 61] were one of the first to use such an approach by applying a series of static forces to a nonlinear FEA model to identify the terms in a Taylor series expansion of the nonlinear force-displacement relationship. Two indirect evaluation methods that rely on static analyses to fit the modal models exist in the literature, and those are used within this dissertation.

The first indirect method, referred to as the *enforced displacement* (ED) procedure, was first developed by Muravyov and Rizzi [62]. The geometrically nonlinear FEA model is displaced into the shape of a scaled linear mode shape or a combination of scaled linear mode shapes, and the reaction forces required to hold the displacements are computed by the FEA code. Using a set of displacement fields and reaction forces, the nonlinear stiffness coefficients in the nonlinear modal equations are determined using the procedure outlined in [62]. For thinwalled structures with geometric nonlinearity, the bending-membrane coupling must be accounted for explicitly when selecting a modal basis in order to obtain accurate results. Many works have used axial vibration modes to capture the in-plane kinematics [63-66], but experience has shown that many axial modes are typically needed, and it may be difficult to determine which to include. Mignolet et al. [67] addressed this issue by introducing the *dual* mode, which captures the quasi-static membrane deformation caused by a bending mode, for the in-plane kinematics in the ROM. A similar *companion* mode was developed by Holkamp et al. in [23, 68].

The second indirect approach is the applied loads procedure, which originated with McEwan [69] and is referred to as Implicit Condensation in [19]. As the name suggests, one begins by applying a static force to the nonlinear FEA model which is proportional to the shape, or a combination of shapes, of the linear modes in the basis set, and the resulting displacement fields are computed with the FEA code. A set of statically applied forces and resulting displacements are then used to fit the nonlinear stiffness coefficients in the reduced order model equations using a least squares approach. Since forces are applied to the structure, the bendingmembrane coupling is implicitly captured in the computed response and nonlinear stiffness coefficients, hence requiring that only the bending modes be included in the reduced basis set. If the axial displacements or the corresponding stresses and strains are of interest, then Hollkamp and Gordon's Implicit Condensation and Expansion (ICE) method can be used to recover the membrane motions [70]. Using this approach, an orthogonal set of membrane modes is identified that are quadratic functions of the bending coordinates and they are used to reconstruct the membrane motions that correspond to a given bending displacement. The membrane motions are found in a post processing step and hence their DOF are not included in the nonlinear modal equations of motion.

Each of these parameter estimation methods (ED and ICE) have been shown to produce accurate low order equations of geometrically nonlinear FEA models. They can be used to compute NNMs, transient response or steady-state forced response at a significantly lower cost than compared to the direct integration of the full order model. However, these indirect NLROM strategies have been found to be sensitive to several factors such as the amplitudes of the loads used to fit the nonlinear stiffness coefficients, or the type and number of modes included in the basis [40, 64, 71]. The inaccuracies of the resulting fit may only be visible at certain response

levels due to the amplitude dependence of the NLROM. Relatively few works to date discuss the difficulties that are sometimes encountered when seeking to create an accurate NLROM, and these are exploited with the nonlinear normal modes. Furthermore, this work proposes to create a candidate set of ROMs as modes are added to the basis set, and then compute and track the convergence of the NNMs to determine whether the ROMs are converging or not. These NNMs are relatively inexpensive to compute using the continuation algorithm in [49], so this allows for convergence studies to be performed quickly without the need to run expensive time simulations on the full order model.

Most developments of indirect model reduction have sought to generate a ROM of a structure using its monolithic FEA model of the assembly. While this approach has been very effective for many studies, it becomes exceedingly expensive if the system requires many modal DOF, in turn requiring a prohibitively large number of static load cases to fit the nonlinear stiffness coefficients. For example, to fit the coefficients of a 20-mode model using ICE, one must apply 9,920 permutations of static loads, whereas a 50-mode and a 100-mode model would require 161,800 and 1,313,600, respectively [19]. This cost has been addressed to some extent using the enforced displacement procedure in [72], which uses the tangent stiffness matrix to more efficiently compute the polynomial coefficients reducing the number of static loads on the order of  $N^2$  compared to  $N^3$  with ICE (where N is the number of modes in the basis). They demonstrated the procedure by reducing a 96,000 DOF model of a 9-bay panel down to an 85mode model [72], but even then it was challenging to determine which modes to include and what displacement amplitudes to apply to determine the nonlinear coefficients. The modal substructuring approach proposed in this work divides a large, complicated model into smaller subcomponents, making it presumably easier to create a validated model from these

substructures assuming that each could require fewer mode shapes to capture the kinematics. The subcomponent models can then be assembled to generate a global ROM of the assembly that takes into account the effects of geometric nonlinearity. One advantage to the substructuring approach is that during the design stage the subcomponents are typically redesigned by different teams and independently of the global structure, and so it is more convenient to modify and recompute the models for smaller, simpler subcomponents rather than a larger, global model.

# 1.4 Review of Substructuring Methods

Dynamic substructuring has been used to create reduced order models from large, complicated *linear* finite element models for several decades, as reviewed in [73, 74]. These methods are classified by the domains in which the subcomponent models are defined: either physical, frequency, or modal. The finite element method is an example of substructuring in the physical domain, where simple geometric elements (e.g. beams, plates, etc..) are coupled together to predict the behavior of an assembly of elements [28]. In the literature, modal substructuring, or component mode synthesis (CMS), approaches typically differ by the types of component modes, or Ritz vectors, used to represent the kinematics of the FEA subcomponent models. The first modal substructuring method developed for linear systems was presented by Hurty in [75] using fixed-interface vibration modes, which Craig and Bampton later simplified in [76]; other methods based on free-interface vibration modes were developed later in [77-80].

The Craig-Bampton (CB) substructuring approach [76] reduces each subcomponent model with fixed-interface modes and static constraint modes to account for deformation at the interface. For FEA models with many connecting degrees-of-freedom, the reduced order model may still be prohibitively large since one constraint mode is computed for every interface DOF.

Furthermore, this basis may become ineffective with a high density of closely spaced nodes on the interface [81]. Castanier et al. [82] developed the concept of the characteristic constraint (CC) modes, where a secondary modal analysis is performed on the interface DOF in order to reduce the number of static constraint modes, resulting in a more efficient basis. Others works regarding interface reduction can be found in [83, 84].

A few nonlinear substructuring methods have been developed to predict the dynamics of an assembly based on the dynamics of its subcomponents. In the linear realm, frequency based substructuring is commonly used to predict the frequency response functions of an assembled system. A few works have extended this to nonlinear substructuring using the harmonic balance approach [85-90]. Harmonic balance employs averaging to create a nonlinear system of equations that approximate the frequency and amplitude of the fundamental harmonic (and in some cases higher harmonics [88]) of the steady-state response. These harmonic balance models for each subcomponent are then assembled using an iterative procedure to account for the frequency-amplitude dependence of each part.

A few works have explored the use of nonlinear normal modes computed from each subcomponent as an amplitude dependent basis for substructuring [91-94] but a unified methodology has not yet emerged. In the works to date [91-94], each subcomponent was reduced to a small modal basis (although each work used a different definition) and the subcomponents were assembled to predict the nonlinear dynamics of the overall structure. Other modal substructuring methods exist in which a linear basis is projected onto the subcomponent equations of motion via a Galerkin approach, which are then assembled to give the equations of motion of an assembly. For example, many works [51, 95-99] have subdivided an FEA model into linear subcomponents, reduced them using an appropriate method, then assembled them

with discrete nonlinear elements between the connections (e.g. springs with nonlinear stiffness, or contact elements).

The nonlinear modal substructuring method presented in this dissertation deals with geometric nonlinearities that are distributed throughout all the elements in the subcomponent FEA model. Wenneker and Tiso [100, 101] developed a method for these types of models using component modes defined by the Craig-Bampton [76] and Rubin [78] approach and augmenting these with modal derivative vectors to account for the effects of geometric nonlinearity. The number of modal derivatives required scales quadratically with the number of component modes used, resulting in a rather large order reduced system. Perez [102] was the first to suggest the use of Craig-Bampton modes and a reduced set of constraint modes in conjunction with the enforced displacement reduced order modeling approach reviewed in Section 1.3. He presented a thorough linear analysis of a complicated multi-bay frame reducing the linear model from 96,000 to 232 DOF that were a combination of fixed-interface modes and constraint modes reduced using proper orthogonal decomposition. Unfortunately, this model was still 2.6 times larger than an 89 mode NLROM that he had created for the monolithic system, so the nonlinear modal substructuring was not actually pursued [102].

In this dissertation, a modal substructuring approach for geometrically nonlinear FEA models is proposed by generating subcomponent ROMs using the ICE [19, 103] indirect modeling approach and assembling them by satisfying force equilibrium and compatibility, just as done with linear systems [54, 74]. Three separate subcomponent basis vectors are used to generate the subcomponent modal models, namely free-interface modes [93], fixed-interface plus constraint modes (i.e. Craig-Bampton modes) [104, 105], and fixed-interface plus characteristic constraint modes [106, 107]. The latter basis with characteristic constraint modes was developed

for realistic models with a continuous interface having more than a few DOF, as the number of constraint modes would prohibit the use of the ICE approach and result in a larger ROM of the assembly. The scope of the research in this dissertation is presented next in Section 1.5.

# 1.5 Scope of the Dissertation

Figure 4 shows an overview of the research presented in this dissertation to generate accurate and efficient reduced order models of geometrically nonlinear FEA models. This work considers only an indirect approach, where the structures of interest are modeled in a commercial software.

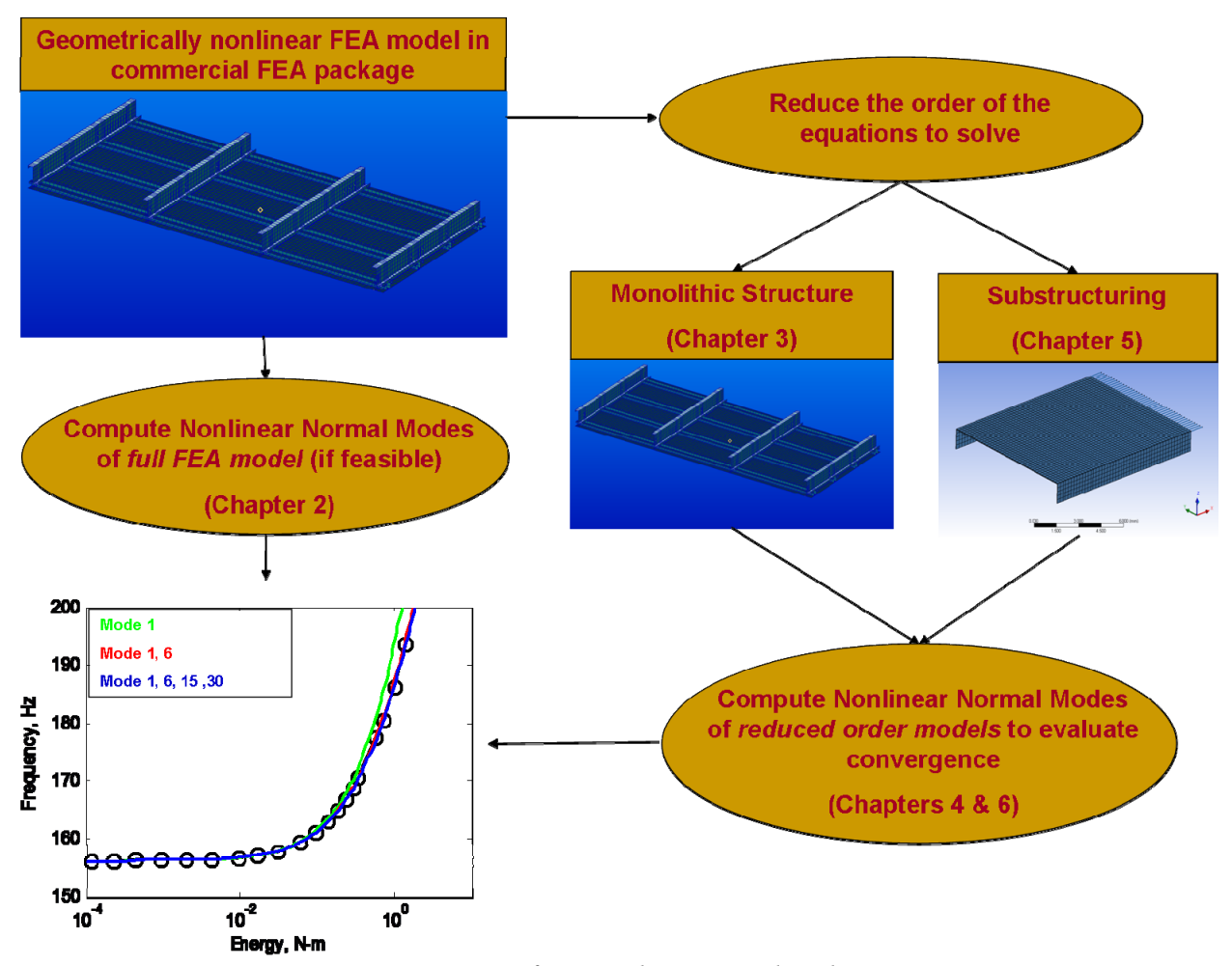


Figure 4. Overview of research presented in dissertation.

Starting with Chapter 2, a pseudo-arclength continuation algorithm is developed that is capable of computing the nonlinear normal modes directly from the full order FEA model. The algorithm is a variant of the one developed by Peeters et al. in [49], which numerically integrates the free response of the nonlinear system to a prescribed set of initial conditions and period of integration in order to evaluate a shooting function that determines whether the response is periodic or not. The algorithm in Chapter 2 wraps around existing FEA packages and nonintrusively calculates the NNMs using the built in time integration and static solvers. The main difference between the method developed by Peeters et al. and the new approach in Chapter 2 is that the initial conditions are determined as a linear combination of a subset of linear vibration mode shapes computed from the linear FEA model, providing a reduction to the continuation variables needed to iterate on during shooting and continuation. This step is essential, otherwise numerical continuation is not feasible for even smaller FEA models with hundreds of DOF. The new continuation algorithm computes NNMs that exactly satisfy the full order equations of motion with no reduction, and is used throughout this work for comparison with the NNMs predicted by the reduced order models.

Chapter 3 reviews the two existing indirect reduced order modeling strategies to extract low order modal models directly from a geometrically nonlinear FEA model. The enforced displacements and applied loads procedures rely on static analyses of a prescribed set of loads to fit the nonlinear portion of the modal equations of motion. There are many modeling decisions that affect the generation of the ROMs such as mode selection, parameter estimation procedures, and amplitude of the static load cases. The geometric nonlinearity causes an amplitude dependent coupling between the bending and membrane type motions, so these effects must be accounted for when selecting an appropriate basis. Furthermore, the scaling levels on the static load cases

dictate the level of geometric nonlinearity excited in the computed responses and ultimately influence the accuracy of the nonlinear stiffness coefficients. These modeling decisions have a very significant effect on the resulting modal equations and the comparison of NNMs from the NLROMs help suggest the best practices that result in the most accurate models.

Chapter 4 presents three case studies where candidate ROMs of nonlinear FEA models are created and the NNMs are computed from these to evaluate convergence/accuracy as more modes are added to the basis, and/or as the scaling of the static load cases change. A detailed study on a geometrically nonlinear beam with clamped-clamped boundary conditions is presented to demonstrate the best practices when creating an NLROM. A larger, more realistic FEA model of an exhaust cover plate with geometric nonlinearity is also presented to demonstrate the approach on a system where the model reduction strategy becomes even more appealing since the model has a large number of DOF (>10,000). For both of these case studies, the true NNMs from the full order model are computed using the algorithm in Chapter 2 for comparison. A third and final case study is presented in Chapter 4 involving a linear beam with simple supports having a contacting nonlinearity at its midpoint. There was no reference NNM for this model due to the excessive number of modal interactions, so the accuracy of the ROM is evaluated based on the convergence of the NNM backbones and internal resonances. In order to confirm that the ROM is indeed most accurate when the NNMs converge, the response from an impulse load and random input is compared to the response predicted by the full order model.

Chapter 5 presents an extension to the indirect reduced order modeling strategies by developing of a novel modal substructuring approach that first divides the full order FEA model of interest into smaller subcomponent models. These geometrically nonlinear subcomponent models are reduced using the Implicit Condensation and Expansion procedure, as reviewed in

Chapter 3. Chapter 5 presents the theory used to generate the subcomponent models using either its free-interface modes, fixed-interface plus constraint modes, or fixed-interface plus characteristic constraint modes. Once the ROMs are generated, they are coupled at the interface by enforcing compatibility and force equilibrium, ultimately producing a set of nonlinear differential equations of the global assembly. These reduced order models are used to compute nonlinear normal modes for validation of the assembled equations. Upon validation, these modal models can be used for accurate time integration to external forces with far less CPU cost compared to the direct integration of the subcomponent models assembled in the physical domain (i.e. the full order FEA model of the global assembly).

Chapter 6 presents three case studies using the nonlinear modal substructuring approach to couple subcomponent FEA models with geometric nonlinearity. The NNMs are computed as an increasing number of modes are included in each subcomponent basis, and reference NNMs are computed from the full order model of the total assembly. The first case study couples two geometrically nonlinear beams at a shared rotational DOF. The NLROMs are generated with free-interface modes, and fixed-interface plus constraint modes, and are used to evaluate the nonlinear modal convergence with its NNMs. A second example demonstrates this approach on a nonlinear beam with an axial spring element added to an axial DOF. This example is motivated by the need to accurately model of in-plane forces as they become especially important during the analysis of coupled fluid-thermal-structural interactions [22] (the in-plane resistance to thermal expansions strongly affects the onset of buckling). The final case study demonstrates the use of fixed-interface modes and characteristic constraint modes on the assembly of two nonlinear plates.

Chapter 7 makes concluding remarks regarding the work presented here and Chapter 8 presents a three ideas for future work that could help strengthen the research presented throughout this dissertation.

# 2 Indirect Computation of Nonlinear Normal Modes

## 2.1 Introduction

A variant on the pseudo-arclength continuation algorithm by Peeters et al. [49] is developed in this chapter to compute the nonlinear normal modes of a geometrically nonlinear finite element model within its native code, meaning that any commercial package can be used to model the system. The structural model is numerically integrated, using the available integration schemes within the FEA package, to a prescribed initial condition and period of integration in order to check whether a periodic response is obtained. Shooting is used to minimize an objective function called the shooting function, which is defined as the difference between the states at two discrete times, giving a mathematical condition of periodicity. The Jacobian of the shooting function is used within a Newton-Raphson scheme to find each periodic solution of the conservative equations of motion, otherwise known as the nonlinear normal mode.

Since the finite element model exists within the native code, the equations of motions are not available in closed form. For this reason, the method used in the code developed by Peeters et al. for efficiently computing the Jacobian [50] cannot be used since it requires the first derivative of the nonlinear equations of motion. Therefore, the first derivative must be computed using finite differences (e.g. by perturbing each DOF). This tends to excite high frequency modes so that a very small time step must be used to accurately integrate the free response. Also, using each state in a large DOF model as a continuation variable would require far too many finite difference computations to generate a Jacobian matrix. These two issues will result in excessive computational cost for computing NNMs of finite element models of even modest size. To circumvent this cost, this chapter proposes an alternative NNM algorithm where the initial

conditions are defined from a subset of modal coordinates based on the linear modes of the underlying linear equations of motion. This significantly reduces the number of variables that must be iterated on by the shooting and continuation algorithm.

In order to uniquely define a nonlinear normal mode branch (or set of periodic solutions), the initial states (displacement and velocity) and period of integration must be determined. In this work, a more practical strategy for finding periodic solutions is used, in which all of the initial velocities are set to zero, eliminating half of the unknown variables for each prediction and correction step, as was done in [49]. Two methods are proposed here to define the initial displacements, which are based on a subset of the linear modal coordinates. The first method, termed enforced modal displacements (EMD), defines the initial conditions by enforcing the displacement of the structure into a deformation that is a linear combination of linear mode shapes. The second approach, termed applied modal force (AMF), sets the initial conditions based on the static equilibrium that results from a linear combination of applied forces that excite only a single linear mode. Regardless of the method to define the initial conditions, the continuation of each NNM branch initiates at a single linear mode solution at low energy, so the continuation algorithm requires only one modal coordinate at first. This greatly reduces the cost of the Jacobian since a single finite difference calculation is needed for the first prediction step. As the algorithm follows the NNM branch to higher response amplitudes, or energies, the participation of other modes is monitored in the time response, and modes are added once they begin to contribute significantly to the shooting function. This reduction of variables that define the shooting function greatly reduces the computational burden, making this approach feasible for finite element models of moderate size (10,000's of DOF).

# 2.2 Nonlinear Normal Modes of Large Order Systems

Consider an autonomous, conservative nonlinear system of equations, discretized by the finite element method. The equations of motion with *N* degrees-of-freedom can be written as

$$\mathbf{M}\ddot{\mathbf{x}} + \mathbf{K}\mathbf{x} + \mathbf{f}_{NL}(\mathbf{x}) = \mathbf{0} \tag{4}$$

where **M** and **K** are the respective  $N \times N$  linear mass and stiffness matrices, and  $\mathbf{f}_{NL}(\mathbf{x})$  is the  $N \times 1$  nonlinear restoring force vector. The nonlinear equations can be recast into the state space form

$$\dot{\mathbf{z}} = \begin{cases} \dot{\mathbf{x}} \\ \ddot{\mathbf{x}} \end{cases} = \begin{cases} \dot{\mathbf{x}} \\ -\mathbf{M}^{-1} \{ \mathbf{K} \mathbf{x} + \mathbf{f}_{NL}(\mathbf{x}) \} \end{cases}$$
 (5)

where  $\mathbf{z}$  is the  $2N \times 1$  time dependent state vector, such that  $\mathbf{z} = \begin{bmatrix} \mathbf{x}^T & \dot{\mathbf{x}}^T \end{bmatrix}^T$  is comprised of N physical displacements in  $\mathbf{x}$  and N velocities in  $\dot{\mathbf{x}}$ , and  $\begin{pmatrix} 1 \end{pmatrix}^T$  represents the transpose operation. The approach developed by Peeters et al. in [49], which is based on the shooting technique and pseudo-arclength continuation, computes the undamped NNMs of the conservative system in Eq. (5). An NNM, which is a periodic orbit, is uniquely defined by the period T and initial conditions  $\mathbf{z}_0$  which produce a periodic response such that  $\mathbf{z}_p(T,\mathbf{z}_0) = \mathbf{z}_p(0,\mathbf{z}_0)$ , although there is no loss of generality if the system is time invariant. The shooting technique determines the initial condition vector  $\mathbf{z}_0$  and period T that satisfy the periodicity condition, and iterates on the  $2N \times 1$  unknown variables.

The algorithm presented in this chapter determines the initial conditions of a nonlinear system with *N*-DOF using a modal coordinate transformation based on the underlying linear normal modes in order to reduce the number of variables required for continuation. The linear

modes are computed from the undamped, linear(ized) equation of motion, e.g. by solving  $(\mathbf{K} - \omega_r^2 \mathbf{M})_{\mathbf{p}_r}$  if the equilibrium of interest is at  $\mathbf{z} = \mathbf{0}$ . A coordinate transformation is then used to represent the physical displacements in terms of the linear modal coordinates as

$$\mathbf{x} = \mathbf{\Phi}\mathbf{q} \tag{6}$$

where  $\Phi$  is the  $N \times N$  linear mode shape matrix, and each column represents a mass normalized mode shape vector. (For large scale finite element models where it is impractical to extract all the modes, only a subset of modes will be contained in this matrix.) Since the nonlinear normal modes initiate at a single, linear mode at low amplitude, the initial solution required for the continuation algorithm in that regime is simply  $q_n \neq 0$  for the mode of interest, which is a dramatic reduction compared to all the displacements and velocities in  $\mathbf{z}_0$ . Two methods are proposed to define the initial conditions based on the modal coordinate transformation, namely the enforced modal displacement and applied modal force methods.

## 2.2.1 Enforced Modal Displacements (EMD)

The enforced modal displacements method uses only the modal displacement amplitudes as the free parameters in the continuation algorithm. All initial velocities are set to zero in order to reduce the number of continuation variables by a factor of two, and fix the phase of each periodic motion. The initial state with the EMD method is defined as

$$\mathbf{z}_0 = \begin{bmatrix} \mathbf{\Phi} & \mathbf{0} \\ \mathbf{0} & \mathbf{\Phi} \end{bmatrix} \begin{Bmatrix} \mathbf{q}_0 \\ \mathbf{0} \end{Bmatrix} \tag{7}$$

where the modal amplitudes  $\mathbf{q}_0$  are all zero, except for the modes included in the continuation variables. A periodic solution for a conservative, nonlinear system depends on the initial modal displacements  $\mathbf{q}_0$  and period of oscillation T, and must satisfy the periodicity condition

$$\mathbf{z}_{p}(T,\mathbf{q}_{0}) = \mathbf{z}_{p}(0,\mathbf{q}_{0}) \tag{8}$$

An NNM initiates at a linear mode at low energy, so when computing the branch corresponding to the  $r^{th}$  NNM, the initial modal displacement vector is

$$\mathbf{q}_0 = \mathbf{q}_{0,r} = \begin{cases} q_n & n = r \\ 0 & n \neq r \end{cases} \tag{9}$$

such that the modal amplitude of the  $r^{\text{th}}$  mode,  $q_{n=r}$ , is small enough to assure that the nonlinear system's response is well in its linear range. The integration period T for the initial solution is determined from the linear natural frequency. Note that no iteration is required within continuation for the linear modal coordinates that are set to zero. As the NNM is continued to higher energy, additional linear modes may become active in the nonlinear response. Hence, the modal amplitudes of all the modes of the system are monitored in the computed free response as the shooting algorithm drives the system towards convergence. Additional modes are added to the coordinate set when their response is needed to satisfy shooting function. For example, if the  $i^{\text{th}}$  mode needs to be added to the basis set, a new vector is defined as

$$\mathbf{q}_{0,i} = \begin{cases} q_n & n = i \\ 0 & n \neq i \end{cases} \tag{10}$$

which contains only a coordinate value for the  $i^{th}$  mode. The modal coordinates for continuation then become

$$\mathbf{q}_0 = \mathbf{q}_0 + \mathbf{q}_{0,i} \tag{11}$$

Hence, the number of linear modes, denoted m, in the truncated modal coordinate set may increase with increasing energy.

#### 2.2.2 Applied Modal Force Method (AMF)

While the previous approach is conceptually simple, it has sometimes been found to require far more modes than one would hope to obtain a converged NNM. It was discovered that many of the modes that were included had only a static effect on the response (e.g. membrane displacements caused by bending motions for models with geometric nonlinearity), and hence the following approach is developed to implicitly include those effects in the initial conditions. First, a static force is applied to the nonlinear FEA model, such that the force is a linear combination of the forces that would each excite a single linear mode. The static response to this force is computed and used to define the initial conditions within continuation. Specifically, the static load is defined as

$$\mathbf{F}_{static} = \mathbf{M}\mathbf{\Phi} \ \mathbf{q}_0 \tag{12}$$

In the AMF approach, the vector  $\mathbf{q}_0$  now represents modal force amplitudes instead of initial modal displacement amplitudes. Premultiplying the force by the mass matrix guarantees that a single mode force (e.g. one entry in  $\mathbf{q}_0$ ) would exactly excite the corresponding linear mode in the linear system. The deformation in response to the force in Eq. (12) is found using the built in nonlinear static solver such that the following nonlinear equation is satisfied

$$\mathbf{K}\mathbf{x}_{0,static} + \mathbf{f}_{NL}(\mathbf{x}_{0,static}) = \mathbf{M}\mathbf{\Phi} \mathbf{q}_{0}$$
(13)

The initial conditions based on this static equilibrium become,

$$\mathbf{z}_{0} = \begin{cases} \mathbf{x}_{0,static} \\ \mathbf{0} \end{cases} \tag{14}$$

again assuming the initial velocities are set to zero. If  $\mathbf{x}_{0,static}$  were projected onto the linear modes of the system, every modal amplitude may be nonzero. Similar to the EMD approach, the  $r^{th}$  NNM is initiated with only the  $r^{th}$  modal coordinate in  $\mathbf{q}_0$  set to a small value, as done with Eq. (9). At low energy, the static deformation in Eq. (13) to an initial force profile defined by Eq. (12) will result in a displacement field exactly in the  $r^{th}$  linear mode shape. As the NNM branch increases in energy, additional modes are added to the coordinate set as they are needed for convergence of the shooting function, as explained later in Section 2.3.4.

# 2.3 Shooting and Pseudo-Arclength Continuation Algorithm

The pseudo-arclength continuation algorithm used here is essentially the same as that in [49], but instead uses the EMD or AMF methods to reduce the number of variables to define the initial displacements. These initial conditions greatly reduce the number of finite difference computations required to estimate the Jacobian matrix used in the prediction and correction steps. The mode augmenting scheme described in 2.3.4 is also novel to the pseudo-arclength continuation algorithm presented in this chapter. The flow chart in Fig. 5 highlights the general steps of the algorithm, and the details of the algorithm are presented in the following subsections.

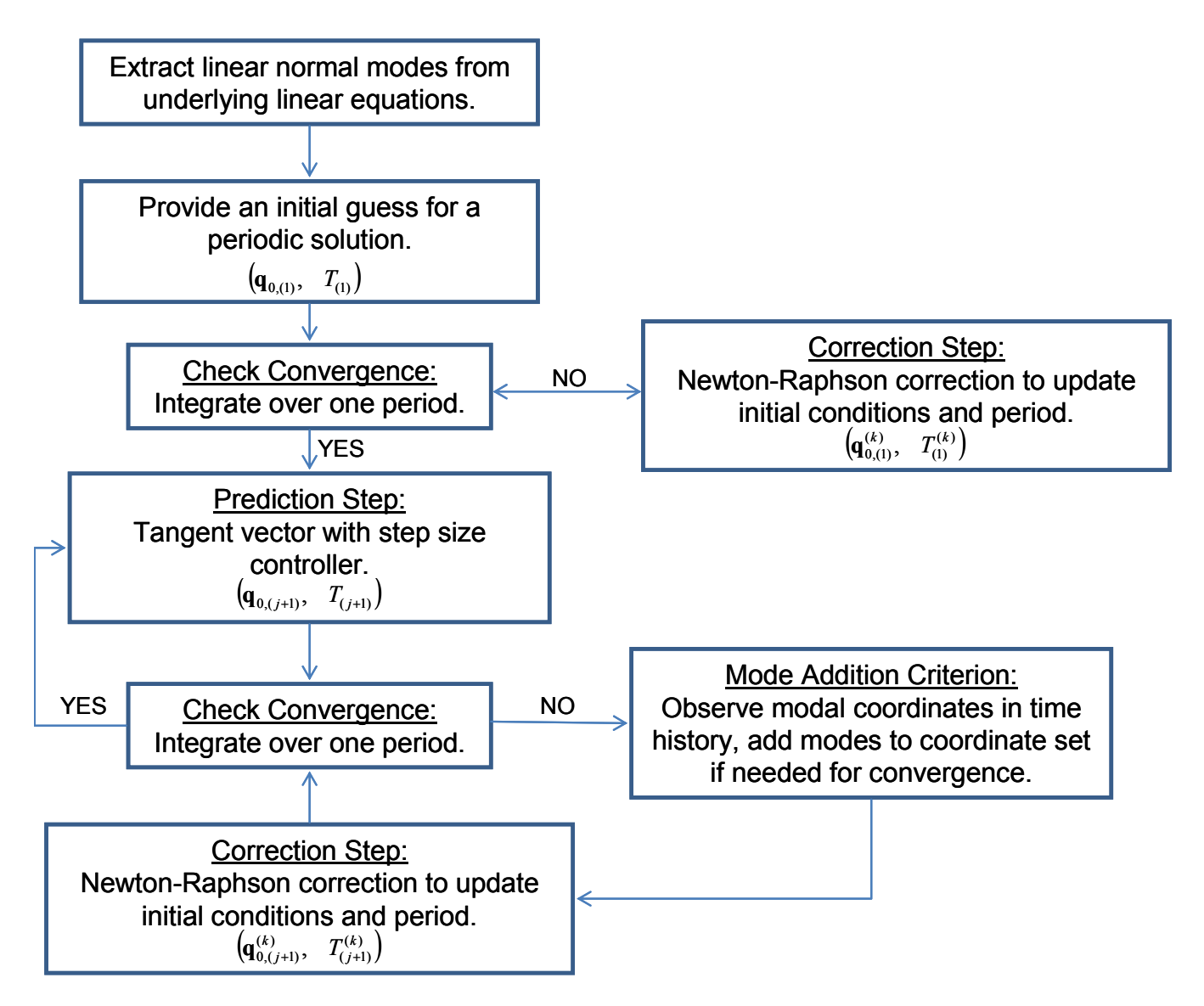


Figure 5. Schematic of the AMF and EMD continuation algorithms to compute nonlinear normal modes.

## 2.3.1 Shooting Technique

The Newton-Raphson algorithm searches for solutions that satisfy the shooting function, solving the two-point boundary value problem [45] of Eq. (5), and is defined as

$$\mathbf{H}(T, \mathbf{q}_0) = \mathbf{z}_T(T, \mathbf{q}_0) - \mathbf{z}_0(0, \mathbf{q}_0) = \mathbf{0}$$
(15)

The  $2N \times 1$  shooting function,  $\mathbf{H}(T, \mathbf{q}_0)$ , is converged with tolerance,  $\varepsilon$ , if the following condition is satisfied.

$$\frac{\left\|\mathbf{H}(T,\mathbf{q}_0)\right\|}{\left\|\mathbf{z}_0(0,\mathbf{q}_0)\right\|} < \varepsilon \tag{16}$$

A Taylor series expansion of Eq. (15) is used to make corrections to the continuation variables  $\mathbf{q}_0$  and T in the event that Eq. (16) is not satisfied, just as done in [49]. The corrections to the initial modal amplitudes and period ( $\Delta \mathbf{q}_0$ ,  $\Delta T$ ) of the system generally satisfy the algebraic equation,

$$\left[ \frac{\partial \mathbf{H}}{\partial \mathbf{q}_0} \Big|_{\mathbf{q}_0, T} \quad \frac{\partial \mathbf{H}}{\partial T} \Big|_{\mathbf{q}_0, T} \right] \left\{ \Delta \mathbf{q}_0 \right\} = -\mathbf{H}(T, \mathbf{q}_0) \tag{17}$$

where the Jacobian is the  $2N \times (m+1)$  matrix on the left hand side of the equation. For the AMF and EMD algorithms, the number of modal amplitudes is drastically smaller than the number of physical DOF (i.e. N >> m). The Jacobian is generated using a forward finite difference scheme, requiring a total of m numerical integrations over a period T. The Jacobian is then transformed into modal coordinates, reducing the size of the matrix in Eq. (17) from  $2N \times (m+1)$  to  $2m \times (m+1)$ . This is accomplished by premultiplying both sides of Eq. (17) by the  $2m \times 2N$  transformation matrix,

$$\mathbf{B} = \begin{bmatrix} \mathbf{\Phi}_{m}^{\mathrm{T}} \mathbf{M} & \mathbf{0} \\ \mathbf{0} & \mathbf{\Phi}_{m}^{\mathrm{T}} \mathbf{M} \end{bmatrix}$$
 (18)

where  $\Phi_m^T$  contains the mass normalized mode shapes of the active modes as its rows. If the mass matrix **M** is not available, a Moore-Penrose pseudo inverse can be used to invert the non-

square mode matrix. Premultiplying Eq. (17) by the transformation matrix  $\mathbf{B}$  in Eq. (18) eliminates any portion of the shooting function that is orthogonal to the m modes in the active coordinate set, producing the following algebraic relation,

$$\left[ \frac{\partial \mathbf{H}_{q}}{\partial \mathbf{q}_{0}} \Big|_{\mathbf{q}_{0},T} \quad \frac{\partial \mathbf{H}_{q}}{\partial T} \Big|_{\mathbf{q}_{0},T} \right] \left\{ \Delta \mathbf{q}_{0} \right\} = -\mathbf{H}_{q}(T,\mathbf{q}_{0}) \tag{19}$$

 $\mathbf{H}_q$  represents the shooting function in terms of the *m* modal coordinates active in  $\mathbf{q}_0$ . The new initial states and periods are updated using  $(\Delta \mathbf{q}_0, \Delta T)$ , providing the corrected initial modal amplitudes and period as

$$\mathbf{q}_0^{(k+1)} = \mathbf{q}_0^{(k)} + \Delta \mathbf{q}_0^{(k)}$$
(20)

$$T^{(k+1)} = T^{(k)} + \Delta T^{(k)}$$
(21)

The Jacobian matrix used in Eq. (19) is used throughout the prediction and correction steps that follow.

## 2.3.2 Pseudo-Arclength Continuation: Prediction Step

The prediction step uses the last computed solution  $(\mathbf{q}_{0,(j)}, T_{(j)})$  to estimate a prediction vector  $\begin{bmatrix} \mathbf{P}_{q,(j)}^{\mathrm{T}} & P_{T,(j)}^{\mathrm{T}} \end{bmatrix}^{\mathrm{T}}$  tangent to the NNM branch, and is computed by solving the linear system of equations defined as

$$\begin{bmatrix}
\frac{\partial \mathbf{H}_{q}}{\partial \mathbf{q}_{0}}\Big|_{\mathbf{q}_{0,(j)},T_{(j)}} & \frac{\partial \mathbf{H}_{q}}{\partial T}\Big|_{\mathbf{q}_{0,(j)},T_{(j)}}
\end{bmatrix} \begin{Bmatrix} \mathbf{P}_{q,(j)} \\ P_{T,(j)} \end{Bmatrix} = \begin{Bmatrix} \mathbf{0} \\ 0 \end{Bmatrix}$$
(22)

where the Jacobian is the same as the one in Eq. (19). This requires m additional integrations of the equations of motion over the period T about the last solution ( $\mathbf{q}_{0,(j)}$ ,  $T_{(j)}$ ). The normalized prediction vector then uses the same step size control algorithm described by Peeters et al. to obtain a prediction of the next solution as

$$\mathbf{q}_{0,(j+1)} = \mathbf{q}_{0,(j)} + s_{(j)} \cdot \mathbf{P}_{q,(j)}$$
(23)

$$T_{(j+1)} = T_{(j)} + s_{(j)} \cdot P_{T,(j)}$$
(24)

The step size controller,  $s_{(j)}$ , is determined by user defined inputs, such as the minimum and maximum step size, as well as the ideal and maximum number of correction iterations as described in [49].

#### 2.3.3 Pseudo-Arclength Continuation: Correction Step

The predicted solution  $\mathbf{q}_{0,(j+1)}$  is evaluated for periodicity over the period  $T_{(j+1)}$  using the shooting function in Eq. (15). If the periodicity condition is satisfied, then the solution is stored and a new prediction is made from this new solution. If the shooting function is not satisfied, then a corrector step is initiated using the Newton-Raphson approach to compute an update to the modal amplitudes,  $\Delta \mathbf{q}_{0,(j+1)}^{(k)}$ , and period  $\Delta T_{(j+1)}^{(k)}$ , where k denotes the k<sup>th</sup> correction iteration. The updates are computed using the Jacobian matrix in Eq. (19), with the added constraint that the correction must be perpendicular to the prediction vector. This is accomplished by solving the linear system of equations

$$\begin{bmatrix}
\frac{\partial \mathbf{H}_{q}}{\partial \mathbf{q}_{0}}\Big|_{\mathbf{q}_{0,(j+1)}^{(k)}, T_{(j+1)}^{(k)}} & \frac{\partial \mathbf{H}_{q}}{\partial T}\Big|_{\mathbf{q}_{0,(j+1)}^{(k)}, T_{(j+1)}^{(k)}} \\
\{\mathbf{P}_{q,(j)}\}^{\mathrm{T}} & P_{T,(j)}
\end{bmatrix} = \begin{bmatrix}
\Delta \mathbf{q}_{0,(j+1)}^{(k)} \\
\Delta T_{(j+1)}^{(k)}
\end{bmatrix} = \begin{bmatrix}
-\mathbf{H}(T_{(j+1)}^{(k)}, \mathbf{q}_{0,(j+1)}^{(k)}) \\
0
\end{bmatrix}$$
(25)

The updated period and initial conditions are then computed using Eqs. (20) and (21). The shooting function in Eq. (15) is evaluated for each correction step until convergence is met, at which point the solution  $\mathbf{q}_{0,(j+1)}$  and  $T_{(j+1)}$  is stored and used to predict the next solution.

Because the nonlinearity essentially couples the underlying linear modes, additional modes may begin to contribute to the response as the energy (or response amplitude) increases. These modes, if not accounted for, may prevent the convergence of the shooting function within the correction step of the algorithm. Therefore, an additional procedure is needed to detect modes that may be important to obtain a periodic response, and add them when appropriate. Since the size of the Jacobian in Eqs. (22) and (25) is governed by the number of active modal coordinates m, it is preferable to include the smallest number of modes possible.

#### 2.3.4 Add Linear Modal Coordinate

Within the correction step of the algorithm, the modes not included in  $\mathbf{q}_0$  are monitored with respect to their contribution to the shooting function in Eq. (15). The shooting function is premultiplied by the transformation matrix  $\mathbf{B}$  in Eq. (18) to filter modes only within the active coordinate set, and then transformed back to physical coordinates, as follows

$$\hat{\mathbf{H}} = \begin{bmatrix} \mathbf{\Phi}_m & \mathbf{0} \\ \mathbf{0} & \mathbf{\Phi}_m \end{bmatrix} \mathbf{B} \mathbf{H} (T_{(j+1)}^{(k)}, \mathbf{q}_{0,(j+1)}^{(k)})$$
(26)

The new shooting function,  $\hat{\mathbf{H}} \in \mathbb{R}^{2N}$ , is used to determine whether the neglected modes prevent convergence by evaluating the condition

$$\frac{\left\|\hat{\mathbf{H}}(T_{(j+1)}^{(k)}, \mathbf{q}_{0,(j+1)}^{(k)})\right\|}{\left\|\mathbf{z}_{0}(0, \mathbf{q}_{0,(j+1)}^{(k)})\right\|} < \varepsilon \tag{27}$$

If Eq. (27) has converged to the desired numerical tolerance  $\varepsilon$ , but the full shooting function in Eq. (15) has not, then a new mode is augmented to the modal variables as described in Eqs. (10) and (11). To determine which mode to add, the shooting function is transformed into modal displacements as

$$\mathbf{H}_{q} = \begin{bmatrix} \mathbf{I} & \mathbf{0} \end{bmatrix} \mathbf{B} \mathbf{H} (T_{(j+1)}^{(k)}, \mathbf{q}_{0,(j+1)}^{(k)})$$
(28)

The maximum value of each modal coordinate in the shooting function is found and the most dominant mode not currently in the variable set is added to the continuation variables. The correction procedure is then resumed with *m* augmented by one. While this augmenting scheme will allow the algorithm to converge to a periodic solution, experience has shown that modes may be unnecessarily added. This tends to occur when the prediction step is somewhat far from the NNM branch, or when finding an internal resonance that emanates from the backbone. Even when this happens, the number of free variables is still greatly reduced relative to the original algorithm, so this is not a large concern. One could add a condition to discard modes that are not required for convergence, but this has not been pursued in this work.

#### 2.3.5 FEA-Interface with NNM Algorithm

The AMF and EMD algorithms have been implemented in MATLAB®, and can interface with many existing nonlinear finite element packages, which serve as a "black box" integrator for the nonlinear system of interest. A schematic of the interface between the continuation algorithm and the finite element software package is shown in Fig. 6. In this dissertation, only geometric nonlinearities are considered, but other nonlinearities, such as contact and material nonlinearity, could be accommodated as long as the equations of motion are conservative. The initial conditions,  $\mathbf{z}_0$ , are input to the finite element model from the continuation algorithm and

integrated by finite element code over a desired period T. The time histories of the response are exported back into MATLAB for further evaluation (e.g. determining whether  $\mathbf{q}_0$  and T satisfy the shooting function). The time history data is written to a text file from the finite element package, which is then read into MATLAB for evaluation. A more intrusive approach could be used without reading/writing text files, and would likely improve the efficiency of the NNM algorithm. This was not implemented for the results throughout this work, so the computational times presented reflect a conservative number.

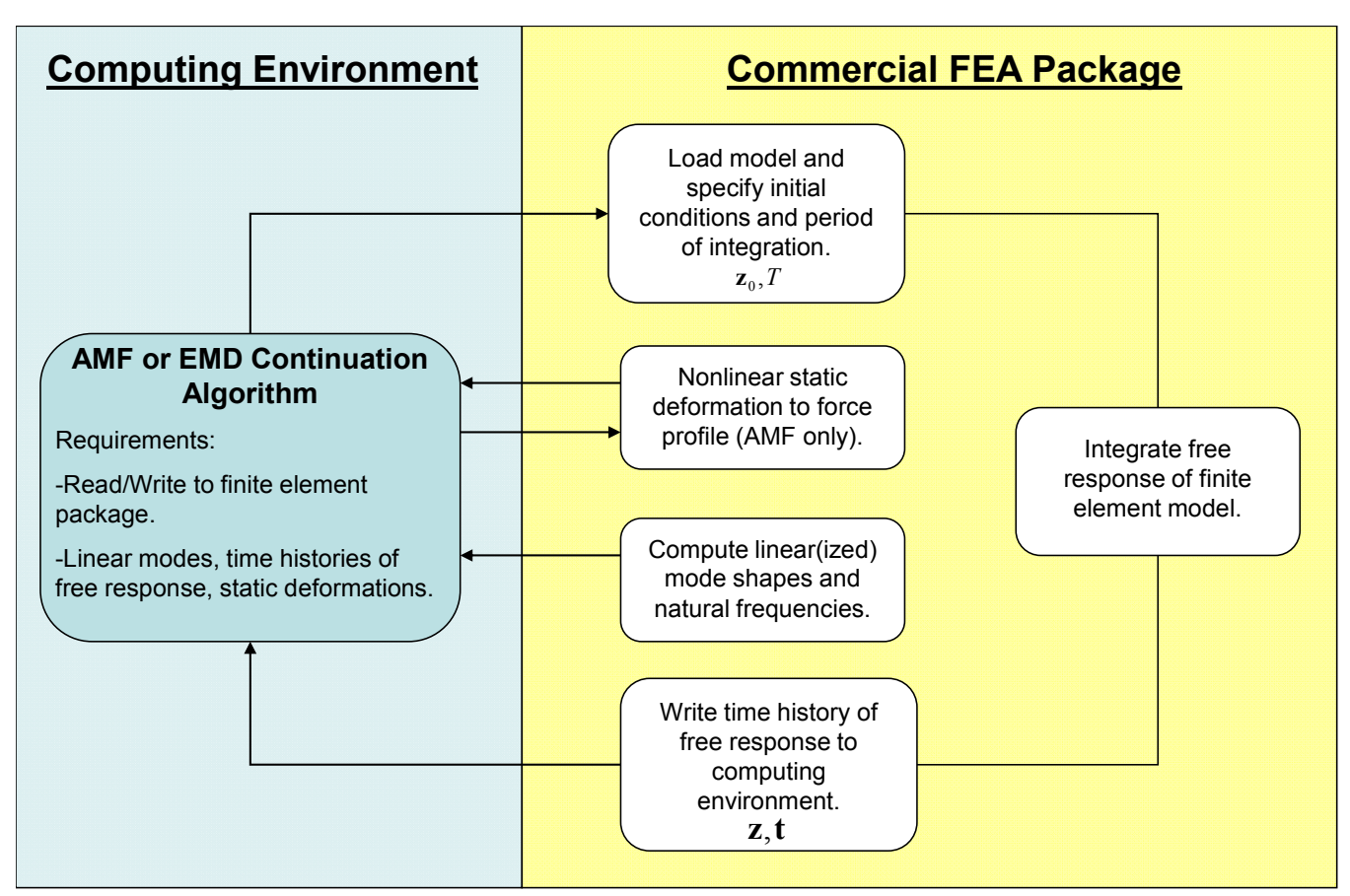


Figure 6. Schematic of interface between computing environment and commercial finite element package.

The nonlinear normal modes of two geometrically nonlinear finite element models were computed using the proposed EMD and AMF strategies. The nonlinear modes are presented on a two dimensional frequency-energy plane, where each point along the curve represents a free

periodic response exactly satisfying the full order finite element model. The fundamental frequency of the response is plotted along the vertical axis, while the total conserved energy (kinetic plus potential) of the response is on the horizontal axis. The results from a geometrically nonlinear clamped-clamped beam are presented first, followed by a more realistic model of an exhaust cover plate.

## 2.4 Application to Clamped-Clamped Beam with Geometric Nonlinearity

The EMD and AMF algorithms were applied to a finite element model in Abagus® of a clamped-clamped beam with geometric nonlinearity. The model was constructed using forty B31 beam elements, resulting in a total of 117 DOF. The B31 element is a 2-noded 3-D Euler-Bernoulli beam that uses linear interpolation between each node. The out of plane z displacement, and x and y rotations were fixed to model the beam as planar. The beam was 9 inches (229 mm) long, 0.5 inches (12.7 mm) wide and 0.031 inches (0.787 mm) thick. It was constructed of structural steel with a Young's modulus of 29,700 ksi (204.8 GPa), shear modulus of 11,600 ksi (80.0 GPa) and mass density of 7.36·10<sup>-4</sup> lb-s<sup>2</sup>/in<sup>4</sup> (7,870 kg/m<sup>3</sup>). The model geometry was adopted from [19, 23, 108], where the beam served as a benchmark to validate a variety of nonlinear model reduction strategies. The full, mass normalized mode matrix was extracted using Abagus' Lanczos eigensolver. Abagus directly integrated the free response to a prescribed initial condition determined by  $\mathbf{q}_0$  using its implicit Newmark-Beta scheme. The average acceleration method was used with integration parameters  $\gamma=0.5$  and  $\beta=0.25$  [28], such that algorithmic damping was not introduced into the time response. A suitable time step was required to accurately capture the higher order harmonics of the response introduced by the geometric nonlinearity. For the results shown this was accomplished by using 500 equidistant time steps over one period of integration.

The first nonlinear normal mode of the beam was computed using the EMD and AMF approaches with a shooting tolerance set to  $\varepsilon = 10^{-4}$ , and is shown in Fig. 7. Since the backbones were of primary interest, a large maximum step size was used in the continuation algorithm in hopes of "skipping" over any internal resonances that emanate from the backbone (a more detailed NNM is presented later in Fig. 8). These results were used to evaluate the mode augmenting scheme. At low energy, each branch was initiated with only the first linear bending modal coordinate in the variable set. As the amplitude of the periodic response increased, more modes were added to the modal set in order to satisfy the shooting function to the given tolerance (these are marked with a star or triangle for the AMF and EMD methods, respectively).

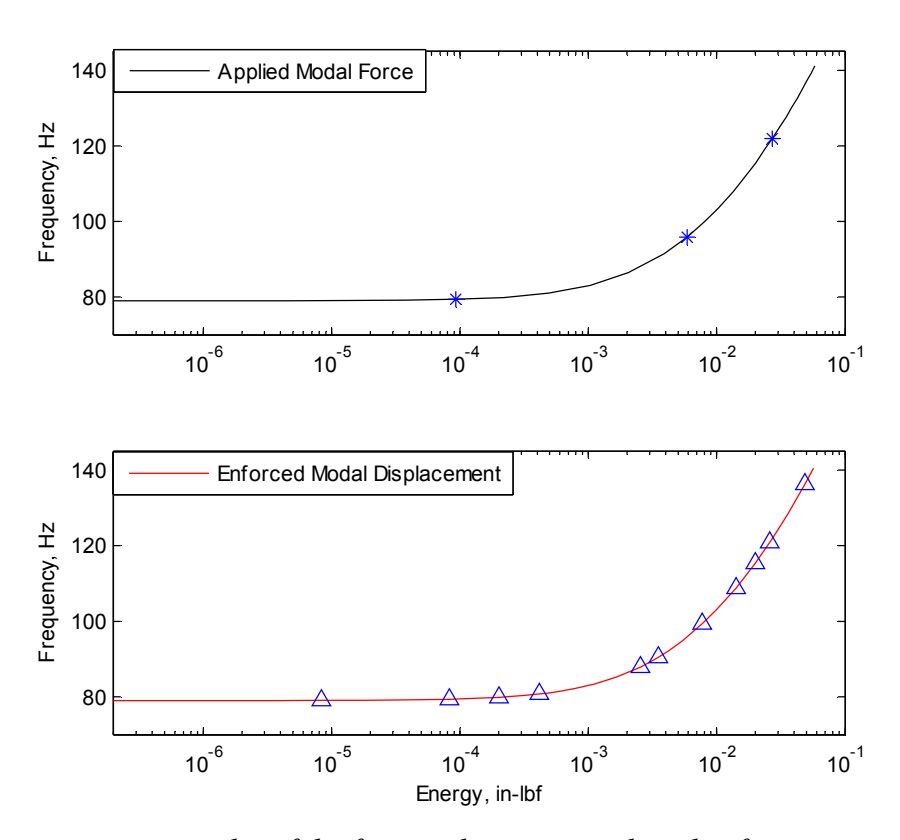


Figure 7. Frequency-energy plot of the first nonlinear normal mode of a geometrically nonlinear beam. (Star) and (triangle) represents an added mode for the AMF and EMD method, respectively. (Note that 1 in-lbf = 0.113 N-m.)

The frequency-energy plots (FEPs) produced by the EMD and AMF methods were indistinguishable, which was evident when the two branches were overlaid on the same plot (not shown here for brevity). This is expected since the only difference was the method used to determine the initial conditions; the solutions found by both algorithms satisfy the same shooting function to the same tolerance when integrated with the same finite element model. There was a significant difference in computational cost between the two approaches, however. For the branches in Fig. 7, the AMF algorithm took a little over two hours to compute, while the EMD approach took about 8 hours on a desktop computer with 8 GB of RAM and an Intel® Core i7 CPU. Tables 1 and 2 show the resulting modes that were added to the modal coordinate set as the energy in the NNM 1 branch increased. For a frequency shift of ~77%, the AMF only required a total of 4 modes, while the EMD method needed 18 modes. For either algorithm this represents a significant reduction in the number of variables required to define the initial conditions for the continuation algorithm, compared to the 117 DOF that define each physical displacement and rotation of the model. The significance of this reduction comes through the cost required to compute the Jacobian matrix, which requires a finite difference calculation (one period of integration of the full finite element model) for each variable at every prediction/correction step.

*Table 1. Modes added to NNM 1 using Applied Modal Force.* 

Frequency, Hz	79.4	95.9	121.9
Mode Added	3	5	7

*Table 2. Modes added to NNM 1 using Enforced Modal Displacement.* 

Frequency, Hz	79.1	79.4	79.9	80.8	87.9
Mode Added	3	5, 39	7, 26	9, 45	11
Frequency, Hz	99.3	108.8	115.4	120.9	136.3
					24, 27, 51,
Mode Added	17, 47	20	49	22	53

It is important to note that AMF adds extra computational cost compared to EMD since a nonlinear static solution is required each time the model is integrated. For the beam studied here, each static solution took about 10 seconds, while the numerical time integration over one period took approximately 30 seconds. This 10 second increase from the nonlinear static solution was far outweighed by the fact that AMF only had to iterate on 4 modes compared to 18 for the EMD algorithm. For models with geometric nonlinearity, the quasi-static bending-axial coupling for flat structures caused a stiffening effect as bending motions increased in amplitude. This was implicitly captured by the preliminary static equilibrium solution of the AMF method. For example, when a force was applied to the structure in the shape of only the first bending mode using Eq. (12), other modes would be "statically" coupled to the response. When projecting this static response onto the linear modes, the first mode would dominate the displacement, but other modes would be implicitly present as well. The 26<sup>th</sup> and 39<sup>th</sup> axial vibration modes (along with other bending modes) showed up in the response, as these were needed to relax the axial deformation caused by the first bending mode shape. As a result, no axial modes were needed within the AMF basis during the computation of the first NNM. The EMD method added seven axial modes (26, 39, 45, 47, 49, 51, 53) to define the initial axial deformation for the first NNM. The AMF needed fewer bending modes than EMD (4 compared to 11) as well, implying that coupling between bending modes was also implicitly accounted for through the preliminary static equilibrium.

The first three NNMs were computed with the AMF approach using a smaller maximum step size in order to more completely resolve the branches. (The same computation would have been much more expensive with the EMD approach so it was not pursued here.) A smaller maximum step size improved the ability of the continuation algorithm to capture the internal

resonances that emanate from the backbone since they can occur rather abruptly. Again, each nonlinear mode initiated at a single linear mode at low energy, initially requiring only one coordinate for iteration. The resulting frequency-energy plots are shown in Fig. 8. The energy at which each NNM solution vibrates at a maximum displacement amplitude of one beam thickness (0.031 inches or 0.787 mm) is clearly marked.

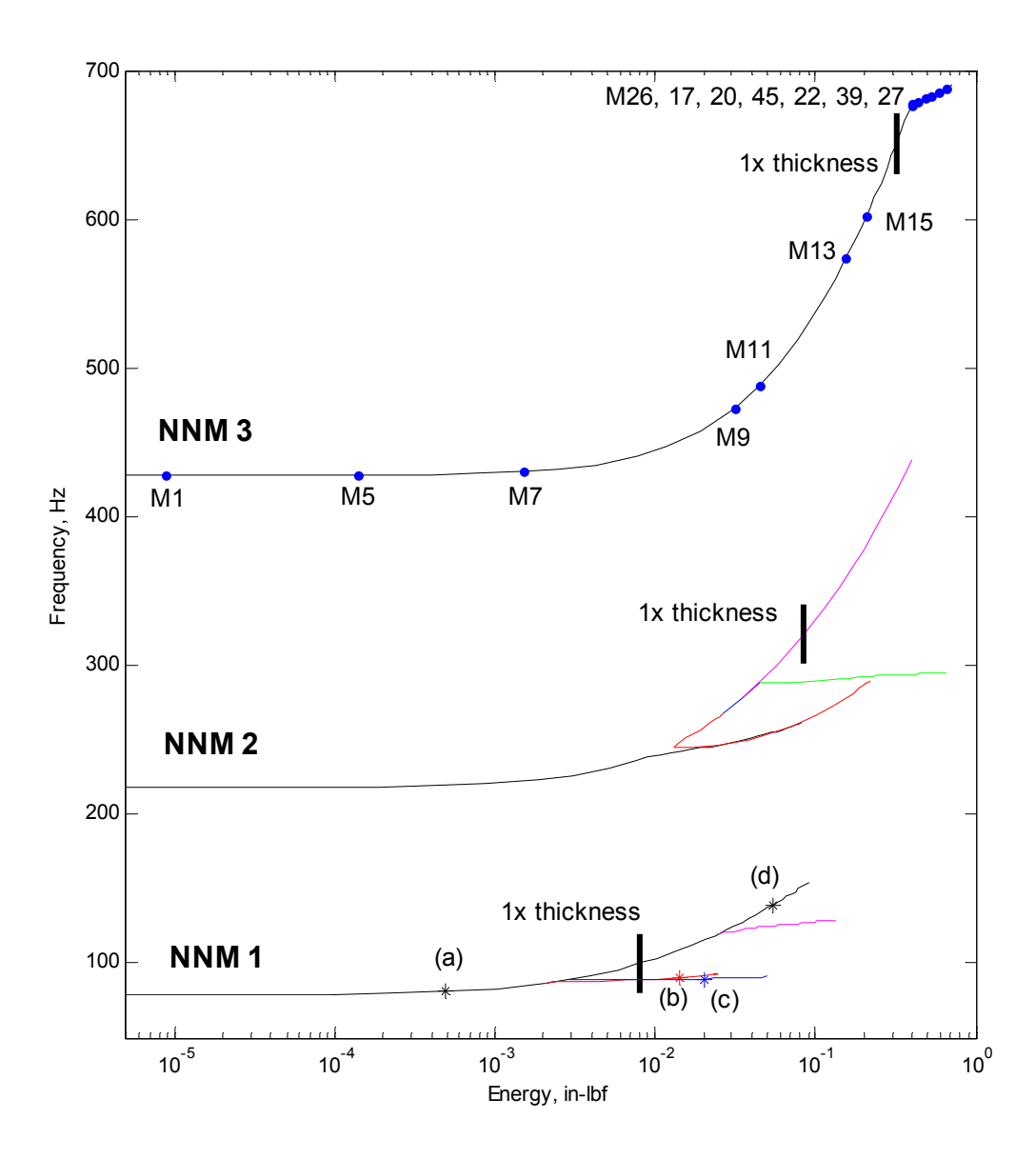


Figure 8. Frequency-energy plot of the first three nonlinear normal modes of a geometrically nonlinear beam using the AMF approach. Periodic motions (a-d) are plotted in Fig. 9.

Each color section of the FEPs in Fig. 8 represent a portion of the NNM that was continued from a new initial guess  $(\mathbf{q}_{0,(1)}, T_{0,(1)})$ . Each new portion of the branch required either an adjustment of the maximum prediction step size in order to more efficiently continue along an internal resonance, or a change in the direction of the prediction step. For example, the black curve of the NNM 2 branch started at low energy with a single mode, continued along the backbone and followed the first internal resonance. The algorithm was then manually terminated since the prediction step size was being reduced dramatically, and many modes were being added to satisfy convergence. A new solution was then initiated on the backbone, right before the tongue, with a large prediction step in order to find a new solution on the backbone beyond the first internal resonance. From that new point, the prediction step was reversed with a smaller step size, and the red curve was computed to resolve the internal resonance from the other direction. It would have been ideal to capture the entire NNM branch in one computation, but it seemed that when using Abagus as the integrator (rather than MATLAB as done in [49]) it was not possible to integrate with high enough accuracy to capture the 'turn' (fold bifurcation) at the end of the tongue. This strategy was relatively manual, and required that the user adjust the continuation settings (such as step size controller, etc.). In some cases it was observed that the pseudo-arclength continuation algorithm jumped from one branch to another. For example, the red curve representing an internal resonance along NNM 1 in Fig. 8 eventually would jump to a period multiple of the third NNM, where the response was integrated over 5 times the minimum period. When this occurred, the algorithm would be manually terminated and initiated at a different starting point.

The frequencies/energies where a mode was added for the computation of NNM 3 are marked in Fig. 8 where, for example, the M1 marker implies that the first linear mode was added

to the continuation variable set. The third NNM required a total of 15 modes with AMF to compute the branch up to 690 Hz, where continuation had followed a 5:1 internal resonance with NNM 9 until the algorithm was manually terminated. Along the backbone, the AMF algorithm automatically added only symmetric bending modes (1, 5, 7, 9, 11, 13, 15) to the basis, similar to the result of NNM 1 in Fig. 7. At the internal resonance, a few axial modes were added to the basis (such as modes 26, 45, 39). Due to the excessive number of modes added along the tongue, it was expected that these axial modes were mistakenly augmented to the continuation variable set when the algorithm was iterating to find a converged solution. While the add mode condition did not seem to be robust around the internal resonances, there was still a significant reduction in continuation variables to iterate on (15 variables compared to 117 with all physical DOF). This same behavior was also observed for other internal resonances in the first and second NNM. It is important to mention that for these NNMs, the excessive number of modes added along the internal resonance were not needed to satisfy shooting when the branch returned to the backbone.

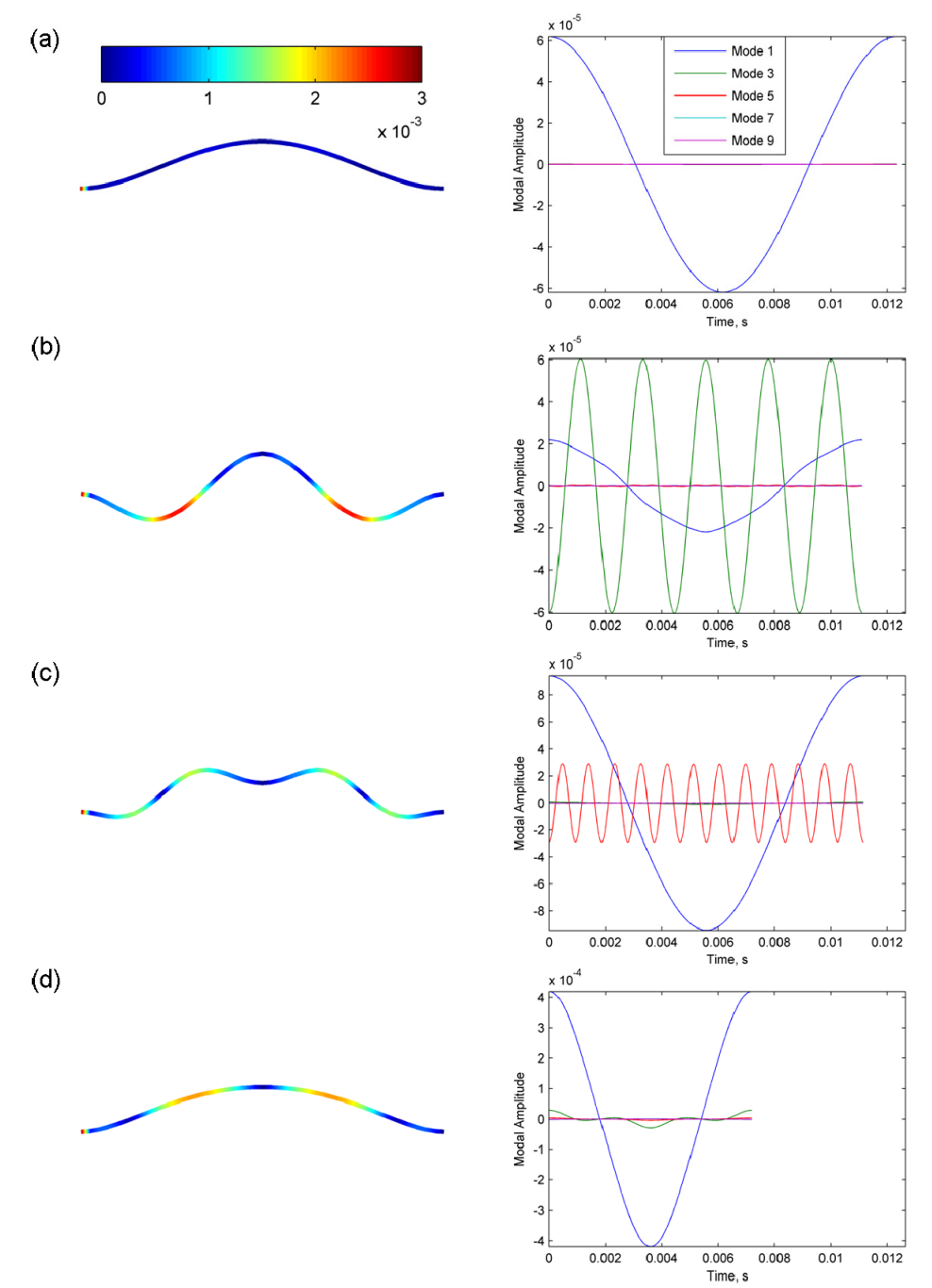


Figure 9. (Left column) Initial displacement shapes of clamped-clamped beam with increasing energy of discrete solutions along the NNM 1 branch marked with (\*) in Fig. 8. The color bar gives the ratio of in-plane displacement to transverse displacement at each point along the beam. (Right column) The time histories show the nonlinear response projected onto the first 5 symmetric bending modes.

A few of the solutions on the first nonlinear normal mode at the points marked with an asterisk (\*) in Fig. 8 are plotted in Fig. 9, showing the nature of the periodic response at these

points along the branch. At low energy, the time history and initial deformation of solution (a) was dominated by the first bending mode, and other modes had little contribution to the response. At a higher energy along the backbone, solution (d) shows a large shift in frequency, and higher order modes (mode 3 in particular) were clearly active in the time response, although the initial deformation mode shape has not changed dramatically. The initial deformation shapes reveal that the beam was deforming axially (the colorbar represents the ratio of axial to transverse displacement for each node) in order to obtain a free response that satisfied the shooting function at higher energy. The two solutions representing an internal resonance (solutions (b) and (c)) show the interaction between higher order modes that can only be explained with nonlinear normal mode theory. The time histories reveal that solution (b) is a 5:1 resonance with the third nonlinear mode, while solution (c) is a 12:1 internal resonance with the fifth nonlinear mode.

# 2.5 Application to Exhaust Cover Panel with Geometric Nonlinearity

The applied modal force algorithm was also used to compute the NNMs of a geometrically nonlinear finite element model of an exhaust cover plate, as a first step in diagnosing unexplained failures that had occurred in operation. Swept sine tests on a large shaker revealed that the frequencies of several of the resonances shifted significantly at the force levels of interest, and this was likely caused by geometric nonlinearities. The plate has a diameter of 12.5 inches (317.5 mm), with a uniform thickness of 0.06 inches (1.5 mm), and was modeled in Abaqus® with 899 S8R shell elements. The S8R element is an 8-noded thick shell element with reduced integration and shear flexibility. The mesh for this model is shown in Fig. 10 where there were a total of 15,708 DOF. Each element had the material property of structural steel with a mass density of 7.29·10<sup>-4</sup> lb-s<sup>2</sup>/in<sup>4</sup> (7,800 kg/m<sup>3</sup>) and a Young's modulus of 30,200 ksi (208

GPa). The entire bottom ring of the plate was fully constrained (i.e. all 6 DOF fixed), as if the plate were rigidly welded to an adjacent structure.

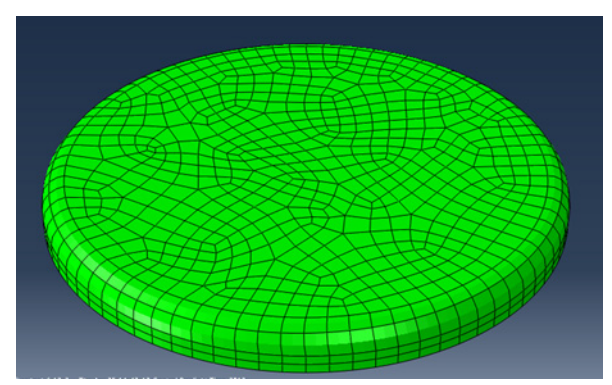


Figure 10. Finite element model of a geometrically nonlinear exhaust cover plate.

The FEP of the first NNM is plotted in Fig. 11, showing a frequency shift of 41% over the computed branch. The value for the shooting function tolerance was set to  $\varepsilon = 10^{-4}$ , with the same integration scheme and time steps used with the clamped-clamped beam in the previous section. A total of 500 modes were extracted from Abaqus, which could be added to the continuation variable set to define the initial conditions with the AMF approach. Each time integration (over one period) with this model took about 700 seconds, and every static solution took approximately 20 seconds. The total computational time for the FEP in Fig. 11 was approximately 4 days on the desktop computer mentioned earlier. As discussed in Section 2.3.5, this computational cost is conservative since the time histories were imported into MATLAB by reading/writing text files, which added some cost to the algorithm.

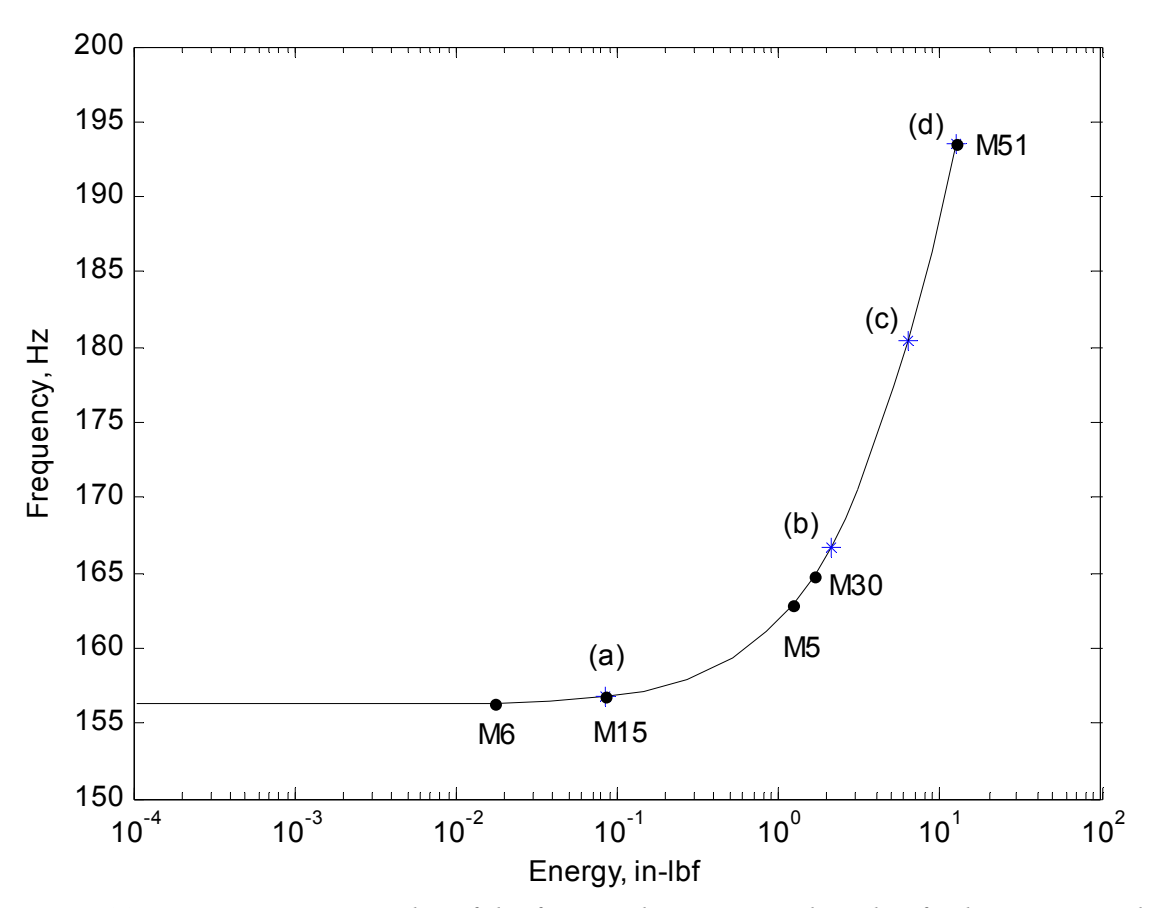


Figure 11. Frequency-energy plot of the first nonlinear normal mode of exhaust cover plate. Periodic motions (a-d) marked with (\*) are plotted in Fig. 13. (Note that 1 in-lbf = 0.113 N-m.)

The continuation algorithm added a total of 5 modes (mode 6, 15, 5, 30, 51) before the algorithm was manually terminated at a frequency of 193.6 Hz. This is an even more dramatic reduction compared to the beam for a model with a total of 15,708 DOF, illustrating how advantageous this approach is for finite element models with many DOF. The linear bending modes of the exhaust plate that were added to the algorithm to compute NNM 1 are shown in Fig. 12. Each of the bending modes are similar to that of the first linear mode (i.e. drum mode), except for mode 5.

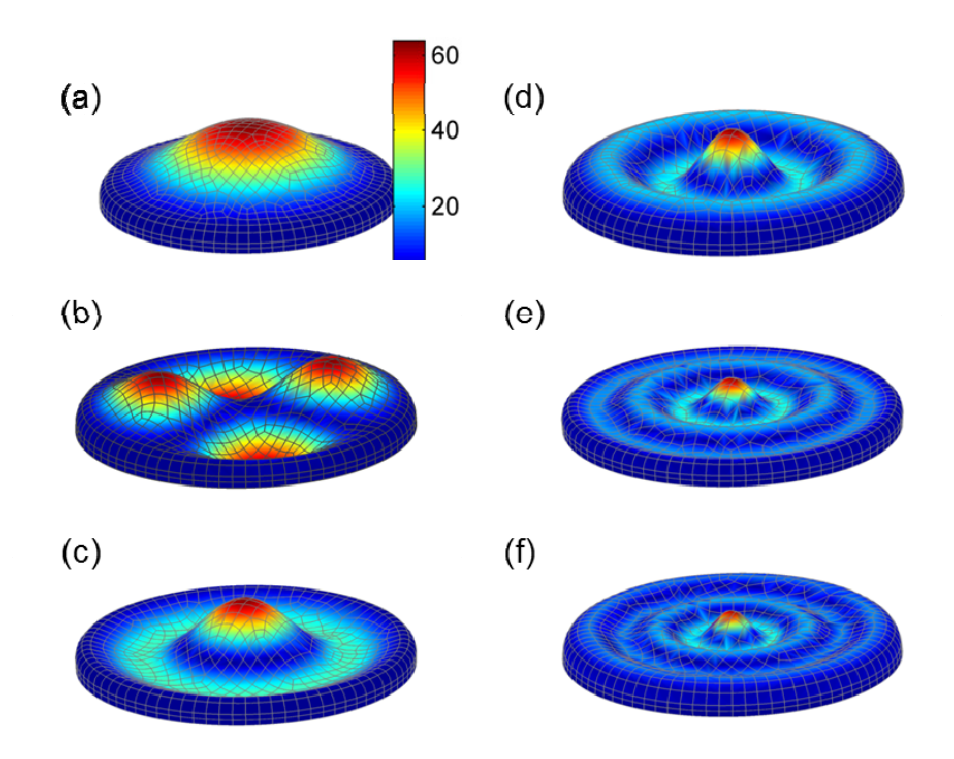


Figure 12. Linear (a) mode 1, (b) mode 5, (c) mode 6, (d) mode 15, (e) mode 30, and (f) mode 51 of exhaust cover plate that was added by the continuation algorithm to compute NNM 1. The color bar gives the amplitude of the out of plane displacement at each node.

The solutions marked with a (\*) in Fig. 11 represent four discrete periodic solutions, whose initial deformations are plotted in Fig. 13. The color bar in Fig. 13 represents the ratio of the axial deformation at each node relative to the transverse displacement along the top of the plate. The deformation shapes highlight the importance of the axial deformation in the initial conditions of the NNM as energy increased. At low energy, the plate bends with little accompanying axial stretch (Fig. 13a), about as much that is included in the first linear bending mode. Experience with the EMD algorithm revealed that axial deformation must be considered to compute the NNM out to a point where the natural frequency has shifted by less than 1%. More stretching was observed as energy increased, with the largest tension towards the outer edge of the plate. It is interesting to note how the deformations in Fig. 13(c) and (d) show the presence of the 6<sup>th</sup> linear bending mode in initial displacement. The other modes (15, 5, 30, 51)

are needed to satisfy the shooting function but their effect is not pronounced in the initial deformation shape. All of the modes required by the AMF algorithm were bending modes, as the membrane effects of the nonlinearity were implicitly included by first solving the static equilibrium problem. Based on the shape of the 5<sup>th</sup> bending mode, it is likely that this was unnecessarily added, but this was not a concern since the algorithm still provided a drastic reduction.

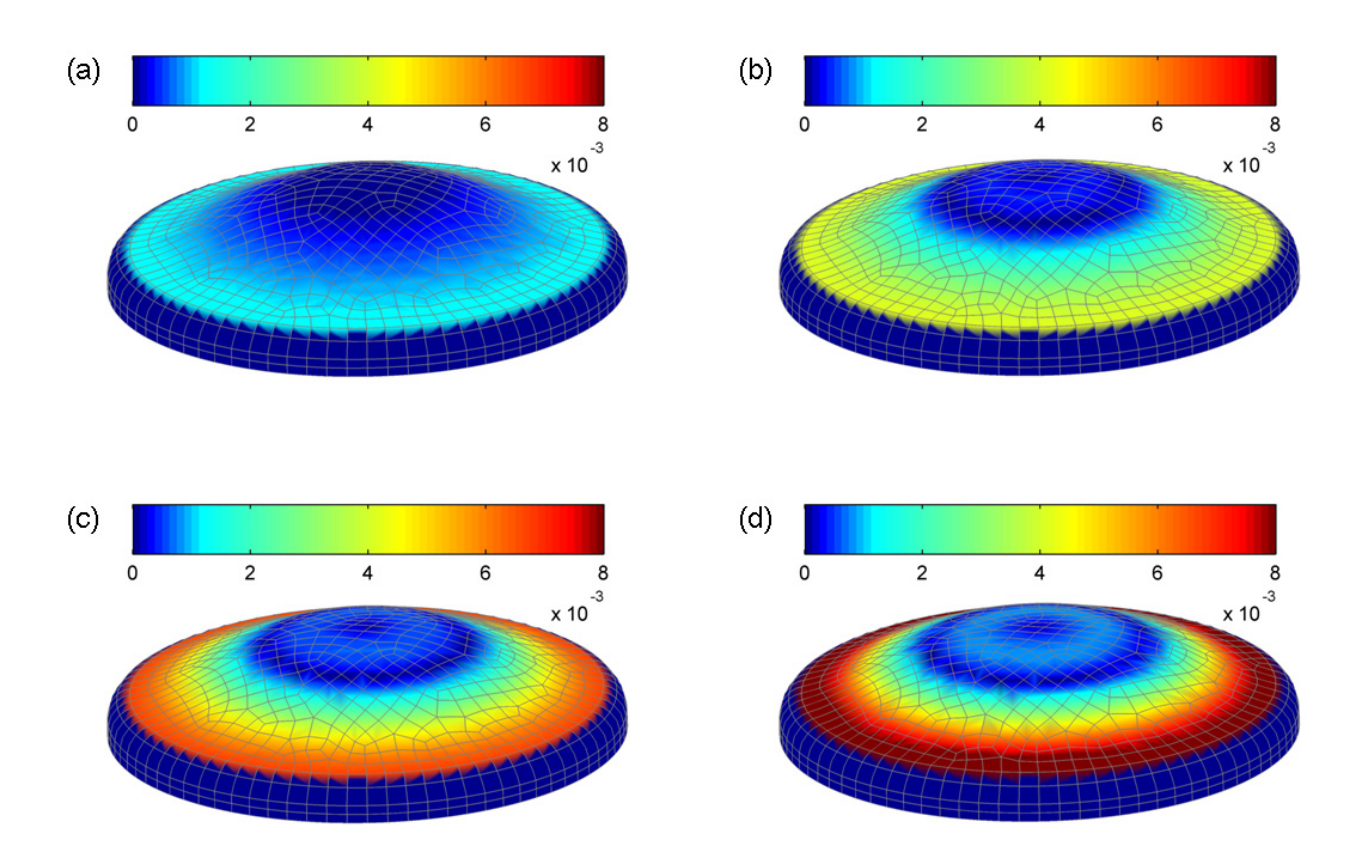


Figure 13. Initial displacement shapes of exhaust cover plate with increasing energy of discrete solutions along the frequency-energy plot in Fig. 11. The color bar gives the ratio of in-plane displacement to transverse displacement at each point along the plate.

The EMD approach would have required more modes, likely both axial and bending as seen with the clamped-clamped beam, in order to capture the deformations in Fig. 13. On the desktop computer mentioned earlier, one Jacobian of the exhaust plate model would take about

135 days with the approach in [49] (with all 15,708 DOF), whereas the Jacobian with the AMF approach (using 6 modes) took only 72 minutes. Each solution needed on average of 2-3 iterations within the correction step, and 1 prediction step (resulting in 3 to 4 Jacobian computations per solution). The AMF algorithm has a clear advantage for the computation of NNMs from finite element models with many DOF.

## 2.6 Summary

This chapter presented two numerical continuation approaches that can be used to compute the nonlinear normal modes of structures modeled in commercial, geometrically nonlinear finite element codes. These algorithms are an extension of the pseudo-arclength continuation algorithm developed by Peeters et al. [49] with two major differences. First, two approaches are used (AMF and EMD) to define the initial conditions based on a small subset of the underlying linear modal coordinates, resulting in a dramatic reduction in the number of variables that were varied within the continuation algorithm. Second, an add mode condition is included to automatically add modal coordinates to the reduced coordinate set as they are needed to satisfy convergence of the shooting function to a given numerical tolerance. The clampedclamped beam example in Section 2.4 showed a reduction from 117 DOF down to 4 DOF, and 18 DOF, respectively, for the AMF and EMD approaches. Furthermore, for the higher fidelity model of the exhaust plate in Section 2.5, only 6 modal coordinates were required with AMF compared to the 15,708 DOF that define the full order model, corresponding to almost a 3,000 fold decrease in the number of times that the response had to be integrated over one period at each iteration.

One interesting discovery with the two algorithms is that only a few linear modal coordinates were required to compute the nonlinear normal modes of these geometrically

nonlinear systems out to a significant shift in frequency. (In both cases, the NNMs were computed out to a frequency shift similar to the amount observed experimentally [35, 109, 110].) Even though the nonlinearity essentially couples all the underlying linear modal coordinates, only a few of these are important to compute the nonlinear normal modes. These solutions provide insight into which modes would be important to include in the kinematics of a reduced order model. The NNMs of the full order model are used throughout this dissertation to validate reduced models, providing a metric for comparison that is a unique signature of the nonlinear system.

# 3 Geometrically Nonlinear Reduced Order Models

#### 3.1 Introduction

This chapter reviews two indirect methods in the literature that generate reduced order models of geometrically nonlinear finite element models built directly within commercial FEA packages, as reviewed in [23, 24]. These methods project a set of Ritz vectors, or component modes, onto the nonlinear FEA equations of motion to obtain a set of low order, nonlinear modal equations. In commercially available FEA software, the linear mass and stiffness matrices can be readily exported, however the nonlinear stiffness terms due to geometric nonlinearity cannot. Therefore, an indirect approach is needed to estimate the nonlinear portion of the modal model (i.e. a quadratic and cubic polynomial function of modal coordinates) using a series of static load cases with either the applied loads procedure [19, 69, 103] or enforced displacements procedure [62, 72]. The resulting modal model offers significant computational savings for time response prediction compared to the direct integration of the full order model. Several existing works to date have reduced the monolithic FEA model with its linear vibrations modes [23, 62, 64, 65, 67, 69, 72], although with enforced displacements procedure, sometimes this basis can be augmented with a set of dual [67] or companion [23, 63] modes to capture in-plane kinematics.

These indirect nonlinear reduced order modeling (NLROM) strategies have been found to be sensitive to several factors such as the amplitudes of the loads used to fit the nonlinear stiffness coefficients, or the type and number of modes included in the basis. The inaccuracies of the resulting fit may only be visible at certain response levels due to the amplitude dependence of the NLROM. Relatively few works discuss the difficulties that can be encountered when seeking an accurate modal model, so this chapter comprehensively reviews all of the decisions that go

into the ROM, and how these models are used in the NNM framework. Past works have validated NLROMs experimentally or numerically by comparing time responses or the power spectrum of the response to a random input [19, 66, 108, 111]. Throughout this dissertation, the NNMs computed from candidate NLROMs generated with either the ED or ICE method are compared to the NNMs of the full order FEA model, which are computed using the applied modal force (AMF) algorithm in Chapter 2. The NNM offers a powerful metric to compare full and reduced order models since these solutions span a range of response amplitudes and are independent of any external forces.

## 3.2 Reduced Order Model Equations of Motion

The discretized system of equations for an N degree-of-freedom linear elastic, geometrically nonlinear finite element model can be written as

$$\mathbf{M}\ddot{\mathbf{x}} + \mathbf{K}\mathbf{x} + \mathbf{f}_{NL}(\mathbf{x}) = \mathbf{f}(t)$$
(29)

where  $\mathbf{M}$  is the  $N \times N$  mass matrix,  $\mathbf{K}$  is the  $N \times N$  linear stiffness matrix,  $\mathbf{f}_{NL}(\mathbf{x})$  is the  $N \times 1$  nonlinear restoring force vector, and  $\mathbf{f}(t)$  is the  $N \times 1$  external force vector. The  $N \times 1$  vectors  $\mathbf{x}$  and  $\ddot{\mathbf{x}}$  are the displacement and acceleration, respectively. The NLROM procedures seek to reduce these undamped, nonlinear equations using the linear vibration modes as the reduction basis, which are found by solving the eigenvalue problem  $(\mathbf{K} - \omega_r^2 \mathbf{M}) \mathbf{\varphi}_r$ . A small set of mass normalized mode shapes approximate the kinematics of the EOM as,

$$\mathbf{x}(t) = \mathbf{\Phi}_{m}\mathbf{q}(t) \tag{30}$$

Each column in the  $N \times m$  mode shape matrix,  $\Phi_m$ , is a mass normalized mode shape vector,  $\varphi$ , and  $\mathbf{q}$  is an  $m \times 1$  vector of time-dependent modal displacements. The vectors in  $\Phi_m$  are truncated to a small number of mode shapes (depending on the NLROM strategy used) such that the reduced coordinate space  $\mathbf{q}$  is significantly smaller that the physical coordinate space  $\mathbf{x}$  (i.e. m << N).

In order to reduce the full order equations of motion (EOM), the transformation in Eq. (30) is substituted into the full order EOM in Eq. (29) and premultiplied by  $\mathbf{\Phi}_m^{\mathrm{T}}$  to assure that the residual error is orthogonal to the reduction basis (note that ()<sup>T</sup> is the transpose operator). The reduced, nonlinear modal form of the  $r^{\mathrm{th}}$  equation becomes

$$\ddot{q}_r + \omega_r^2 q_r + \theta_r (q_1, q_2, \dots, q_m) = \boldsymbol{\varphi}_r^{\mathrm{T}} \mathbf{f}(t)$$
(31)

where  $\omega_r$  is the linear natural frequency, and  $q_r$  is the  $r^{th}$  modal displacement. The  $r^{th}$  nonlinear modal restoring force is given as

$$\theta_r(\mathbf{q}) = \mathbf{\phi}_r^{\mathrm{T}} \mathbf{f}_{NL}(\mathbf{\Phi}_m \mathbf{q}) \tag{32}$$

The nonlinear restoring forces are a nonlinear function,  $\theta_r(\mathbf{q})$ , of the modal displacements. Prior works [23, 24] have shown that if the finite element model is linear elastic with geometric nonlinearities derived using quadratic strain-displacement relationships, the function  $\theta_r(\mathbf{q})$  has the form of a quadratic and cubic polynomial given as

$$\theta_r(q_1, q_2, \dots, q_m) = \sum_{i=1}^m \sum_{j=i}^m B_r(i, j) q_i q_j + \sum_{i=1}^m \sum_{j=i}^m A_r(i, j, k) q_i q_j q_k$$
(33)

The coefficients  $B_r$  and  $A_r$  are the quadratic and cubic nonlinear stiffness coefficients, respectively, for the  $r^{th}$  nonlinear modal equation. If the full order EOM in Eq. (29) is known in closed form, then the nonlinear coefficients in Eq. (33) can be directly computed (referred as direct evaluation in [23]). However, this work is interested in models where the closed form equations are not explicitly available (e.g. within commercial finite element packages), and an indirect approach must be used. The coefficients are estimated using either the enforced displacements or Implicit Condensation and Expansion methods (otherwise known as the applied loads method) using a series of nonlinear static solutions of the full order model. Once these nonlinear stiffness terms are identified, the NLROM equations are completely given by Eqs. (31) and (33), which can be used for time response prediction at a significantly lower cost than compared to direct time integration of the full order model.

For the two NLROM methods discussed in this chapter, the linear term was set to  $\omega_r^2$  and treated as a known value during the identification of  $B_r$  and  $A_r$ . Originally, McEwan used a regression analysis to solve for the nonlinear stiffness coefficients using a set of applied load cases [69]. Further development of the Implicit Condensation method led Gordon and Hollkamp [19] to develop a constrained method where the nonlinear stiffness coefficients are directly solved with a least squares approach while enforcing certain relations between some of the  $B_r$  and  $A_r$  terms in order to preserve symmetry in the nonlinear stiffness matrices. This constrained approach is used in the results in Chapter 4 to determine the nonlinear coefficients for the ICE procedure, whereas the approach developed by Muravyov and Rizzi in [62] is used with the ED method.

## 3.3 Identification of Nonlinear Stiffness Coefficients

#### 3.3.1 Enforced Displacements Procedure

The enforced displacements procedure uses a set of prescribed displacements that are in a permutation of the sums and differences of either one, two or three of the mode shapes in the basis in Eq. (30). In general, the  $c^{th}$  multi-modal displacement combination of the  $r^{th}$ ,  $s^{th}$ , and  $p^{th}$  modes can be written as

$$\mathbf{X}_{c} = \mathbf{\varphi}_{r} \hat{q}_{r} + \mathbf{\varphi}_{s} \hat{q}_{s} + \mathbf{\varphi}_{p} \hat{q}_{p} \tag{34}$$

The  $N \times 1$  displacement vector  $\mathbf{X}_c$  is an enforced displacement field applied to the full order model, and the  $\hat{q}$ 's are the prescribed scaling factors for each mode. In order to accurately estimate the ROM, the scaling factors should scale the deformation shape of each mode to a level that exercises the geometric nonlinearity in the structure. Using the static solver in the finite element package, the resulting reaction force,  $\mathbf{F}_c$ , is computed in response to the  $c^{th}$  displacement field,  $\mathbf{X}_c$ . The estimation procedure in [62] uses a series of these enforced displacement fields that are in various combinations of one, two or three modes in the basis set. These displacements and the resulting reaction forces are used to identify the nonlinear stiffness coefficients from the quasi-static representation of the NLROM, where the  $r^{th}$  modal equation is given as

$$\omega_r^2 \hat{q}_r + \sum_{i=1}^m \sum_{j=i}^m B_r(i,j) \hat{q}_i \hat{q}_j + \sum_{i=1}^m \sum_{j=i}^m \sum_{k=j}^m A_r(i,j,k) \hat{q}_i \hat{q}_j \hat{q}_k = \mathbf{\phi}_r^{\mathsf{T}} \mathbf{F}_c$$
 (35)

The number of nonlinear static solutions, for m > 3, required by the ED method [24] is

$$2m + \frac{3m!}{2(m-2)!} + \frac{m!}{6(m-3)!} \tag{36}$$

#### 3.3.2 Applied Loads Procedure or Implicit Condensation and Expansion

The applied loads procedure is conceptually similar to the ED approach, but instead uses a set of static forces that are in a permutation of the sums and differences of either one, two or three of the mode shapes in the basis in Eq. (30). A multi-mode static force for the  $c^{th}$  load case can be written as a combination of the  $r^{th}$ ,  $s^{th}$ , and  $p^{th}$  modes as

$$\mathbf{F}_{c} = \mathbf{M} \Big( \mathbf{\varphi}_{r} \hat{f}_{r} + \mathbf{\varphi}_{s} \hat{f}_{s} + \mathbf{\varphi}_{p} \hat{f}_{p} \Big)$$
(37)

where  $\mathbf{F}_c$  is the  $N \times 1$  vector of static forces applied to the FEA model, and the  $\hat{f}$ 's are the force scaling factors for each mode. Note that existing works on the applied loads method do not mention the use of the mass matrix when computing the static force vector,  $\mathbf{F}_c$ , but it was used here and is needed to obtain a force that exactly isolates a single mode for a linear system (e.g. when  $\mathbf{f}_{NL}(\mathbf{x}) = \mathbf{0}$  in Eq. (29)). The force scaling factors should be selected to exercise the desired amount of geometric nonlinearity in the structure, as will be discussed further in Section 3.5. The resulting static deformation,  $\mathbf{X}_c$ , computed from the FEA static solver in response to the  $\mathbf{c}^{\text{th}}$  static force,  $\mathbf{F}_c$ , is then projected onto each of the linear modal coordinates in the basis as follows

$$q_r = \mathbf{\phi}_r^{\mathsf{T}} \mathbf{M} \mathbf{X}_c \tag{38}$$

Using a series of these applied forces and displacements, one can use the quasi-static form of the NLROM in Eq. (35) to solve for the nonlinear stiffness coefficients with the constrained least squares estimation procedure in [19]. With the applied loads approach, the number of load permutations (for m > 3) required to generate the static response data [19] is given as

$$2m + 2\frac{m!}{(m-2)!} + \frac{4m!}{3(m-3)!} \tag{39}$$

Regardless of the estimation procedure used to identify the nonlinear stiffness coefficients, there are many user decisions that are made by the analyst when creating these models. Inputs such as mode selection and static load scaling factors greatly affect the accuracy of the resulting NLROM, and are exploited when comparing the nonlinear normal modes computed from these reduced equations. Previous works [19, 62] have provided basic guidelines for the model reduction procedure, and many of these guidelines are comprehensively discussed below.

#### 3.4 Mode Selection

It is imperative to include all of the dynamically important modes in the reduced basis in Eq. (30) when creating the reduced order model, otherwise the NLROM will not be adequate for its intended purpose. For a linear system, one typically includes all of the excitable modes in a frequency range of interest to accurately capture the response of the model, however the addition of geometric nonlinearity requires further considerations. For example, the nonlinearity essentially couples the underlying linear modes of the structure, so additional modes outside the typical bandwidth of interest may be needed to account for such interactions. A low frequency mode can potentially excite a higher frequency mode outside of the desired excitation bandwidth and if the coupling is strong, these high frequency modes should be included in the basis set. For example, if the structure's nonlinearity is cubic, then it is well known that a periodic input at a frequency  $\omega$  may excite modes at higher harmonics such as  $3\omega$ ,  $5\omega$  and hence one may need to consider modes outside the bandwidth of the input forces to accurately capture the response of the structure.

The method used to estimate the NLROM coefficients (either ED or ICE) also has a strong influence on which modes to include. For example, the coupling between the bending and membrane motions cause "stretching" that is not always accurately captured with a set of low frequency bending modes. When using the enforced displacements procedure, high frequency membrane/axial modes must be explicitly included in the basis to account for the coupling. On the other hand, with the Implicit Condensation and Expansion method, membrane modes do not need to be included since the softening due to membrane stretching is implicitly captured during the identification of the nonlinear stiffness coefficients. Nonlinear systems are also known to exhibit modal interactions, where an NNM at a given energy level can exchange energy with a different NNM [25, 38]. In order to capture this phenomena, the NLROM must include the mode shapes/kinematics that are involved in the modal interaction. In theory, an infinite number of interactions may exist for even the simplest systems, but certain ones may likely be more important than others.

A few methods have been proposed to identify a sufficient modal basis for the NLROM. For example, Rizzi and his colleagues presented an approach in [66, 111] that uses a short dynamic response to a representative loading to determine which modes significantly contribute to that response. This dissertation proposes an alternate approach to identify which modes are nonlinearly coupled to each of the bending modes of interest based on nonlinear static solutions. A force proportional to a single, linear mode shape,  $\varphi_r$ , is scaled with a scale factor,  $\hat{f}_r$ , which is chosen to ensure the geometric nonlinearity is sufficiently excited (see Section 3.5.2). This force is applied to the nonlinear FEA model and the nonlinear static response to the given force reveals which axial and bending modes couple to the  $r^{th}$  bending mode of interest. Specifically,

the FEA software solves the following static equation, where external force is applied in the shape of the  $r^{th}$  linear mode,

$$\mathbf{KX}_{static} + \mathbf{f}_{NL} \left( \mathbf{X}_{static} \right) = \mathbf{M} \boldsymbol{\varphi}_r \hat{f}_r$$
(40)

The displacement,  $\mathbf{X}_{\textit{static}}$ , resulting from the static force is then projected onto all the modal coordinates as

$$\mathbf{q} = \mathbf{\Phi}^{\mathsf{T}} \mathbf{M} \mathbf{X}_{static} \tag{41}$$

If the force amplitude is too small (in the linear regime), the applied force will result in a displacement exactly in the  $r^{th}$  mode shape and hence only  $q_r$  will be nonzero. For larger force amplitudes, the nonlinear static solution reveals the natural coupling between that mode and other bending and membrane modes due to the geometric nonlinearity. The modal amplitudes in Eq. (41) guide the selection of the appropriate modes to supplement each linear mode that falls in the frequency range of interest. Consider the computation of the  $r^{th}$  nonlinear normal mode initiated at the  $r^{th}$  linear mode at low energy. The NNM can be checked for convergence by adding the linear mode with the next largest value in the  $\bf q$  vector in Eq. (41) to the NLROM basis in Eq. (30), and then recomputing NLROM and its NNM. If the additional mode improves the resulting NNM, then that mode should be included in the basis set. This procedure helps identify when a sufficient basis set has been selected to capture the  $r^{th}$  NNM. This can be used for both the ED and ICE procedures, and will be demonstrated throughout the results in Chapter 4.

## 3.5 Scaling Factors for Multi-Mode Models

The scaling factors on the static load cases in Eq. (34) for ED and Eq. (37) for ICE govern the degree to which the nonlinearity in the FEA model is activated in the response data used to fit the nonlinear stiffness coefficients. If the scale factors are too small, the nonlinearity in the response may be on the order of computational noise leading to numerical difficulty when attempting to determine the polynomial coefficients  $A_r$  and  $B_r$ . Similar problems may result if one mode is excited far more or far less than the others. This section discusses the suggested approaches for selecting the scale factors with the ED and ICE estimation procedures.

#### 3.5.1 Enforced Displacement Scaling Factors

One scaling approach, termed the constant modal displacement (CD) factor, sets the scaling factors,  $\hat{q}$ , in Eq. (34) for each mode in a meaningful way. The modal scale factor required to displace the  $r^{\text{th}}$  mode to a desired maximum displacement in physical coordinates,  $w_{\text{max}\,r}$ , can be written as

$$\hat{q}_r = CD_r = \frac{w_{\text{max},r}}{\mathbf{\Phi}_{r,\text{max}}} \tag{42}$$

The scalar  $\varphi_{r,\max}$  is the maximum displacement value (i.e. ignoring any rotations) of the  $r^{\text{th}}$  mass normalized mode shape in the basis. Note that generally the maximum displacement occurs at a different displacement DOF for each mode, and that different values of  $w_{\max,r}$  may be chosen depending on the mode of interest. For example, if the scaling factor is for a bending mode, choosing a  $w_{\max,r}$  value on the order of the thickness of the structure will typically assure that the displacements exercise the nonlinearity. For an axial mode, then a value on the order of a

fraction of the thickness (a tenth or hundredth) should be used since these modes do not behave nonlinearly and unreasonably large forces would be needed to cause them to displace by one thickness, possibly introducing numerical ill-conditioning into the estimation process.

The works in [62, 65] suggest that the ED NLROM obtained is theoretically insensitive to the amplitudes of  $\hat{q}$ , however should be chosen to be physically reasonable and within the range of interest. For the enforced displacement procedure, they proposed using the same scaling factor for all modal displacements in Eq. (34). This method will be referred to as the constant modal scale (CS) factor method, where the scale factors are determined based on the maximum displacement of the lowest order bending mode as

$$\hat{q}_r = CS_r = CD_1 \tag{43}$$

where  $CD_1$  is given by Eq. (42). It is suggested that  $w_{\text{max},1}$  is chosen to be physically reasonable for the lowest frequency bending mode and within the range of displacements expected in the application of interest. The results in Chapter 4 explore the results obtained by each approach and discuss some of the issues that arise.

It is noted that Mignolet, Perez, Wang and others have also employed the enforced displacements procedure successfully with many structures [24, 72, 102, 112]. They typically set  $CD_r$  for each mode such that each bending mode displaces 1.0 times the thickness and a displacement < 1.0 times the thickness for the membrane/axial modes. The optimal CD values are problem dependent and so they typically employ a few values near 1.0 thickness and check whether the ROM coefficients vary significantly. They also typically use the "cleaning" procedure described in [112] to zero out any cubic  $A_r$  and quadratic  $B_r$  terms involving only one axial mode. Finally, it should be noted that their approach to determine the ROM

coefficients differs slightly from that outlined in this chapter; they estimate both the linear and nonlinear stiffness coefficients in the ROM from the results of the static load cases (in this dissertation, the linear terms were always set to  $\omega_r^2$ ). They compared the linear terms against the known linear natural frequencies to check the consistency of the results; they may vary from the linear natural frequencies if too large of loads have been applied. This approach was not implemented in this work, but it should be kept in mind as it may explain some of the differences between the scaling values that worked best in Chapter 4 and those reported in their works.

### 3.5.2 Applied Load Scaling Factors

For the applied loads procedure, Gordon and Hollkamp specify scaling factors based on the amount of force required to achieve a certain maximum displacement for the linear system [19]. The equation for the scaling factor of the  $r^{th}$  mode shape based on the load case in Eq. (37) is formulated as

$$\hat{f}_r = CLD_r = \frac{w_{\text{max},r}}{\mathbf{\phi}_{r,\text{max}}} \omega_r^2 \tag{44}$$

This method of scaling is termed constant linear displacement (CLD). Note that this equation is slightly different than the equation presented in [19] due to the mass matrix being pre-multiplied by the force vector in Eq. (37). The desired linear displacement for each mode should sufficiently excite the geometric nonlinearity. Typically a displacement on the order of one thickness is used for the primary, low frequency modes [19], however, higher frequency modes tend to require a lower  $w_{\text{max},r}$  value. It is important to select a displacement amplitude,  $w_{\text{max},r}$ , large enough to overcome the linear range of the response, but small enough to avoid convergence issues with the finite element solution. One recommendation for determining  $w_{\text{max},r}$ 

for each mode is to compute the nonlinear static solution to the force in Eq. (40), and find the resulting maximum *nonlinear* displacement,  $w_{\max,r,NL}$ . The ratio of the nonlinear to linear maximum displacement is defined as the ratio

$$\gamma_r = \frac{W_{\text{max},r,NL}}{W_{\text{max},r}} \tag{45}$$

Typically, the ratio for  $\gamma_r$  should be between 0.8 and 0.95 for hardening nonlinearities, or 1.05 to 1.2 for softening nonlinearities [19].

Another important issue arises when determining the load cases that involve a combination of two or three modes simultaneously. After determining the CLD scaling factors for each mode in the basis, a reduction of these force amplitudes is recommended here. For example, when applying a load in the combination of modes 1 and 2, the CLD factors should be reduced by a factor of two such that the loading becomes

$$\mathbf{F}_c = \mathbf{M} \left( \mathbf{\phi}_1 \cdot \frac{1}{2} \hat{f}_1 + \mathbf{\phi}_2 \cdot \frac{1}{2} \hat{f}_2 \right) \tag{46}$$

Similarly for combinations of three modes, each CLD factor should be reduced by a factor of three. This ensures that the applied forces do not exceed desired displacement levels, and contaminate the fit of the nonlinear stiffness coefficients. This method is termed the reduction factor (RF) method.

## 3.6 Nonlinear Normal Modes of Reduced Order Models

Once the NLROM equations are identified using either parameter estimation procedure, the NNMs of the modal equations are computed using the pseudo-arclength continuation algorithm in [49]. From the equations of motion in Eqs. (31) and (33), there exist at least m

nonlinear normal modes that are extensions of the linear modes in the basis. The continuation algorithm uses the linear mode solution at low response amplitude as an initial guess, and the predictor-corrector type algorithm traces the periodic solutions as the response amplitude increases. The method relies on the shooting technique to find the periodic solutions of the equations of motion, using the shooting function

$$\mathbf{H}(T, \mathbf{q}_{0}, \dot{\mathbf{q}}_{0}) = \begin{cases} \mathbf{q}(T, \mathbf{q}_{0}, \dot{\mathbf{q}}_{0}) \\ \dot{\mathbf{q}}(T, \mathbf{q}_{0}, \dot{\mathbf{q}}_{0}) \end{cases} - \begin{Bmatrix} \mathbf{q}_{0} \\ \dot{\mathbf{q}}_{0} \end{Bmatrix} = \mathbf{0}$$

$$(47)$$

A valid NNM is defined as a periodic motion with integration period T, initial modal displacement  $\mathbf{q}_0$ , and initial modal velocity  $\dot{\mathbf{q}}_0$  that satisfies the shooting function to a given numerical tolerance. The algorithm in [49] iterates on these variables  $(T, \mathbf{q}_0, \dot{\mathbf{q}}_0)$  using a Newton-Raphson method to search for a response that satisfies Eq. (47). Once a periodic solution is found, the solution is stored and the algorithm predicts a new solution along a line tangent to the current branch. The correction step is repeated by adjusting the predicted solution until the shooting function is again satisfied.

One advantage to the numerical continuation approach is that it can handle strong nonlinearities since each periodic solution is exact to a given integration tolerance. Unfortunately, the cost of the algorithm grows in proportion to the number of DOF in the model. NLROMs have the computational advantage of having far fewer DOF compared to the full finite element model, making the NNM computation very efficient. Furthermore, the Jacobian of the NLROM can be derived analytically from Eqs. (31) and (33), so the method in [49] is used to further speed up the computations, compared to the finite difference approach used in Chapter 2. Hence, this is a very efficient means of computing the NNMs of a geometrically nonlinear

structure, the only question is whether the NLROM is an accurate representation of the FEA model of interest.

## 3.7 Expansion of In-Plane Displacements for Applied Loads

As stated earlier, the applied loads approach condenses the quasi-static membrane effects induced by large bending amplitudes into the nonlinear stiffness coefficients of the modal models. The advantage to this is that the membrane type modes do not need to be explicitly included in the basis set, allowing for a lower order ROM. Membrane or axial modes typically have much higher frequencies and require shorter time steps during numerical integration. When recovering the displacements in physical coordinates using the modal coordinates in Eq. (30), the transformation does not necessarily contain the correct membrane kinematics that are excited by the bending-membrane coupling. Hence, those displacements cannot be used to recover accurate stresses and strains from the FEA model as a post-processing step. Hollkamp and Gordon developed a remedy by recovering these membrane motions when expanding back to physical coordinates [103]. They estimate a set of membrane basis vectors that account for membrane stretching, and are related to the physical deformations as functions of the bending modal coordinates. Each modal model has its own unique set of expanded membrane basis vectors depending on the bending modes used in the basis, and are only needed when recovering physical displacements as a post-processing step.

The derivation of the expanded membrane motions from [103] is summarized here. The transformation in Eq. (30) is augmented with membrane motions so it becomes

$$\mathbf{x} \approx \mathbf{\Phi}_{m} \mathbf{q} + \mathbf{T}_{m} \mathbf{p} \tag{48}$$

The  $N \times k$  matrix  $\mathbf{T}_m$  contains k membrane basis vectors, one in each column, and the  $k \times 1$  vector  $\mathbf{p}$  contains the generalized membrane coordinates. The membrane motions are found by returning to the results of the static load cases performed to create the ROM. Each static deformation,  $\mathbf{X}_c$ , to a modal force in Eq. (37) is assumed to be well approximated using the expanded basis

$$\mathbf{X}_c \approx \mathbf{\Phi}_m \mathbf{q}_c + \mathbf{T}_m \mathbf{p} \tag{49}$$

where  $\mathbf{q}_c$  are the modal amplitudes of each mode contributing to the response in  $\mathbf{X}_c$  computed using the modal filter in Eq. (38). The entire series of static solutions used to fit the nonlinear stiffness coefficients are considered simultaneously by collecting all columns of Eq. (49).

$$\mathbf{X}_{static} \approx \mathbf{\Phi}_{m} \mathbf{Q} + \mathbf{T}_{m} \mathbf{P} \tag{50}$$

The columns of the matrices  $\mathbf{X}_{static}$ ,  $\mathbf{Q}$ , and  $\mathbf{P}$  represent the individual static solutions to the load cases defined by Eq. (37). Assuming there are a total of l static load cases (see Eq. (39)), the dimensions of each matrix are  $N \times l$ ,  $m \times l$ , and  $k \times l$ , respectively.

It is assumed that the membrane basis vectors in  $\mathbf{T}_m$  are orthogonal to the mode shapes in  $\mathbf{\Phi}_m$ , allowing the modes to be projected onto the physical displacements as

$$\mathbf{Q} = \left(\mathbf{\Phi}_{m}^{\mathsf{T}} \mathbf{\Phi}_{m}\right)^{-1} \mathbf{\Phi}_{m}^{\mathsf{T}} \mathbf{X}_{static} \tag{51}$$

Note that the matrix,  $\mathbf{Q}$ , can also be computed as  $\mathbf{Q} = \mathbf{\Phi}_m^T \mathbf{M} \mathbf{X}_{static}$  if the basis in  $\mathbf{\Phi}_m$  are linear, mass normalized vibration modes. Assuming now that the generalized membrane amplitudes are known, the membrane basis could theoretically be estimated from

$$\mathbf{T}_{m} \approx \left(\mathbf{X}_{static} - \mathbf{\Phi}_{m} \mathbf{Q}\right) \mathbf{P}^{\mathrm{T}} \left(\mathbf{P} \mathbf{P}^{\mathrm{T}}\right)^{-1}$$
(52)

Following the approach developed in [103], a quadratic relationship is assumed between the modal coordinates in  $\mathbf{q}$  and the generalized membranes amplitudes  $\mathbf{p}$  such that

$$\mathbf{p} = \begin{bmatrix} q_1^2 & q_1 q_2 & q_1 q_3 & \dots & q_1 q_m & q_2^2 & q_2 q_3 & \dots & q_2 q_m & \dots & q_{m-1}^2 & q_{m-1} q_m & q_m^2 \end{bmatrix}^{\mathrm{T}}$$
(53)

The expanded membrane motions can now be estimated using Eqs. (51) to (53). Once a solution to the NLROM in Eqs. (31) and (33) has been integrated, the resulting physical displacements can be expanded as a post-processing procedure using Eq. (48) in order to accurately compute the stress and strain in each finite element. These generalized membrane coordinates are not included explicitly in the nonlinear differential equations, so there is no increase in order size of the system being integrated.

## 4 Convergence Evaluation of Monolithic Nonlinear Reduced Order Models

### 4.1 Introduction

This chapter uses the nonlinear normal modes as a metric to determine the convergence of a ROM either as modes are added to the basis, or as the amplitudes change on the static loads used to identify the nonlinear stiffness coefficients. The enforced displacement and Implicit Condensation and Expansion parameter estimation approaches are evaluated here on the two geometrically nonlinear finite element models presented in Chapter 2. The first is a flat planar beam with 117 DOF and clamped-clamped boundary conditions, while the second is a more complicated FEA model of an exhaust cover plate with 15,708 DOF. The NLROMs were created for each model with different modes and scaling factors, and then the NNMs were computed and compared to gain insight into the convergence and accuracy of the models. These results are compared with the true NNMs computed from the full order models using the applied modal force (AMF) algorithm in Chapter 2. In practice, these solutions will not necessarily be available since this truth data is computationally expensive, however the ROM can still be validated based on how the NNMs converge as the modal models are refined. For the development of this research, it is informative to have these reference NNMs from the full order model.

A third case study is presented in this chapter using a linear beam model with a local contact nonlinearity modeled as a unilateral piecewise-linear spring. The reduced order models of this system are generated using a Galerkin approach with linear vibrations modes augmented with a single discontinuous basis function, as done in [113]. The NNMs are computed from a candidate set of ROMs with a successively increasing number of vibration modes in the basis, and the accuracy of the ROMs are evaluated based on the convergence of the resulting NNMs.

No reference NNMs were available from the full order model, so the effectiveness of the NNM convergence metric is evaluated by comparing the response of the ROMs to the full order model for both an impulsive load and a random input.

## 4.2 Application to Clamped-Clamped Beam with Geometric Nonlinearity

The beam model studied here was identical to that in [23], and had the following dimensions: 9 inches (229 mm) long, with a cross section of 0.5 inches (12.7 mm) wide by 0.031 inches (0.787 mm) thick. It was modeled with forty B31 beam elements in Abaqus®, resulting in 117 DOF. It was constructed of steel with a Young's modulus of 29,700 ksi (204.8 GPa), a shear modulus of 11,600 ksi (80.0 GPa) and a mass density of  $7.36 \cdot 10^{-4} \, \text{lb-s}^2/\text{in}^4$  (7,870 kg/m³). The geometrically nonlinear beam exhibited hardening nonlinearities, as shown in Chapter 2, due to the coupling between bending and membrane motions at large response amplitudes.

First, the modal coupling due to the geometric nonlinearity was investigated by applying a static force proportional to the first five symmetric bending modes, and projecting the displacement onto the mass normalized linear modes using Eq. (41). As in [23], it was presumed that the anti-symmetric modes will not be excited and hence are not of interest. The force was scaled for each of the modes using the CLD method in Eq. (44) with a  $w_{\text{max},r}$  value of 0.031 inches (0.787 mm), or 1 beam thickness. The magnitude of the resulting modal amplitudes were normalized to the largest amplitude, and sorted in descending order in Table 3. An applied static force meant to excite the first linear mode revealed nonlinear coupling to other symmetric bending modes (modes 3, 5, 7, 9, etc..). In addition, anti-symmetric axial modes 26, 39, 45 and 47 were found to be coupled to it as well. The results suggest which axial/membrane modes to augment with the bending modes for the ED procedure, as well as which bending modes to

successively include in the basis set for either the ED or ICE method in order to get convergence of the NLROM.

Table 3. Relative modal amplitude due to a static force applied to excite the linear mode shapes of the clamped-clamped beam.

Force in Mode 1		Force in Mode 3		Force in Mode 5		Force in Mode 7		Force in Mode 9	
Mode #	Amp	Mode #	Amp	Mode #	Amp	Mode #	Amp	Mode #	Amp
1	1	3	1	5	1	7	1	9	1
3	$9.3 \cdot 10^{-3}$	1	5.7·10 <sup>-1</sup>	1	$6.8 \cdot 10^{-1}$	1	$7.2 \cdot 10^{-1}$	1	$7.4 \cdot 10^{-1}$
5	$1.3 \cdot 10^{-3}$	5	$2.4 \cdot 10^{-2}$	3	$2.0 \cdot 10^{-1}$	3	$2.6 \cdot 10^{-1}$	3	$2.9 \cdot 10^{-1}$
39	5.0.10-4	7	$7.2 \cdot 10^{-3}$	7	$2.6 \cdot 10^{-2}$	5	1.1.10-1	5	1.4·10 <sup>-1</sup>
7	$3.1 \cdot 10^{-4}$	9	$2.7 \cdot 10^{-3}$	9	$1.1 \cdot 10^{-2}$	9	$2.5 \cdot 10^{-2}$	7	$7.6 \cdot 10^{-2}$
26	$2.4 \cdot 10^{-4}$	47	$1.5 \cdot 10^{-3}$	11	$5.3 \cdot 10^{-3}$	11	$1.3 \cdot 10^{-2}$	11	$2.3 \cdot 10^{-2}$
9	9.9.10-5	11	$1.1 \cdot 10^{-3}$	13	$2.7 \cdot 10^{-3}$	13	$7.1 \cdot 10^{-3}$	13	$1.4 \cdot 10^{-2}$
45	$6.7 \cdot 10^{-5}$	45	$9.8 \cdot 10^{-4}$	51	$2.6 \cdot 10^{-3}$	15	$4.1 \cdot 10^{-3}$	15	$8.2 \cdot 10^{-3}$
11	$3.9 \cdot 10^{-5}$	13	$5.5 \cdot 10^{-4}$	49	$1.9 \cdot 10^{-3}$	55	$3.6 \cdot 10^{-3}$	17	$5.1 \cdot 10^{-3}$
13	1.8 · 10 - 5	49	$4.1 \cdot 10^{-4}$	15	$1.5 \cdot 10^{-3}$	53	$2.9 \cdot 10^{-3}$	59	$4.7 \cdot 10^{-3}$
47	$1.7 \cdot 10^{-5}$	15	$2.9 \cdot 10^{-4}$	26	$1.1 \cdot 10^{-3}$	17	$2.5 \cdot 10^{-3}$	57	$3.9 \cdot 10^{-3}$

#### 4.2.1 One-Mode NLROMs

A one-mode NLROM was first generated using the ED and ICE procedures, and the NNMs were computed from the resulting equations and are shown in Fig. 14. The CLD factor was used with ICE, where the  $w_{\text{max,l}}$  value was set to a displacement of 0.5 times the beam thickness, or 0.016 inches (0.394 mm). The ratio of nonlinear to linear displacement at the midpoint with this scale factor was  $\gamma_1$ =0.88. For the ED NLROM, a CD scale factor that produced a maximum displacement such that  $w_{\text{max,l}}$  was 3 times the thickness was used. The reason for selecting these optimal values is addressed later in this subsection. The legend for each NLROM in Fig. 14 uses the following convention: "NLROM strategy (modes included) scaling method ( $w_{\text{max,r}}$ /beam thickness x Number of modes with that ratio)." For example, the last line in the legend in Fig. 14 represents an enforced displacement NLROM (ED) which includes modes 1, 26, and 39 using the constant displacement scale factor method (CD) with

 $w_{\text{max},1}$  set to 3 times the beam thickness for the first mode in the basis set (mode 1) and  $w_{\text{max},26}$  and  $w_{\text{max},39}$  set to 0.01 times the beam thickness for the two (x2) axial modes (modes 26 and 39).

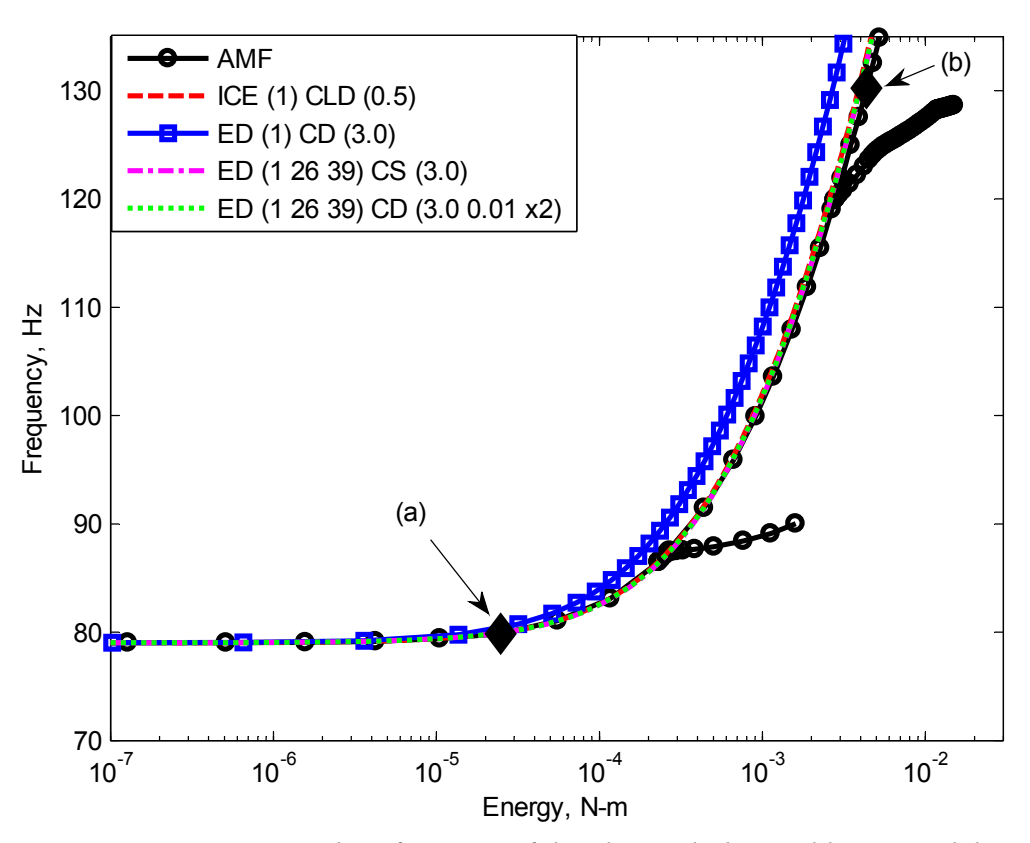


Figure 14. Frequency-energy plot of NNM 1 of the clamped-clamped beam model with various NLROM strategies. Deformations of solutions (a) and (b) are plotted in Fig. 15.

The NNM is shown on the frequency-energy plane, where each point along the curve represents a periodic solution to the nonlinear equations. The fundamental frequency on the vertical axis was computed from the minimum period of the response (higher harmonics were generally observed as energy increased). The energy along the horizontal axis was computed as the total energy, kinetic plus potential, of the system during the periodic response. The results in Fig. 14 show that a one-mode NLROM created using the ICE procedure (dashed red) accurately captured the backbone of the first NNM when compared to the truth results from AMF (black circles). At higher energies (above 0.003 N-m), the one-mode ICE NLROM was slightly stiffer

than the true NNM. As expected, a comparable one-mode model created using the enforced displacement procedure (blue squares) was much stiffer and hence much less accurate than the ICE NLROM over the whole energy range due to the lack of membrane-softening in the basis. It is well known that membrane modes must be included in an ED NLROM in order to obtain accurate results; the results above exploit the error that is incurred when the membrane modes are neglected.

The ED NLROM was improved by adding the first two anti-symmetric axial modes to the basis set (modes 26 and 39), as determined by the coupling in Table 3. Two different scaling methods were used with the NLROMs that included these axial modes: CS scaling, and also CD scaling with  $w_{\text{max},r}$  set to 3 times and 0.01 times the beam thickness for the first bending mode and the associated axial modes, respectively. After adding these two axial modes, either of the ED NLROMs were as accurate as the one-mode ICE NLROM. This illustrates the fact that the membrane displacements must be included in the basis set for the ED method in order to accurately capture the nonlinear stiffness, whereas the ICE method implicitly captured these effects. For this NNM no difference was seen between the results obtained using the CD (short dashed green) and CS (dashed dot magenta) scaling methods. Hence, when using the enforced displacements approach the higher frequency axial modes can be displaced much less than the bending modes during the static load cases and produce an accurate NLROM.

All of these approaches gave an excellent estimate for the backbone of NNM 1, even though the NLROMs only included the first bending mode. The ED procedure was at a slight disadvantage since it required the axial modes explicitly in the basis set, but in this case these modes were easily identified using a statically applied force in the shape of the first bending mode as shown in Table 3. The dual modes method proposed by Kim, Mignolet et al. [67] would

likely include similar axial effects, but this basis was not explored in this work. Each NLROM captured the bending-membrane coupling caused by geometric nonlinearity, and was examined more thoroughly by looking at the physical deformations at different points along the NNM branch. The plot in Fig. 15 shows the maximum deformation shape (e.g. when the velocity of the periodic response was zero) at the points marked (a) and (b) in Fig. 14 for the ICE and ED methods, as well as the AMF truth results (note that the expansion method in Section 3.7 had to be used to capture the membrane deformations with ICE). The position of each node is plotted in millimeters, and the color bar shows the log of the ratio of in-plane displacement to transverse displacement at each node.

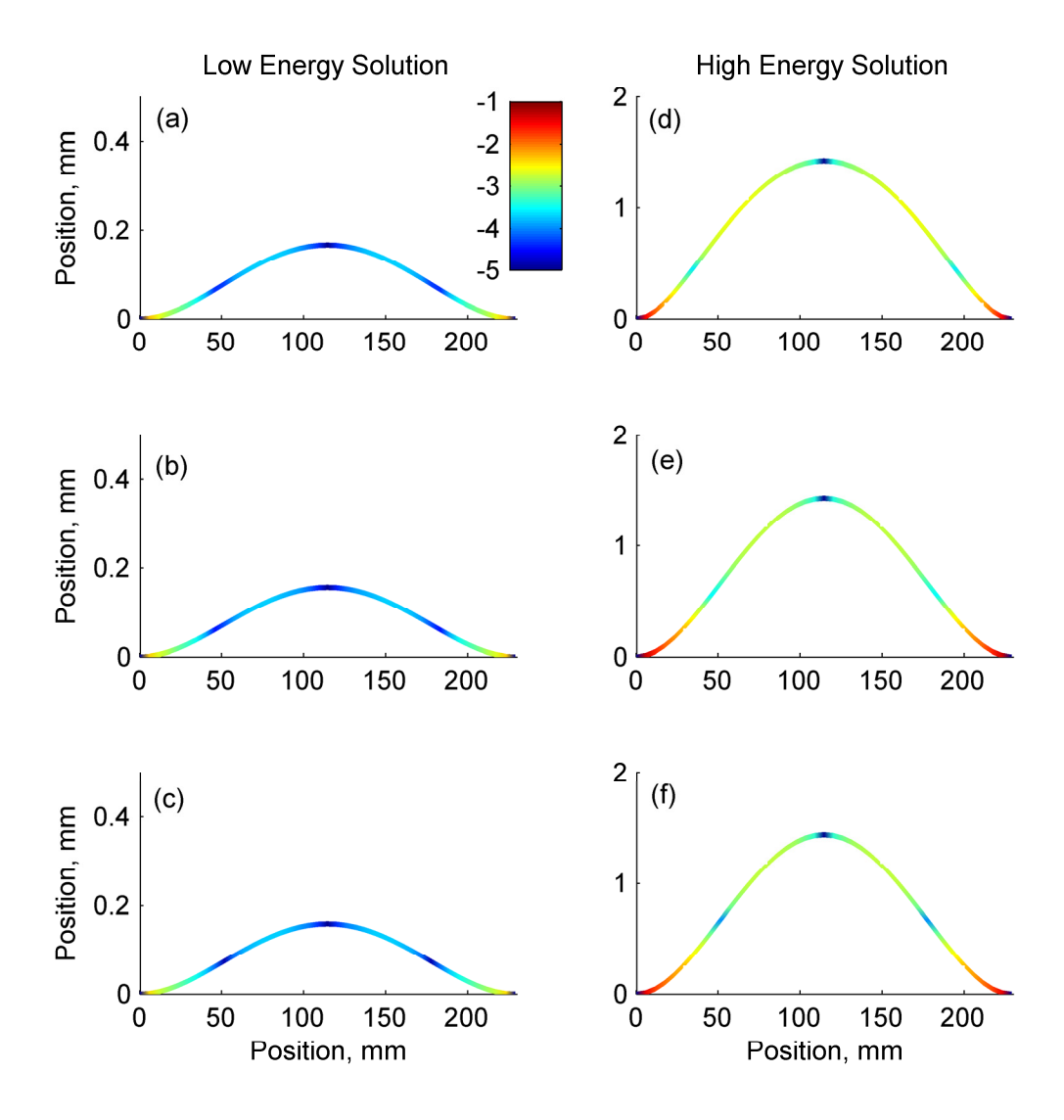


Figure 15. Deformation shapes of NNM 1 in Fig. 14 at low (left column) and high (right column) energy computed using the (a, d) AMF method, (b, e) ICE (1) CLD (0.5), and (c, f) ED (1 26 39) CD (3.0 0.01 x2). The color bar gives the log of the ratio of in-plane displacement to transverse displacement at each node.

At low energy (left column), the deformation shapes were all dominated by the first linear bending mode shape of the beam, with little membrane stretching near the clamped ends. This was expected since the NNM converges to the linearized mode of the system at low energy, and the amplitude of the bending motion was not large enough to induce much bending-membrane coupling. The solution at high energy (right column), near 130 Hz on the FEP,

showed significant contribution of geometric nonlinearity in the response. Each of the deformations in Fig. 15 (right column) show that the bending-membrane coupling was much more significant than the lower energy solution. The NLROMs predicted the deformation reasonably well at high energy, but looking closely one can see that they both differ slightly from the full order model (top row); the AMF solution appears to "flatten" near the midpoint, suggesting that the third bending mode was beginning to contribute to the NNM. Also, the color bar shows that the axial deformation predicted by ED (bottom row) and ICE (middle row) does not exactly agree with that obtained with AMF; the node points in the axial displacement occur about 2 cm closer to the clamped ends in the AMF result. These discrepancies perhaps explain the differences between the FEPs at higher energy in Fig. 14. The lack of higher order bending kinematics also explains why neither of these models captured the "tongues" that emanated from the FEPs in the AMF solution. These deviations are known as internal resonances, or modal interactions, and occur when two or more NNMs interact with one another.

A few NLROMs were generated with larger and smaller scaling factors in order to demonstrate the inaccuracy of the reduced equations when the proper scaling amplitude was not chosen for the static load cases. The FEP of the first NNM in Fig. 16 shows results from ICE ROMs with CLD having a  $w_{\text{max},1}$  value was set to a displacement of 0.001 and 30.0 times the beam thickness, and ED ROMs with CD scaling factors where the first bending mode displaced with  $w_{\text{max},1}$  of 0.5 and 100.0 times the thickness. These scale factors were chosen to illustrate how sensitive/insensitive the methods can be in various cases. Due to the hardening nature of the NNM, the  $A_1(1,1,1)$  stiffness term dictates the "bend" of the NNM curve, so the different scaling amplitudes strongly affect the fit of this value.

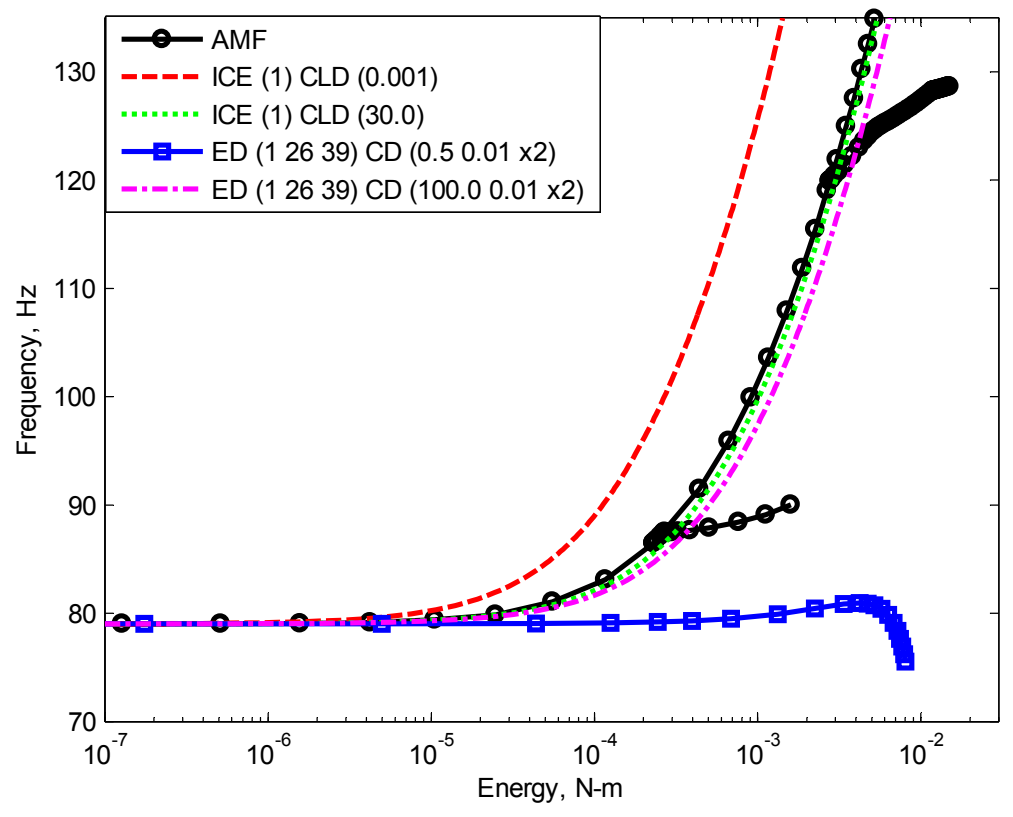


Figure 16. Frequency-energy plot of NNM 1 of the clamped-clamped beam model with various NLROM strategies.

The ICE NLROMs miscalculate the backbone of NNM 1 drastically when the force amplitude was not large enough to excite the nonlinearity (dashed red), and the NNM was only just beginning to diverge when the force was too large (short dashed green). Using the ED approach, applying a displacement that is only marginally less than the beam thickness (blue squares) clearly misses the behavior of the full order model, and even predicts softening behavior around 0.006 N-m! On the other hand, even when the first mode is displaced far more than is optimal, the ED NLROM (dashed dot magenta) produces a backbone that diverges a little from the AMF solution. The NNMs are clearly sensitive to the scaling, and hence one can use an analysis like this for each bending mode in the basis set to determine the range of scaling factors that seem to give the most consistent or reasonable results. In the next subsection, additional

modes are added to the basis and similar studies were done to select the optimal scaling values for the appropriate bending and axial modes used in either ROM estimation procedure. Those results show that the multi-mode ROMs are even more sensitive to the scaling.

#### 4.2.2 Multi-Mode NLROMs

Additional bending modes were included in the basis set in hopes of improving the accuracy of the NLROMs, allowing them to capture the modal interactions with higher order NNMs. The tongue at 88 Hz in the FEP in Fig. 14 (AMF, dotted black) was a 5:1 internal resonance, representing an interaction between the 1<sup>st</sup> and 3<sup>rd</sup> NNMs. For each solution along the tongue, the 3<sup>rd</sup> mode oscillated at 5 times the frequency of the 1<sup>st</sup> mode. The natural frequency of the third linear bending mode is 427.5 Hz, which is not commensurate with the linear natural frequency of the first bending mode (79 Hz), but as the frequency of NNM 1 increased due to the bending-membrane coupling, the integer ratio between the two frequencies became commensurate resulting in a modal interaction. The second internal resonance, near 120 Hz, started as a 4:1 interaction with the third bending mode. As energy increased, the fifth bending mode began to oscillate at a 9:1 ratio, simultaneously as the third mode vibrated at a 4:1 ratio. At even higher energy, the seventh mode began to contribute at a 16:1 ratio, along with the previous interactions.

In order to capture this behavior with the NLROMs, all of the modes/kinematics involved in the interaction must be included in the basis set. The ED procedure was used with additional bending and axial modes. Based on the results in Table 3, bending modes 3, 5, and 7 were added due to the nonlinear coupling to the first bending mode. For each higher frequency bending mode, two of the dominant anti-symmetric axial modes coupled to that bending mode were also added to the basis. The first NNM, computed from multi-mode ED NLROMs using various

mode combinations and scaling methods, is shown in Fig. 17. The axial modes were again displaced at a much lower fraction of the beam thickness (0.01 times the thickness) with the CD scaling method.

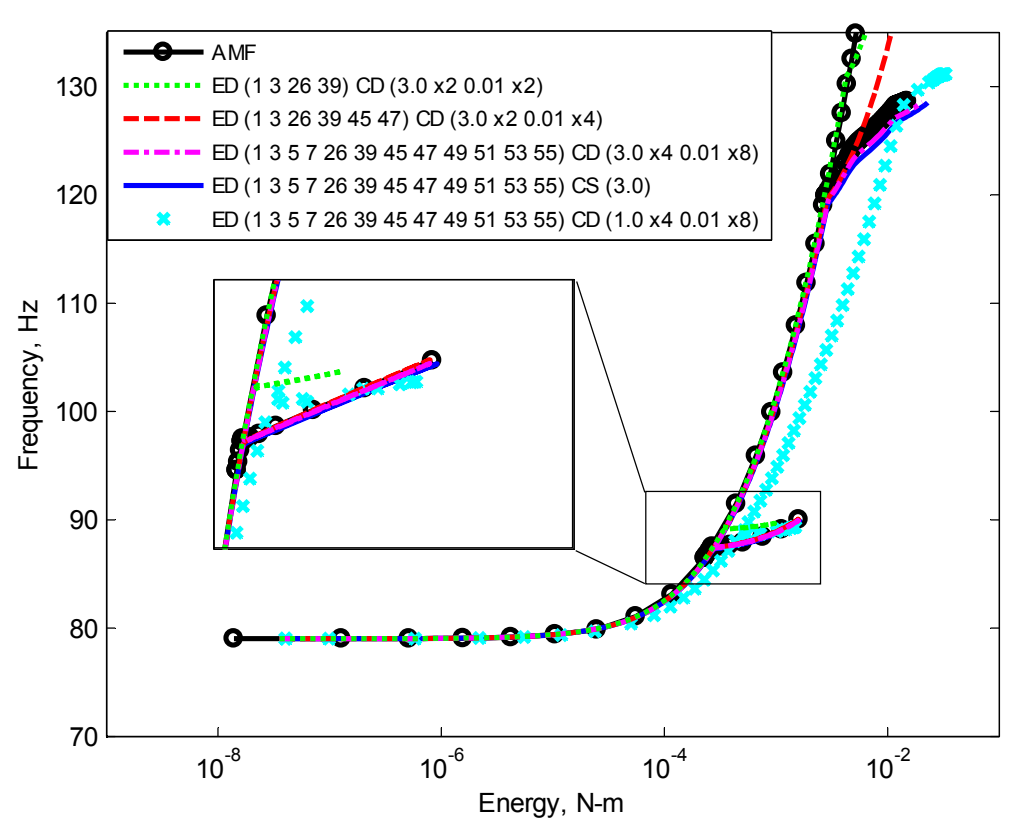


Figure 17. Frequency-energy plot of NNM 1 of the clamped-clamped beam model with ED NLROM strategy with higher frequency bending and axial modes.

The results presented here illustrate several issues that were discovered and which must be addressed to obtain an accurate estimate of the NNM. First consider the ED (1 3 26 39) ROM shown in dashed green. At very high energies this ROM estimated the NNM backbone more accurately than the ED (1 26 39) ROM in Fig. 14, confirming the importance of the third bending mode at these energies. However, this NLROM still did not capture the internal resonance near 88 Hz where linear modes 1 and 3 interact. By simply adding the two antisymmetric axial modes that were most strongly coupled to the third bending mode (modes 45

and 47), the NLROM (dashed red) accurately computed its interaction with the third NNM near 88 Hz. The additional axial modes, which coupled to the third bending mode, helped soften the third NNM (see Fig. 19), which influenced the modal interaction on the first NNM branch. Note that trial and error revealed that two axial modes were needed for each bending mode for this problem. NLROMs were also created including only one anti-symmetric axial mode per bending mode and they did not compare as well with the AMF solution.

As expected, neither of the ROMs discussed thus far (the ED (1 3 26 39) and ED (1 3 26 39 45 47) NLROMs) accurately captured the second internal resonance near 120 Hz, since it involved bending modes 5 and 7, which were not included in these bases. By adding these modes (5 and 7) with the appropriate axial modes (49, 51, 53, 55) and using the CD scaling method, the obtained result (dashed dot magenta) had nearly converged to the true NNM by capturing the second internal resonance near 120 Hz. This illustrates the importance of including an adequate number of bending modes in the basis set, and augmenting these with the appropriate axial modes.

Two other cases are also presented to illustrate the effect of scaling. A 12-mode ED NLROM was created with the CS scaling, ED (1 3 5 7 26 39 45 47 49 51 53 55) CS (3.0) (solid blue), and found to agree very well with the result when CD scaling was used, ED (1 3 5 7 26 39 45 47 49 51 53 55) CD (3.0×4 0.01×8) (dashed dot magenta). Even though the CS method worked well here, one objection to this approach was that it automatically assigned the scaling amplitude to the other modes in the basis. These automatically assigned values could potentially cause higher order modes to be displaced too little, causing the nonlinearity to not be excited and the nonlinear stiffness coefficients to be poorly fit. The cyan x's in Fig. 17 shows an example of this using an identical 12-mode basis with the CD method, but where the bending modes were

displaced 1.0 times the beam thickness rather than three times. This NLROM did not accurately represent the backbone of NNM 1, nor the internal resonances. It appears that the bending modes were not displaced enough in this case to adequately excite the nonlinearity, and as a result the NLROM coefficients were not accurately estimated. This shows that the scaling for the static displacements must be carefully selected in order to generate an accurate NLROM.

Next, the convergence of the ICE method was evaluated as bending modes were added to the basis set using the CLD scaling method for the static loads to fit the nonlinear stiffness coefficients. The FEPs of NNM 1 in Fig. 18 were computed from NLROMs with modes 1, 3, modes 1, 3, 5, 7 and modes 1, 3, 5, 7, 9, 11. (Recall that the axial modes do not need to be included in the basis set when using the ICE method.) Each bending mode used a CLD factor of 0.5 times the thickness, except for mode 11 which used a value of 0.1 time the thickness. These values were selected in order to keep the nonlinear to linear displacement ratio  $\gamma_r$  near 0.9.

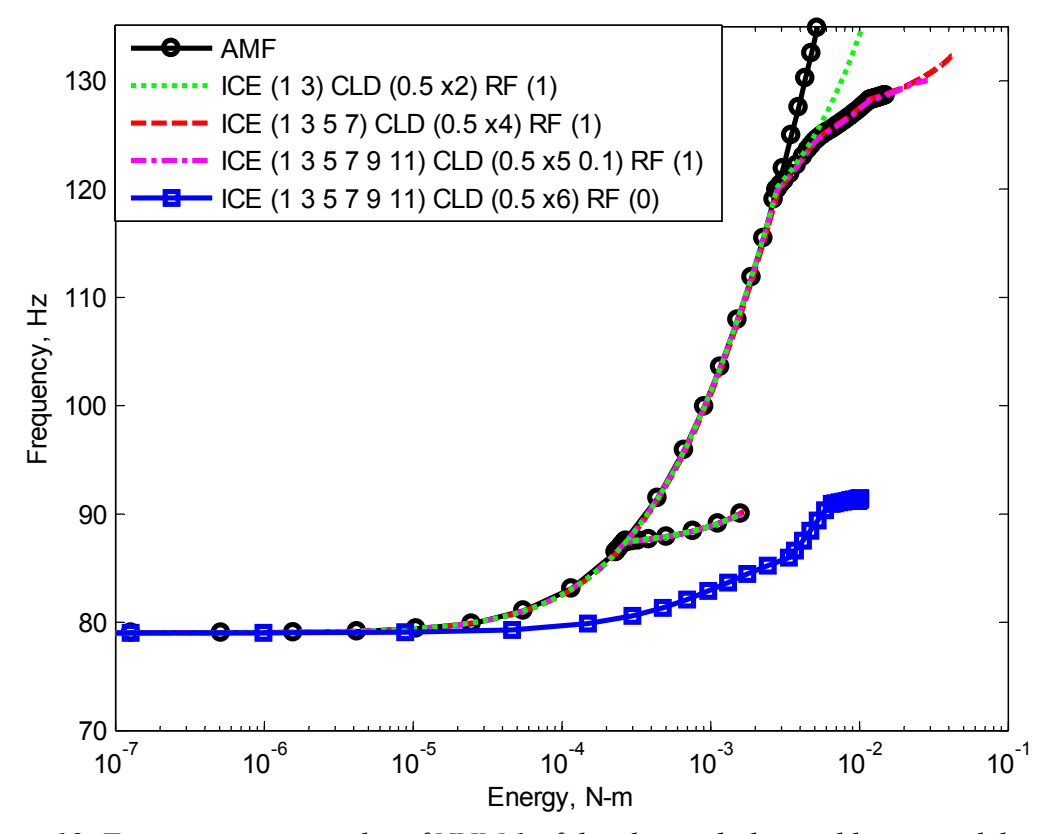


Figure 18. Frequency-energy plot of NNM 1 of the clamped-clamped beam model with ICE NLROM strategy using higher frequency bending modes.

The NNMs for the ICE method with CLD scaling revealed that NNM 1 converged quickly along the main backbone, and the two-mode NLROM (short dashed green) captured the first internal resonance near 88 Hz as soon as the third bending mode was added. The first NNM converged on the second internal resonance near 120 Hz as modes 5 and 7 were added to the basis. Overall, the NLROMs agreed with the AMF solution of NNM 1 when the ICE model used CLD scaling factors and the RF method was used to keep the loads small when forces were applied in the shape of several modes simultaneously (e.g. RF (1) in the legend means that this feature was used).

The 6-mode NLROM with the RF method (dashed dot magenta) produced an NNM that agreed very well with the AMF results, even along the second internal resonance. The ICE

method showed considerable sensitivity to the scaling amplitudes when not using the reduction factor, RF (0), as illustrated by the last line in Fig. 18. This model used a 6-mode basis (modes 1, 3, 5, 7, 9, 11) with a CLD factor of 0.5 times the thickness for mode 11 and no reduction factor (blue squares). Experience has shown that the RF was more robust and produced more consistent results as the NNMs seemed to be less sensitive to amplitude of the scale factors.

The next two higher frequency NNMs were computed with the ICE and ED NLROMs and compared to the results with the AMF algorithm, and are shown in Fig. 19. Each NLROM was capable of computing the NNM, which is an extension of the linear mode at low energy, as long as that mode was included in the basis set. NNMs 3 and 5 computed with the two NLROMs in Fig. 19 agree very well with the AMF solution along the backbone, in fact they practically overlay each other in the FEP. A small discrepancy existed between the ED NLROM (dashed red) and AMF (black circles) at the internal resonance near 680 Hz in NNM 3. This was a 5:1 modal interaction with the NNM 9, and since the ED NLROM did not include the ninth bending mode it was unable to capture this internal resonance (otherwise the two ROMs gave almost indistinguishable results).

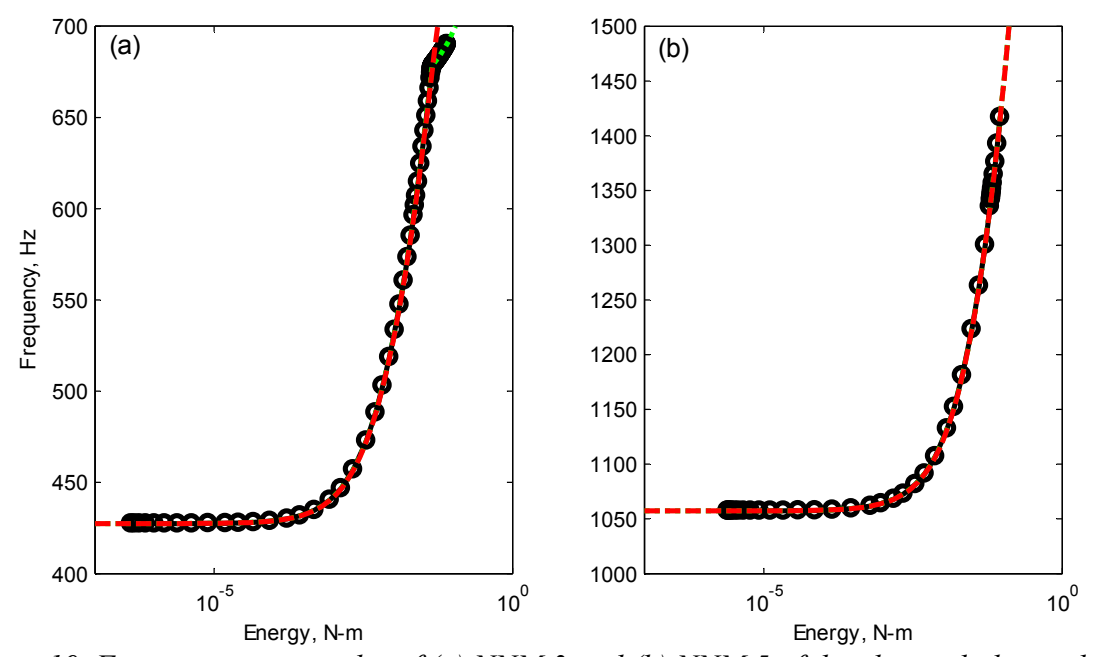


Figure 19. Frequency-energy plot of (a) NNM 3 and (b) NNM 5 of the clamped-clamped beam model with (black circles) the AMF algorithm, (short dashed green) ICE (1 3 5 7 9 11) CLD (0.5 ×5 0.1) RF (1) and (dashed red) ED (1 3 5 7 26 39 45 47 49 51 53 55) CD (3.0 ×4 0.01 ×8).

## 4.3 Application to Exhaust Cover Panel with Geometric Nonlinearity

The NLROMs were used to compute the first NNM of a larger, more realistic FEA model of an exhaust cover plate that exhibited geometric nonlinearity during laboratory tests. The model reduction strategy becomes even more appealing for this system since it has many more degrees of freedom than the beam studied in Section 4.2. The mesh for this model is shown in Fig. 20. The plate was 12.5 inches (318 mm) in diameter, and was constructed of structural steel with a mass density of 7.29·10<sup>-4</sup> lb-s<sup>2</sup>/in<sup>4</sup> (7,800 kg/m<sup>3</sup>) and a Young's modulus of 30,160 ksi (208 GPa). The plate was modeled in Abaqus® with 899 S8R shell elements, with a uniform thickness of 0.0059 inches (1.5 mm), resulting in a total of 15,708 DOF. Each DOF along the bottom ring of the plate was fixed in all translations and rotations, modeling the relatively rigid boundary to which the plate was welded.

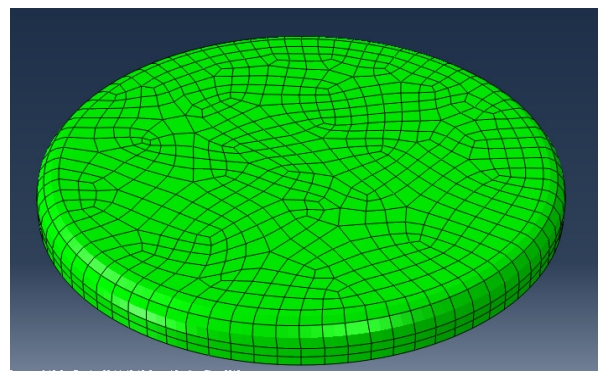


Figure 20. Finite element model of a geometrically nonlinear exhaust cover plate.

A static force was applied to the FEA model that would have displaced the first linear mode to a maximum displacement of 0.059 inches (1.5 mm), or 1 times the plate thickness. The computed deformation revealed static coupling to higher frequency modes, which are shown in Table 4 in descending order of relative modal amplitude. The first five of these linear mode shapes are plotted in Fig. 21, and serve as candidate modes to successively include in the NLROM basis. Note that no purely axial or membrane modes appeared to be coupled to the first bending mode, although mode 156 is predominantly axial. Similar studies of curved beams and curved panels have shown that axial modes often cease to be distinct from the bending modes when there is curvature in the structure [114-116].

Table 4. Relative modal amplitude due to a static force applied to excite the first linear mode of the exhaust plate, and the corresponding linear natural frequency.

Mode #	1	6	156	15	30	175	51	74
Amp	1.00	$6.8 \cdot 10^{-3}$	$4.0 \cdot 10^{-3}$	$2.4 \cdot 10^{-3}$	$1.5 \cdot 10^{-3}$	$1.5 \cdot 10^{-3}$	$9.5 \cdot 10^{-4}$	$5.6 \cdot 10^{-4}$
Frequency,	156.4	607.5	10,770	1,358	2,402	11,650	3,731	5,328
Hz								

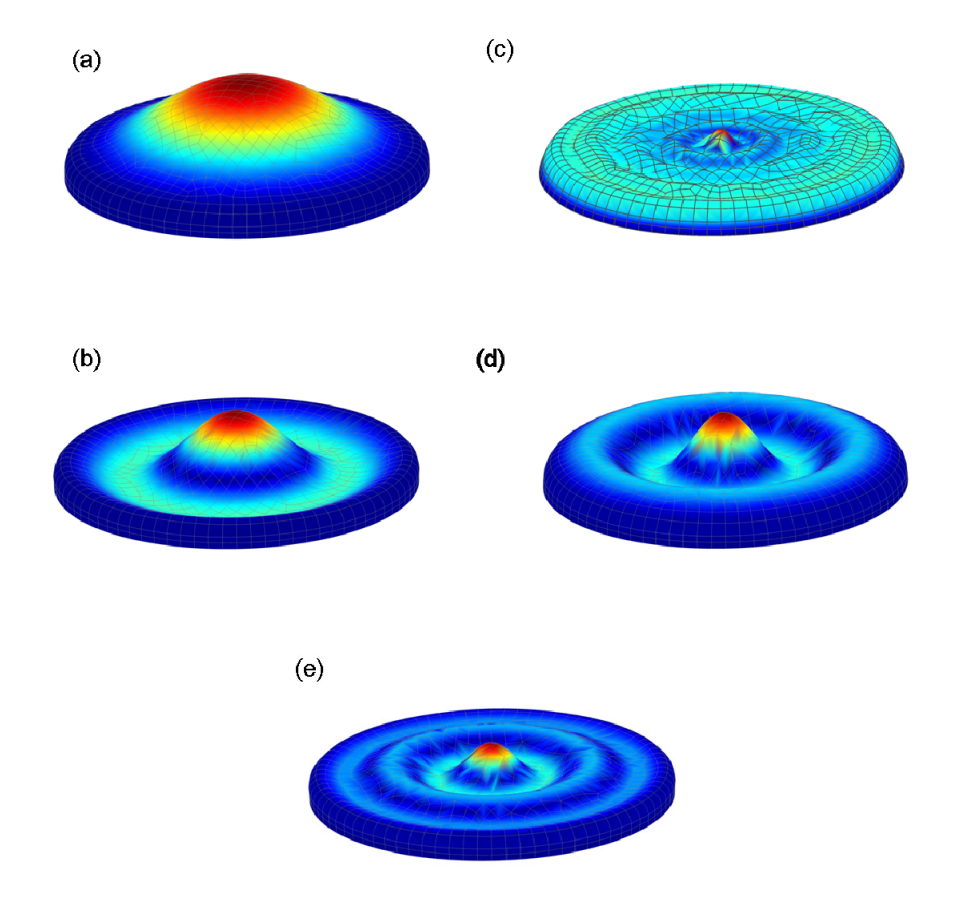


Figure 21. Linear mode shapes of exhaust cover plate model for (a) mode 1, (b) mode 6, (c) mode 156, (d) mode 15, and (e) mode 30.

The ICE and ED strategies were used to generate NLROMs of the FEA model in order to compute and compare the first NNM to the true NNM computed with the AMF algorithm in Chapter 2. Based on the best practices observed for the beam studied in the previous section, the CD scaling approach with  $w_{\text{max},r}$  set to 3 times the thickness was used with the ED method to produce the NNMs shown in Fig. 22. The CLD scaling with the RF was used with the ICE method and those results are shown in Fig. 23. The CLD scaling factors with ICE used a scaling value with  $w_{\text{max},1}$  equal to 0.059 inches (1.5 mm), or 1 times the plate thickness, and was found to be reasonable for the first bending mode since the plate's curved edges make this structure's

boundary more compliant than the clamped beam's. Higher frequency modes used a lower fraction of the thickness in order to keep the nonlinear to linear displacement ratio  $\gamma_r$  near 0.9.

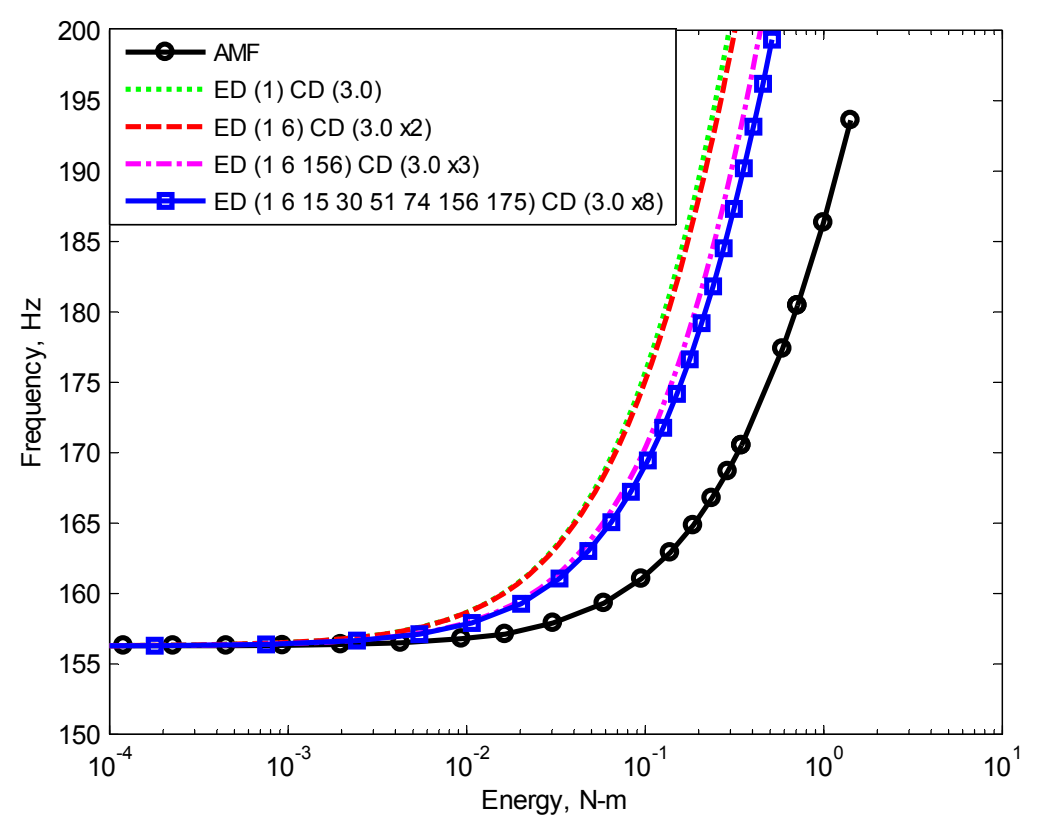


Figure 22. Frequency-energy plot of NNM 1 of the exhaust cover plate model with ED NLROM strategy using higher frequency bending modes.

The ED method did not perform as well for this system as it did for the beam. A single-mode NLROM was greatly in error, yet results for the first NNM improved somewhat as additional modes were added to the ED basis. Even after including the eight modes that were most strongly coupled to the first bending mode, as shown in Table 4, the FEP was off by nearly an order of magnitude in energy at 190 Hz. The FEA model of the clamped-clamped beam showed that including axial type modes greatly improved the accuracy of the ED NLROM. However, no pure membrane modes existed for the exhaust cover plate due to its slight curvature, so this remedy was not available.

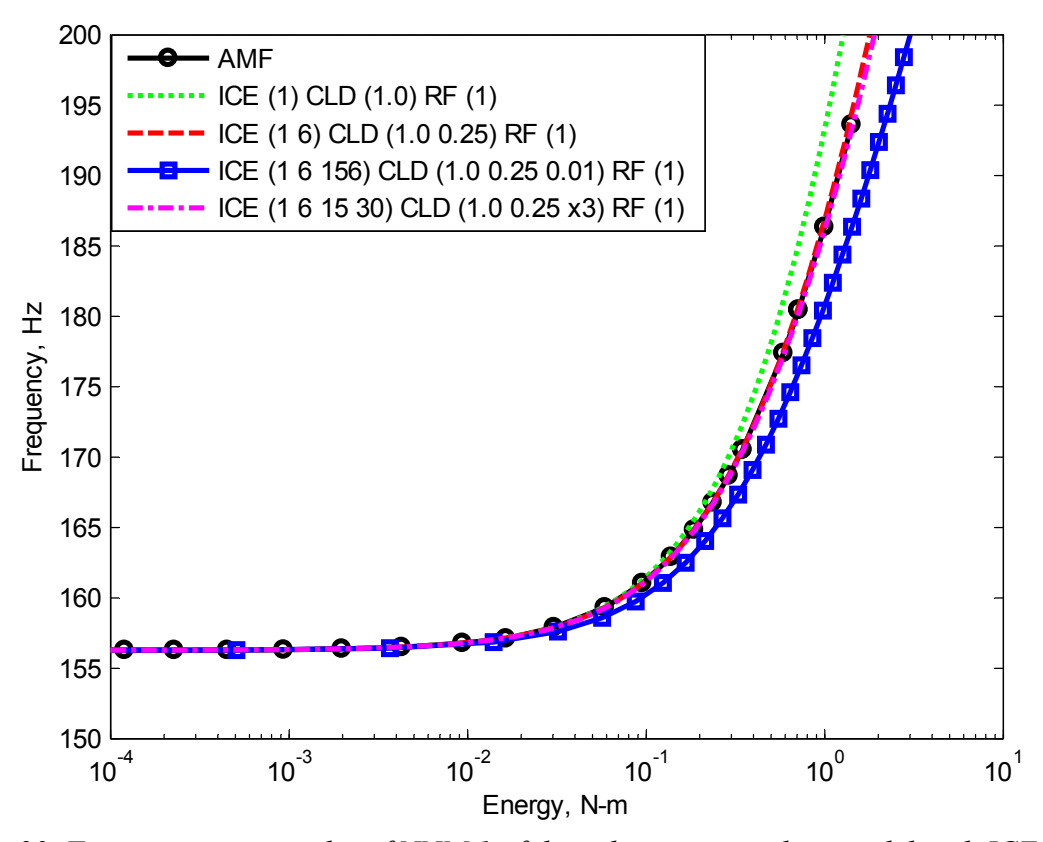


Figure 23. Frequency-energy plot of NNM 1 of the exhaust cover plate model with ICE NLROM strategy using higher frequency bending modes.

The NNM estimated by a one-mode NLROM (short dashed green) constructed using the ICE method was only slightly in error at higher energies, and the NLROM quickly converged to the true NNM when mode 6 was added to the basis (dashed red). The sixth bending mode had a strong coupling to the first NNM, and hence it is not surprising that this mode had an important dynamic effect. Using this NLROM, the first NNM could be computed much more efficiently than the AMF algorithm on the full order model; only about 15 minutes were needed to solve the nonlinear static load cases to create the two-mode NLROM and compute the first NNM branch. In contrast, running the AMF algorithm on the full model took approximately 4 days.

Two other cases are also shown in Fig. 23 to illustrate a potential pitfall of the ICE strategy. When the next dominant mode, mode 156, was added to the ICE basis set (blue

squares), the first NNM diverged. The FEA model had difficulty converging in the static load cases used to create the NLROM with mode 156. By using a small enough CLD factor with  $w_{\rm max,156}$  equal to 0.01 times the plate thickness, the static results finally converged resulting in a nonlinear to linear ratio of  $\gamma_{156}=0.98$ . It was decided that mode 156 should be removed from the basis set, and the next two modes (15 and 30) included instead, producing the result shown with the dashed dot magenta line. The resulting four-mode NLROM again predicted the first NNM very accurately. This example highlights the importance of mode selection with the reduced order modeling strategy. The fact that mode 156 had a much higher frequency leads one to believe that this mode only needs to be included implicitly, and should not be included explicitly in the basis set. Based on these results, the ICE method seemed to be better suited for systems with many DOF, as long as the modes are scaled appropriately and the correct modes are added to the basis.

# 4.4 Simply Supported Beam with Contacting Nonlinearity

The reduced order models of the beam in Fig. 24 are generated using a Galerkin approach with linear vibrations modes augmented with discontinuous basis functions, as done in [40, 113]. The linear, simply supported beam is modeled in Abaqus® using 40 B31 beam elements, resulting in a total of 119 DOF. The contact is modeled as a linear spring with a unilateral piecewise-linear function at a distance  $l_1$  from the left support, with a spring stiffness of k and clearance a. When the spring is engaged, it applies a force on the beam in the transverse direction, resulting in a non-smooth, nonlinear system of equations. The spring in this example is located at the midpoint of the beam with  $l_1 = 4.5$  inches (114 mm) and a clearance of a = 0.0155

inches (0.394 mm). The material and geometric properties of the beam in Fig. 24 are given in Table 5.

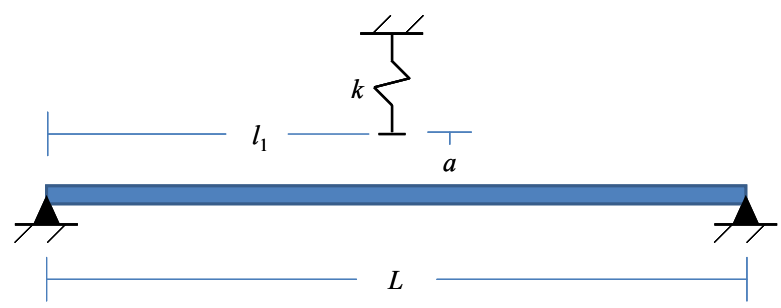


Figure 24. Schematic of simply supported beam with discrete contact nonlinearity.

Property	Value				
Young's Modulus	29,700 ksi (204.8 GPa)				
Poisson's Ratio	0.28				
Shear Modulus	11,600 ksi (80.0 GPa)				
	$7.36 \cdot 10^{-4} \text{ lb-s}^2/\text{in}^4 (7,870 \text{ kg/m}^3)$				
Density					
Length	9 inches (229 mm)				
Width	0.5 inches (12.7 mm)				
Thickness	0.031 inches (0.787 mm)				
K <sub>eq</sub>	9.7 lbf/inch (1.70 kN/m)				
Spring Stiffness, k	200 lbf/inch (35.0 kN/m)				
Spring Clearance,					
а	0.0155 inches (0.394 mm)				
Spring Location,					
$l_1$	4.5 inches (114 mm)				

Prior to the nonlinear modal convergence analysis, the first seven linear modes of the beam were computed, and the corresponding natural frequencies are listed in Table 6. Each is a low frequency bending mode, where the even mode numbers are asymmetric shapes and the odd numbers are symmetric. Only the odd bending modes are used in the reduction scheme, since all of the even modes have nodal points at the impact location. Since the nonlinearity is localized to only a single DOF, only a single discontinuous basis vector was computed for each ROM, and

was orthonormalized with respect to the mass matrix. As a result, this augmented basis vector changed depending on which linear modes were included in the basis set.

Table 6. Linear natural frequencies of simply supported beam.

Mode 1	Mode 2	Mode 3	Mode 4	Mode 5	Mode 6	Mode 7
34.8 Hz	139.4 Hz	313.8 Hz	558.2 Hz	872.7 Hz	1258 Hz	1714 Hz

The NNMs from various ROMs are computed to study the convergence of the beam as modes are added to the basis set. In this study, ROMs with mode (1), modes (1 MC), modes (1 3 5 MC) and modes (1 3 5 7 9 11 MC) were generated using the approach described in [113]. The Milman-Chu (MC) mode is the added discontinuous basis vector used to improve the kinematic constraints at the location of the contacting spring, while the others are the mode numbers of the linear bending mode shapes computed from the linear mass and stiffness matrix. The first, third and fifth NNMs (all symmetric) were computed from these ROMs, and the resulting frequency-energy plots are presented in Figs. 25 to 28.

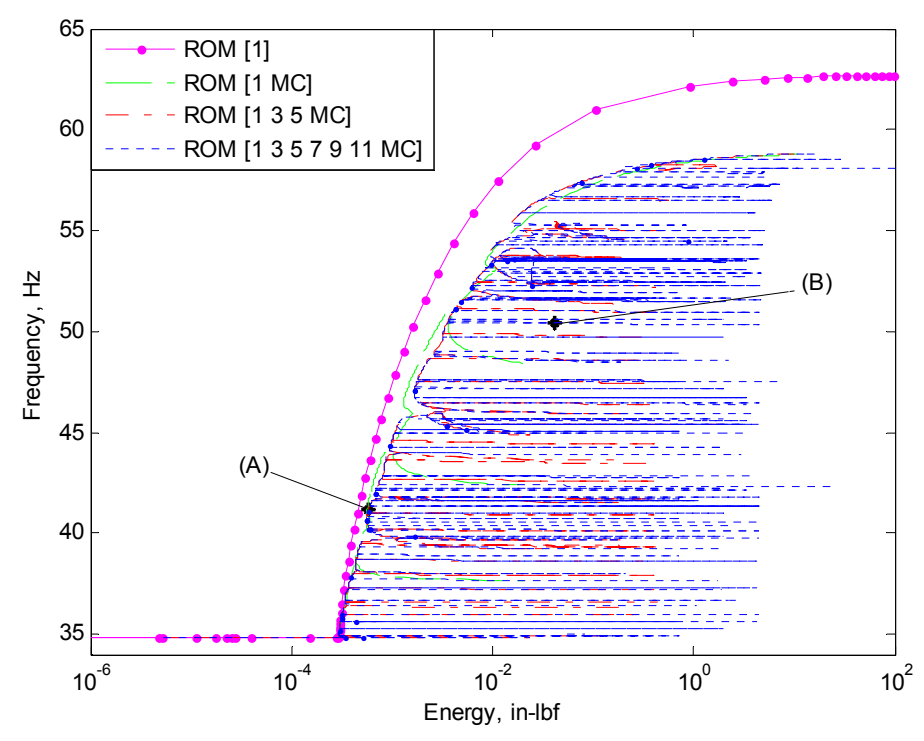


Figure 25. The first NNM computed for the (dotted magenta) ROM with mode (1), (dashed green) ROM with modes (1 MC), (dash-dot red) ROM with modes (1 3 5 MC), and (short dashed blue) ROM with modes (1 3 5 7 9 11 MC). Time response of solutions (A) and (B) are plotted in Fig. 26.

The first NNM was initiated at the first linear mode with a frequency of 34.8 Hz, and was computed out to a 69% shift in fundamental frequency (with the 7-mode ROM). At low energy, the response amplitude was low enough that the contacting spring did not engage with the beam, and the periodic response was exactly that of the first linear bending mode. The linear response range is seen by the straight line in the frequency-energy plane in Fig. 25 below  $3.0 \cdot 10^{-4}$  in-lbf. Once the midpoint amplitude of the first bending mode reached the spring clearance (a = 0.0155 inches), the engaged spring caused the NNM to change. The transition from linear to nonlinear occurred at an energy of  $3.0 \cdot 10^{-4}$  in-lbf, and the periodic responses stiffened (i.e. increased in frequency) due to the added stiffness of the contact.

Two features of the NNM branch are observed in this nonlinear range: the backbone and the modal interactions that emanate from the backbone (e.g. the sharp peaks with nearly constant frequency in the FEP). These deviations from the backbone occur when two or more modes interact, and exchange energy with other NNMs of the ROM. The plots in Fig. 26 show the time response of the two points marked (A) and (B) in Fig. 25 from the ROM with modes (1 3 5 7 9 11 MC). The response of solution (A) oscillates with a frequency of about 41.2 Hz predominantly in the shape of the first bending mode. Through one period of response, Figs. 26a and 26b show that this NNM solution contains higher order harmonics as well as contributions of higher order bending modes. Solution (B) reveals the periodic motion along one of its (many) internal resonances occurring at a frequency of about 50.4 Hz. This was a 34:1 interaction with the 7<sup>th</sup> mode, meaning that NNM 7 oscillated at a frequency 34 times the frequency of the first NNM. The deformation shapes in Fig. 26c show the complicated response through different snapshots of time with strong contributions from the 1<sup>st</sup> and 7<sup>th</sup> mode shapes.

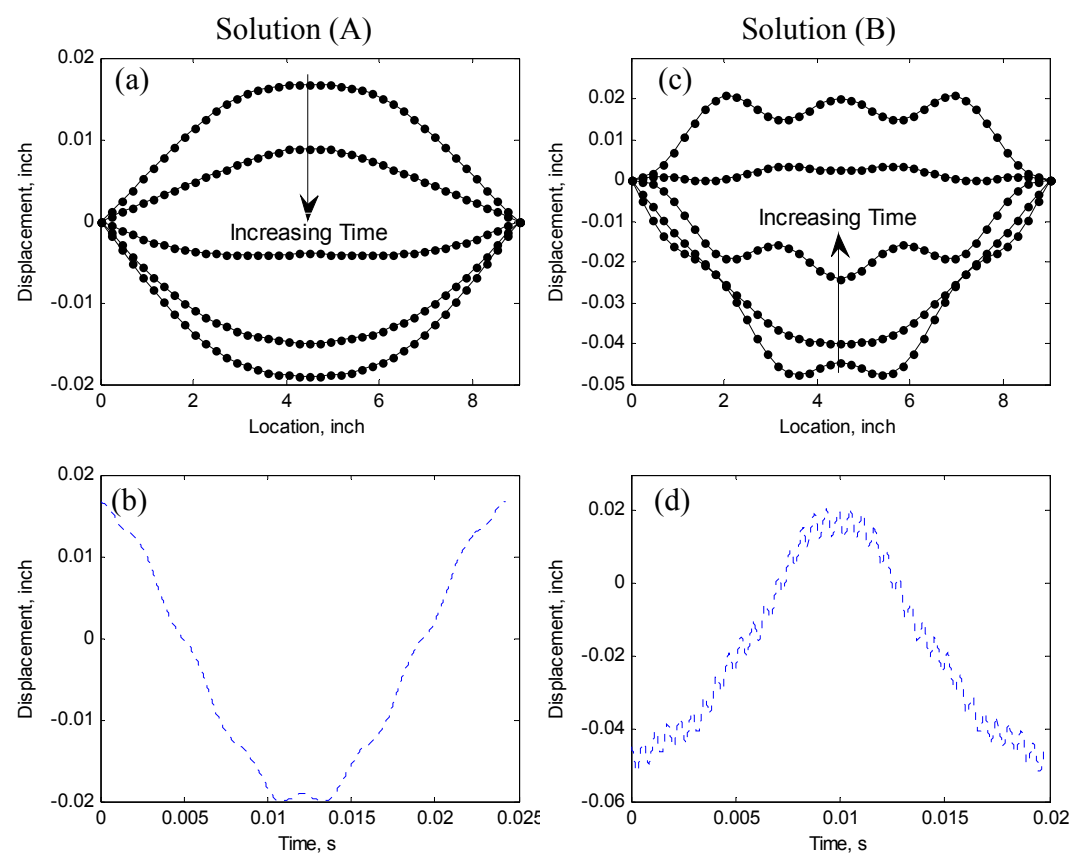


Figure 26. Time history of NNM solutions (A) and (B) in Fig. 25 for the ROM with modes (1 3 5 7 9 11 MC). Plots (a) and (c) show the beam deflection shape at different snapshots in time, and plots (b) and (d) show the time history of the contacting DOF over one period.

The first NNM in Fig. 25 from the ROM with mode (1) captured the linear solution at energies below 3.0·10<sup>-4</sup> in-lbf, but did not accurately capture the backbone in the nonlinear range. For example, at an energy level of 5.0 in-lbf, this ROM predicted a frequency of 62.5 Hz, whereas the other ROMs predicted 58.7 Hz (an error of 6.5%). The (1 MC) ROM captured the backbone quite accurately, revealing that the MC mode greatly improved the accuracy of the ROM. On the other hand, the ROM with modes (1 MC) only computed 3 internal resonances, which was significantly fewer than the amount captured with the higher fidelity ROMs. The contacting spring was coupling higher order modes into the response, so several additional modes were needed in the basis set to accurately capture these internal resonances. The backbone

appears to be converged to high precision with the (1 3 5 MC) and (1 3 5 7 9 11 MC) mode ROMs. However, the internal resonances of these ROMs have not yet converged, as the 7-mode ROM still introduced many new tongues along the backbone and few, if any, agree with those of the 4-mode ROM. This comparison revealed that a relatively simple ROM can accurately capture the backbone of NNM 1, but tremendously more effort would be needed if internal resonances were to also converge.

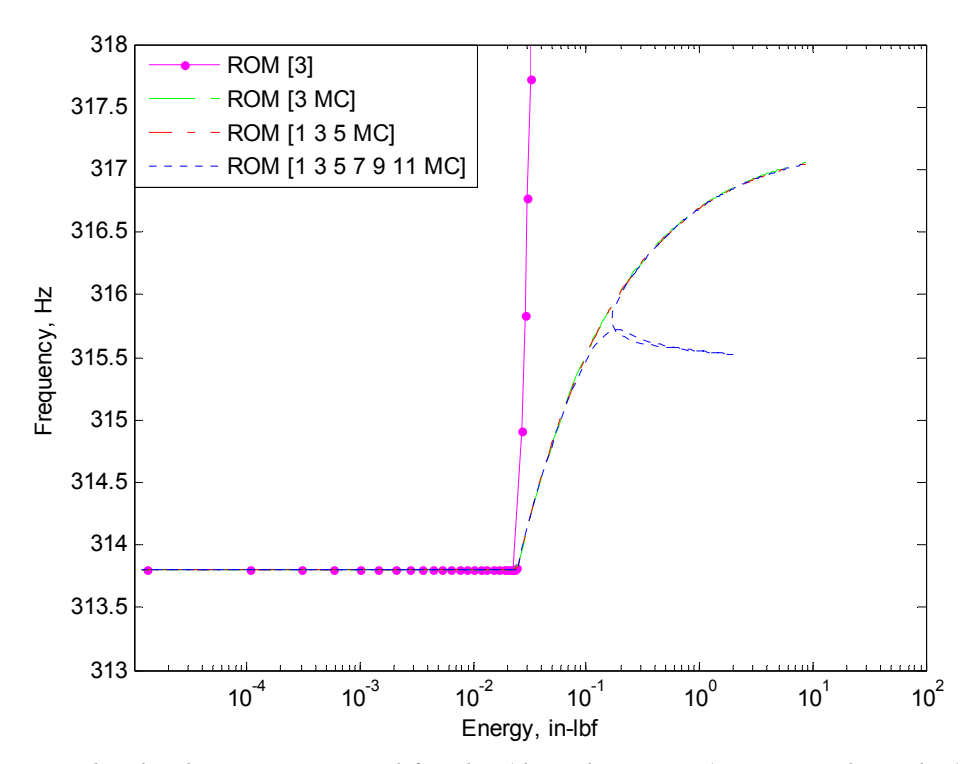


Figure 27. The third NNM computed for the (dotted magenta) ROM with mode (1), (dashed green) ROM with modes (1 MC), (dash-dot red) ROM with modes (1 3 5 MC), and (short dashed blue) ROM with modes (1 3 5 7 9 11 MC).

The FEP of the third NNM is plotted in Fig. 27 for ROMs generated with mode (3), modes (3 MC), modes (1 3 5 MC), and modes (1 3 5 7 9 11 MC). The third NNM has the same features as the first NNM in Fig. 25, but is much simpler since only one internal resonance appears at 315.8 Hz. The nonlinear region of the third NNM started at an energy of  $2.4 \cdot 10^{-4}$  inlbf, and below this level the beam oscillated in exactly the third bending mode with a frequency

of 313.8 Hz. Above 2.4·10<sup>-4</sup> in-lbf, the spring was engaged and caused the fundamental frequency of the motion to increase. The third NNM had a frequency shift of about 1.0 %, which was significantly less than that of the first NNM. Again, the ROM computed with mode (3) did not accurately capture the backbone, and the one-mode model was far too stiff. The accuracy of this ROM improved greatly when one discontinuous basis vector was added to the basis, however additional bending modes did not significantly change the backbone. As the model order increased, there was an internal resonance that occurred at 315.8 Hz, which was only computed with the ROM with modes (1 3 5 7 9 11 MC). It was discovered that this internal resonance was a 9:1 interaction with the 9<sup>th</sup> NNM of the beam, and hence could not be captured unless the kinematics of the 9<sup>th</sup> bending mode were included in the basis. Other internal resonances may also be captured with additional bending modes, but this was not pursued further.

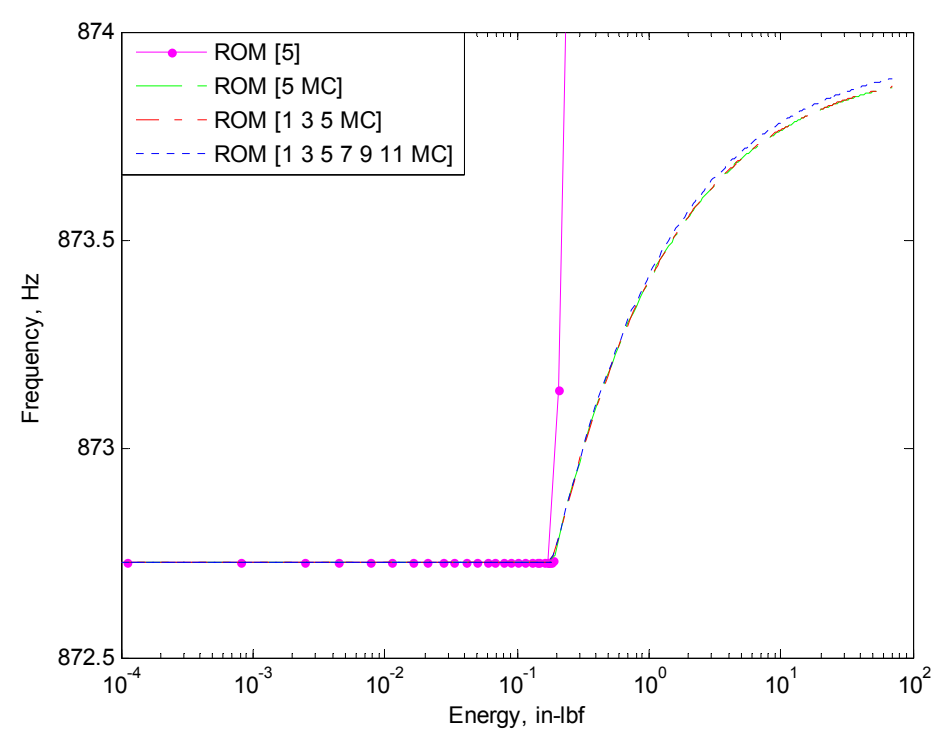


Figure 28. The fifth NNM computed for the (dotted magenta) ROM with mode (1), (dashed green) ROM with modes (1 MC), (dash-dot red) ROM with modes (1 3 5 MC), and (short dashed blue) ROM with modes (1 3 5 7 9 11 MC).

The nonlinear range of the fifth and final NNM in Fig. 28 began at an energy level of 0.19 in-lbf, and had a total frequency shift of only 0.1% with the highest fidelity ROM. None of the ROMs predicted a modal interaction with the fifth NNM over this frequency/energy range. The ROM with only mode (5) appeared to be very stiff compared to the higher fidelity ROMs, consistent with the behavior observed with the other NNMs. There was practically no difference between the backbone of the ROMs with modes (5 MC) and (1 3 5 MC), but the ROM with modes (1 3 5 7 9 11 MC) caused the backbone to shift slightly to higher frequency. In order to determine whether this backbone had converged, additional modes would need to be added to the basis.

The comparisons presented so far reveal that in some cases adding modes to the basis introduced new dynamics to the system, such as an additional internal resonances, while in other

cases they simply improved the accuracy of the backbone (e.g. when the model was augmented from (1) to (1 MC)). In the results shown here, the backbones of the first and third NNM appear to converge with the 7-mode ROM, but the internal resonances have not yet converged. Due to the complexity of the internal resonances, and the potentially infinite number of these solutions, the question remains: how important are these to the accuracy of the ROMs for other predictive purposes (e.g. solutions to a forced response)? Do these internal resonances manifest themselves in the response?

This question was addressed to a certain extent in a paper by Ardeh & Allen [42] where the response of a 2DOF nonlinear system was studied in detail, revealing that many other NNM branches exist with much lower fundamental frequencies than those extending from the linear modes. These solutions form manifolds in the state space that are tangent to the fundamental NNM manifolds, hence a response on one manifold can easily travel onto (or along) another. This, and the erratic convergence of the first NNM presented above, suggests that the transient response of this system may be quite difficult to predict with great precision. In the following subsection the transient response is presented for a few different load amplitudes in order to explore the correlation between the accuracy of the transient response computed by each ROM and their convergence of the underlying NNMs.

# **4.4.1 Impulse Loading Validation**

The first load considered was an impulsive load modeled by a half-sine pulse in time. Spatially, the impulse was given the *shape of the first linear bending mode*, such that  $\mathbf{f}(t) = \mathbf{M}\mathbf{\phi}_1 A \cdot g(t)$ , where g(t) is a half-sine pulse over a short time duration with a prescribed amplitude A. This load was chosen to excite the beam near its first NNM branch, where the

characteristics of the first NNM should be most strongly manifest. The half-sine pulse was applied to the beam for a duration of 1 ms, with various peak amplitudes A to excite the nonlinear beam to different (conserved) energy levels. All initial conditions were set to zero. The response was integrated over 1.0 second with  $10^7$  time steps using an implicit HHT  $\alpha$  method described in [4], with  $\alpha = 0$  such that no numerical damping was added to the response. No structural damping was added to the equations of motion either. The undamped case was chosen since it is likely the worst possible scenario since error to small differences will grow in time, whereas damping would cause these differences to dissipate, and would likely remove the effects of the modal interactions in the underlying undamped NNM.

The root mean square (RMS) value of the midpoint displacement over 1.0 second of undamped response was calculated from the response predicted by each ROM and the full order model with no reduction to assess the suitability of the ROMs for failure prediction. The maximum midpoint displacement was also noted, as this metric might be of interest if brittle failure were expected due to a blast, while the RMS might be used to assess the fatigue damage incurred by the load. The results for different load amplitudes, A, and hence system energy levels, are compared in Tables 7 and 8.

Table 7. RMS value of midpoint displacement for various levels of excitation to a half-sine pulse in the shape of the first linear bending mode.

Load Case	<b>ROM</b> (1)	ROM (1 MC)	ROM (1 3 5 MC)	ROM (1 3 5 7 9 11 MC)	Full
$E = 1.8 \cdot 10^{-4} \text{ in-lbf}$	8.61·10 <sup>-3</sup> in				
$E = 2.0 \cdot 10^{-3} \text{ in-lbf}$	2.54·10 <sup>-2</sup> in	2.49·10 <sup>-2</sup> in	1.61·10 <sup>-2</sup> in	1.51·10 <sup>-2</sup> in	1.50·10 <sup>-2</sup> in
$E = 5.0 \cdot 10^{-2} \text{ in-lbf}$	0.133 in	0.129 in	0.0711 in	0.0699 in	0.0688 in
E = 0.76  in-lbf	0.525 in	0.507 in	0.421 in	0.414 in	0.414 in

Table 8. Maximum value of midpoint displacement for various levels of excitation to a half-sine pulse in the shape of the first linear bending mode.

Load Case	<b>ROM</b> (1)	ROM (1 MC)	ROM (1 3 5 MC)	ROM (1 3 5 7 9 11 MC)	Full
$E = 1.8 \cdot 10^{-4} \text{ in-lbf}$	1.21·10 <sup>-2</sup> in				
$E = 2.0 \cdot 10^{-3} \text{ in-lbf}$	4.05·10 <sup>-2</sup> in	4.05·10 <sup>-2</sup> in	3.84·10 <sup>-2</sup> in	3.92·10 <sup>-2</sup> in	3.92·10 <sup>-2</sup> in
$E = 5.0 \cdot 10^{-2} \text{ in-lbf}$	2.03·10 <sup>-1</sup> in	2.04·10 <sup>-1</sup> in	1.94·10 <sup>-1</sup> in	1.88·10 <sup>-1</sup> in	1.85·10 <sup>-1</sup> in
E = 0.76 in-lbf	0.786 in	0.792 in	0.778 in	0.762 in	0.762 in

For the predicted response at low energy ( $E = 1.8 \cdot 10^{-4}$  in-lbf), the maximum displacement in Table 8 for each model was 0.0121 inches, which was below the contact clearance of a = 0.0155 inches. The beam responded exactly in the first linear mode, and all of the models were in perfect agreement. Knowing the system energy of the response, the frequency-energy plot of the first NNM in Fig. 25 reveals that the system energy is in the linear range. However, the higher energy load cases in Tables 7 and 8 show that the energy of each response are in the nonlinear range of the first NNM. The ROMs with mode (1) and modes (1 MC) do not accurately predict the RMS and maximum displacements of the full order model at the higher energy levels. When looking at the first NNM, the nonlinear modal convergence analysis of each of these ROMs determined that additional modes were needed in the basis to capture the modal interactions predicted by the higher order ROMs. The mode (1) ROM showed considerable error in the backbone while the (1 MC) ROM captured it reasonably well. This confirms that the internal resonances do play an important role in the transient response, at least in the undamped case.

It is interesting to note that the 4-mode and 7-mode ROMs predict the RMS and maximum displacements quite accurately for each load case. In fact, the ROM with modes (1 3 5

7 9 11 MC) agrees very well with the full order model in the nonlinear range, with the largest error occurring when the system energy level was  $E = 5.0 \cdot 10^{-2}$  in-lbf and the ROM overpredicted the RMS displacement by 1.5%, and the maximum displacement by 1.6%. This ROM was quite acceptable even though it could not be confirmed that its first NNM had converged at all of the system's internal resonances. The internal resonances represent manifolds in the state space that connect different nonlinear modes; perhaps the ROMs need only capture the location (in terms of frequency and energy) and the density of these interactions in order to allow energy to propagate correctly and hence to predict the RMS and maximum displacement accurately.

The first 0.5 seconds of the displacement at the center of the beam is plotted in Fig. 29 for the full order model, and two of the ROMs (low and high fidelity), both of which include the augmented discontinuous basis vector. The ROM with modes (1 MC) (green dashed) overpredicts the amplitude of the response for all load cases in the nonlinear region (Fig. 29b-29d), and appears to be dominated by a single frequency.

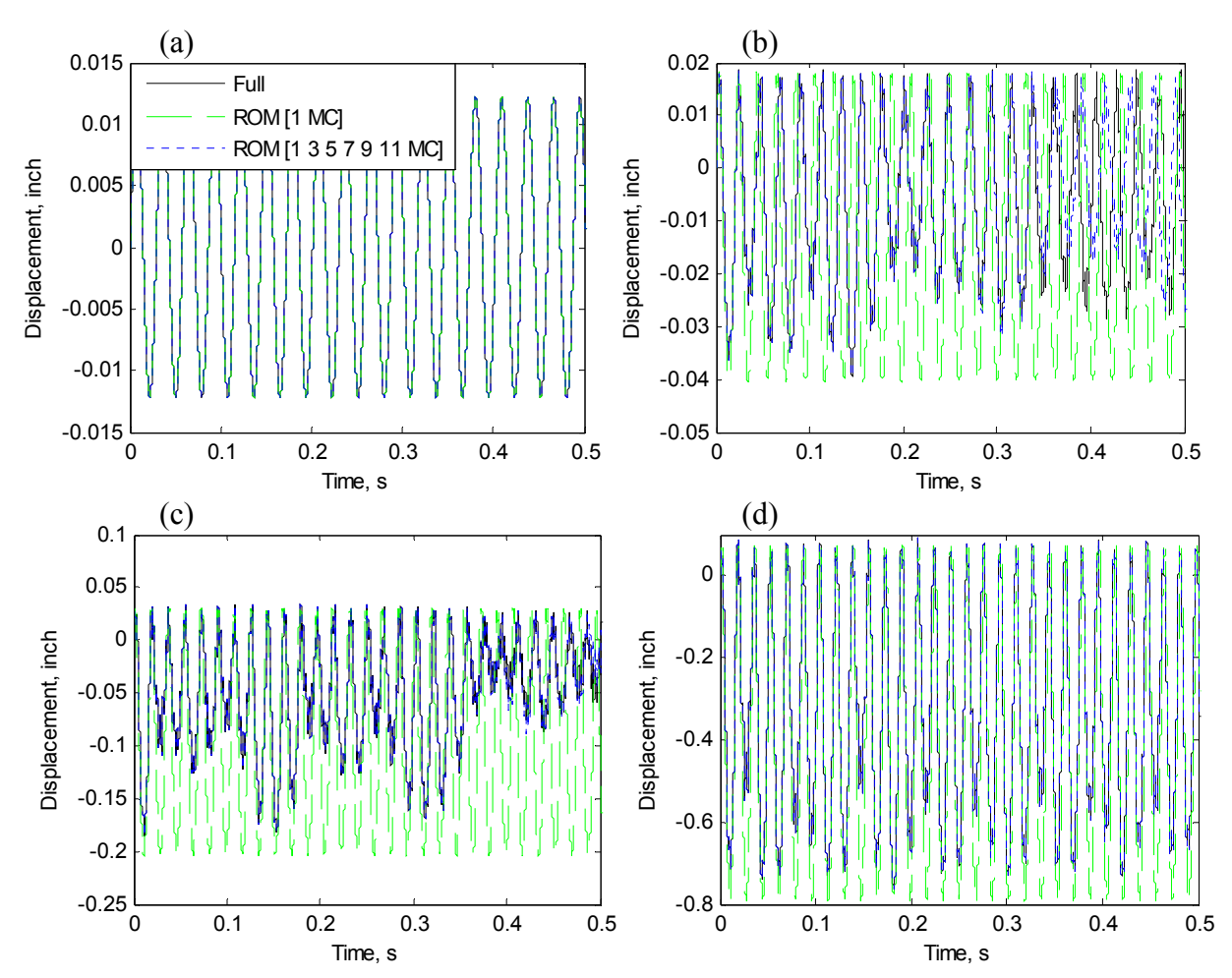


Figure 29. Response of contacting DOF due to a half-sine pulse in the shape of the first linear mode with system energy of (a)  $E = 1.8 \cdot 10^{-4}$  in-lbf, (b)  $E = 2.0 \cdot 10^{-3}$  in-lbf, (c)  $E = 5.0 \cdot 10^{-2}$  in-lbf, and (d) E = 0.76 in-lbf. (Solid black) full order model, (dashed green) ROM with modes (1 MC), and (short dashed blue) ROM with modes (1 3 5 7 9 11 MC).

In contrast, the ROM with modes (1 3 5 7 9 11 MC) closely follows the response predicted by the full model, capturing the higher harmonics and the relative amplitude of the displacement, although the predicted response does have a significant phase error after about 0.3 seconds. This divergence is common for systems with non-smooth nonlinearities. The first NNM in Fig. 25 shows many internal resonances at  $E = 2.0 \cdot 10^{-3}$  in-lbf, suggesting that the beam's response at this energy level could travel along one of these manifolds and pump energy into another nonlinear mode of the system, as was observed in the transient responses in [42]. Since

the 7-mode ROM did not appear to converge at all of the internal resonances, the response that it predicts may travel along other nearby paths potentially transferring energy to different nonlinear modes and ultimately causing the time response to diverge.

It is interesting to point out that Figure 29d shows that at E=0.76 in-lbf, the signals between the full model (solid black) and the ROM with modes (1 3 5 7 9 11 MC) (blue dotted) stay in phase over the entire period and appear to be in very good agreement. Figure 25 shows that, at this energy level, the backbone of the first NNM has leveled off and there are fewer internal resonances that can come into the path of the system; perhaps this causes the response to be more likely to travel on the manifold described by NNM 1 backbone and to oscillate at a fixed frequency. Even the (1 MC) ROM does a sufficient job at predicting the maximum and (to a lesser extent) RMS amplitudes and the frequency content in the response, further reinforcing the idea that the backbone is more important than the internal resonances at this energy level.

These comparisons have shown that, although the response of this beam shows vastly different character at different energy levels, its response is somehow connected to its nonlinear normal modes. A reduced order model that captures its nonlinear modes accurately is likely to correctly predict its response over the corresponding range of energy. In the next subsection, the damped ROMs are compared to the full order model using a random force input to evaluate the response capabilities with structural damping.

### 4.4.2 Random Loading Validation

The response to a random force applied at the midpoint of the beam in the transverse direction is presented here. A linear damping model was included in the reduced and full order equations of motion based on mass and stiffness proportional damping (i.e.  $\mathbf{C} = \alpha \mathbf{M} + \beta \mathbf{K}$ ), with

 $\alpha$  and  $\beta$  chosen so that the first and third modes of the linear beam had modal damping ratios of 0.5 %. The linear, diagonal damping matrix for the ROMs was derived from this diagonalizable damping matrix,  $\mathbf{C}$ . The lightly damped beam was forced using a broadband, Gaussian random input with zero mean and a standard deviation of  $\sigma$ . The input was filtered using an 8<sup>th</sup> order Butterworth filter with a cutoff frequency of 1,000 Hz, in order to excite (at least) the first three symmetric modes of the system. Figure 30 shows the autospectrum of the midpoint displacement for a forcing level with a standard deviation of  $\sigma = 0.1$  lbf.

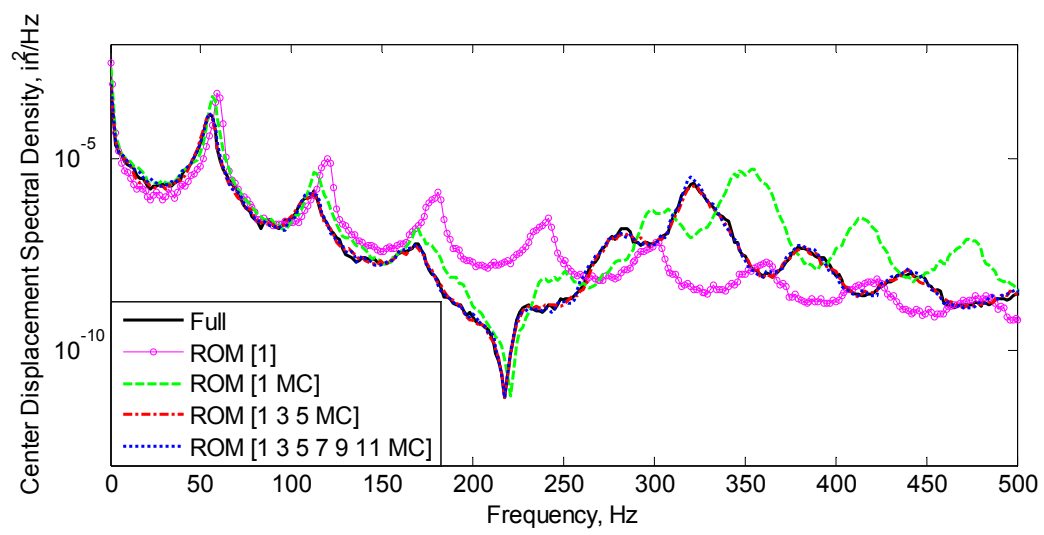


Figure 30. Autospectrum of the midpoint transverse displacement to a random force input with a standard deviation of  $\sigma = 0.1$  lbf.

All of the models show that the response was dominated by a peak around 54 Hz, which can be attributed to the first NNM. The harmonics of this peak occur at 108.8 Hz, 168 Hz, and so forth, and were especially prominent in the response of the one-mode ROM. Since this one-mode ROM did not have any internal resonances along the first NNM, these harmonics come from the response of the first mode. Some of those harmonics were visible in the response of the higher order ROMs. Overall the one-mode ROM poorly predicted the frequencies and amplitudes of these peaks. Furthermore, while this ROM predicted that the dominant frequency was near 54

Hz, the model was stiffer than the full order model since it overpredicted the response near the first mode, presumably because it did not have the pathways that would allow vibration energy to transfer to other NNMs.

The response predicted by the (1 MC) model improved near the 54 Hz resonance peak (as expected based on its NNM backbone), but it still overpredicted the amplitude of the response by a significant amount. It appeared that the first mode exchanged energy with the third mode and hence the model must explicitly include that mode in the basis in order to predict the response level accurately. The higher fidelity ROMs with modes (1 3 5 MC) and (1 3 5 7 9 11 MC) agree very well with the results from the full order model. The autospectrum in Fig. 30 suggests that the convergence of the backbone is the most important feature of the modal convergence study to infer about the accuracy of the damped response to a random load since the 4-mode and 7-mode ROMs predicted nearly the same response as the full order model, but predicted different internal resonances. The internal resonances are known to be important to some degree, however, since one could create a 7-mode model that neglects the coupling between the modes, and while such a model might capture accurately the backbones it would not predict the response amplitudes very accurately. This was illustrated in [41]. Even then, it appeared that for a system like this it was not critical that each internal resonance converge, as long as the system has some internal resonances at the energy level of interest.

### 4.5 Summary

This chapter presented three case studies involving reduced order models of nonlinear FEA models. The accuracy of these were evaluated based on the computed nonlinear normal modes either as modes were added to the basis, or as the scaling on the static loads were adjusted. The ICE and ED reduced order modeling strategies were used in Sections 4.2 and 4.3

to reduce two geometrically nonlinear finite element models to a low order set of nonlinear modal equations. The NNMs of the clamped-clamped beam and an exhaust cover plate helped guide the decisions to generate accurate models and were invaluable in this regard. NNMs are relatively inexpensive to compute from the NLROM and they readily show the differences and similarities between a candidate set of NLROMs and give physical insight into how the responses of the NLROMs might differ.

One disadvantage of the ED method is the requirement to include axial modes in the basis set, causing these ROM to have more DOF than those created with ICE. This increases the size of the NLROM, although it is still dramatically smaller than the original finite element model. Fortunately, the results have shown that a simple static force in the shape of a particular vibration mode can reveal which modes are coupled to it and should be augmented to the ED NLROM basis. The ICE NLROMs converged quickly for each finite element model studied in Chapter 4, requiring only a few modes to at least capture the NNM backbones. The ED method converged for the geometrically nonlinear beam with relatively few modes, but did not converge for the exhaust cover plate. A recent study [71] suggests that using dual modes [67] to capture the membrane kinematics improves the ED basis. The results on the exhaust cover plate in that paper converged to the backbone with only two bending modes and three dual modes.

The third case study presented here demonstrated the NNM convergence metric on a simply supported beam with a non-smooth, contact nonlinearity. The first NNM of the beam appeared to have converged along the backbone with either a four or seven mode ROM, however the internal resonance were not yet converged. The difficulty in computing the tongues along with the high density of these solutions made it difficult to evaluate the convergence of the system without studying higher order ROMs. The ROMs were validated with the full order

model by comparing the responses to an impulsive load and a random external force. The convergence along the backbone suggests that the peak and RMS response to an impulsive force will be in agreement, however the internal resonances seem to contribute to the divergence of the two signals over time. These results suggest that a ROM that accurately captured the backbone (and also included a similar density of internal resonances) would be adequate to predict the random and transient response, although no formal proof was shown.

It is believed that the comparison of nonlinear normal modes has great promise for other model reduction strategies of conservative systems. Previous works have focused on comparing the transient response or the power spectra of the response when a random input is applied, but those each depend on a forcing function and/or a prescribed initial condition. In contrast, the NNMs are unique solutions to the undamped equations of motion that exercise the model over a range of response amplitudes (or energy levels), and they are relatively quick to compute using numerical continuation algorithms. This work has shown that the NNMs serve as a valuable metric to assess the convergence of a NLROM equations, even if the reference solutions from the full order model are not available.

### 5 Nonlinear Modal Substructuring

#### 5.1 Introduction

A modal substructuring approach for geometrically nonlinear FEA models is proposed here by generating subcomponent reduced order models using the Implicit Condensation and Expansion procedure [19, 103] reduced with either

- i.) free-interface modes
- ii.) fixed-interface plus constraint modes (Craig-Bampton (CB) modes)
- iii.) fixed-interface plus characteristic constraint (CC) modes

After the subcomponent modal models are identified, they are assembled by satisfying force equilibrium and compatibility, just as done with linear systems [54, 74] or in finite element assembly [28]. Kuether and Allen first developed this nonlinear modal substructuring approach for subcomponent ROMs reduced with free-interface modes in [93], and later used fixed-interface plus constraint modes on the same assembly of two geometrically nonlinear beams having a connection interface with only 1-DOF [104, 105]. For a continuous interface with more than a few DOF, the number of static constraint modes would prohibit the use of ICE, or any ROM approach, hence motivating the use of characteristic constraint modes [82] to reduce the interface DOF. Kuether and Allen used fixed-interface plus characteristic constraint modes in [106] and then [107] to reduce the interface DOF of two geometrically nonlinear plate models with many connection points.

Dynamic substructuring analysis first divides the global structure of interest into smaller substructures, whose equations are reduced before being assembled to give a reduced order model. Therefore, the derivation starts with the discretized, geometrically nonlinear finite

element model of a subcomponent, giving the undamped, N-degrees-of-freedom equations of motion in the form,

$$\mathbf{M}\ddot{\mathbf{x}} + \mathbf{K}\mathbf{x} + \mathbf{f}_{NL}(\mathbf{x}) = \mathbf{f}(t)$$
(54)

where **M** and **K** are the  $N \times N$  linear mass and stiffness matrices, respectively.  $\mathbf{f}_{NL}(\mathbf{x})$  is the  $N \times 1$  nonlinear restoring force vector that accounts for the internal forces due to geometric nonlinearity. The  $N \times 1$  vectors  $\mathbf{x}$ ,  $\ddot{\mathbf{x}}$ , and  $\mathbf{f}(t)$  are the displacement, acceleration and external forces, respectively. The damping matrix can readily be included as well but will be omitted here for brevity. The nonlinear modal substructuring procedure is outlined in the following three subsections. Section 5.2 discusses a few choices for subcomponent modes to reduce each subcomponent FEA model in Eq. (54), Section 5.3 generates the reduced subcomponent model based on the modal basis chosen in Section 5.2, and Section 5.4 couples the nonlinear subcomponent models to obtain a reduced order model of the assembly.

# 5.2 Component Mode Basis Selection

In order to reduce each subcomponent FEA model, first a set of subcomponent modes, or Ritz vectors, are needed to capture the kinematics. This chapter presents three different types of linear basis functions used for substructuring and their theory is reviewed here. There are a variety of other modal bases that could be used [74] but only those listed below are addressed in this dissertation.

#### **5.2.1** Free-interface Modes

The free-interface modes (e.g. with no boundary constraints applied to the interface DOF) are the linear vibration modes computed from the linear mass and stiffness matrices in Eq. (54)

and are found by solving the eigenvalue problem  $(\mathbf{K} - \omega_r^2 \mathbf{M}) \mathbf{\varphi}_r$ . The modal transformation matrix using a truncated set of these mode shapes is given as,

$$\mathbf{x} = \mathbf{T}_{FI} \mathbf{q}_{FI} \tag{55}$$

The  $N \times m$  matrix,  $\mathbf{T}_{FI}$ , contains a truncated set of mass normalized, free-interface mode shapes,  $\mathbf{\phi}_r$ , in each of its columns. The reduced coordinate space  $\mathbf{q}_{FI}$  is significantly smaller than the physical coordinate space  $\mathbf{x}$  (i.e.  $m \ll N$ ).

### 5.2.2 Craig-Bampton Modes

Again starting with the *linear* form of the equations of motion in Eq. (54) (i.e. when  $\mathbf{f}_{NL}(\mathbf{x}) = \mathbf{0}$ ), each DOF in  $\mathbf{x}$  is first partitioned into either boundary DOF,  $\mathbf{x}_b$ , or interior DOF.  $\mathbf{x}_i$ . The boundary DOF are either shared by an adjacent structure, sometimes referred to as interface DOF, or may have been retained simply because an external point load  $\mathbf{f}(t)$  is applied to that location. The interior DOF are all the remaining coordinates of the system. The partitioned equations of motion of the linear model become

$$\begin{bmatrix} \mathbf{M}_{ii} & \mathbf{M}_{ib} \\ \mathbf{M}_{bi} & \mathbf{M}_{bb} \end{bmatrix} \begin{pmatrix} \ddot{\mathbf{x}}_{i} \\ \ddot{\mathbf{x}}_{b} \end{pmatrix} + \begin{bmatrix} \mathbf{K}_{ii} & \mathbf{K}_{ib} \\ \mathbf{K}_{bi} & \mathbf{K}_{bb} \end{bmatrix} \begin{pmatrix} \mathbf{x}_{i} \\ \mathbf{x}_{b} \end{pmatrix} = \begin{pmatrix} \mathbf{0} \\ \mathbf{f}(t) \end{pmatrix}$$
(56)

The fixed-interface modes are computed by restraining all the boundary coordinates,  $\mathbf{x}_b$ , and solving the eigenvalue problem  $(\mathbf{K}_{ii} - \omega_{ii,r}^2 \mathbf{M}_{ii}) \mathbf{p}_{ii,r} = \mathbf{0}$  from the linear system matrices partitioned to only the interior DOF,  $\mathbf{x}_i$ , in Eq. (56). These fixed-interface modes are then mass normalized with respect to  $\mathbf{M}_{ii}$ . These mode shapes are augmented with a set of static shapes, known as constraint modes, that account for deformations at the boundary, or interface, DOF.

One constraint mode is computed for every boundary coordinate in  $\mathbf{x}_b$  by computing the static deflection to a unit displacement at each boundary DOF while holding the other boundary coordinates fixed. These shapes are computed as

$$\Psi = \begin{bmatrix} \Psi_{ib} \\ \mathbf{I}_{bb} \end{bmatrix} = \begin{bmatrix} -\mathbf{K}_{ii}^{-1} \mathbf{K}_{ib} \\ \mathbf{I}_{bb} \end{bmatrix}$$
 (57)

The modal transformation matrix with fixed-interface modes and constraint modes then becomes

where  $\Phi_{ik}$  is the  $N_i \times N_k$  matrix of mass normalized fixed-interface modes, **I** is the identity matrix, and  $\Psi$  is the  $N \times N_b$  matrix of constraint modes. Typically, only a small set of  $N_k$  fixed-interface modes are needed in the basis and this truncation determines the level of accuracy of the assembled ROMs, as seen later in Chapter 6. The total number of modal coordinates in the vector  $\mathbf{q}_{CB}$  is the number of retained fixed-interface modes  $N_k$  plus the number of constraint modes  $N_b$ , denoted as  $m = N_k + N_b$ . The resulting  $N \times m$  matrix  $\mathbf{T}_{CB}$  is known in the literature as the Craig-Bampton transformation matrix, as discussed in [74, 76].

#### 5.2.3 Craig-Bampton Modes with Interface Reduction

To initiate the interface reduction using characteristic constraint modes [82], a linear reduced order model of the subcomponent is created by substituting Eq. (58) into Eq. (56) and pre-multiplying by the transpose, ()<sup>T</sup>, of the CB transformation matrix,  $\mathbf{T}_{CB}^{T}$ . A linear CB reduced order model for a subcomponent has the form,

$$\begin{bmatrix} \mathbf{I}_{kk} & \hat{\mathbf{M}}_{kb} \\ \hat{\mathbf{M}}_{bk} & \hat{\mathbf{M}}_{bb} \end{bmatrix} \begin{pmatrix} \ddot{\mathbf{q}}_{k} \\ \ddot{\mathbf{x}}_{b} \end{pmatrix} + \begin{bmatrix} \mathbf{\Lambda}_{kk} & \mathbf{0}_{kb} \\ \mathbf{0}_{bk} & \hat{\mathbf{K}}_{bb} \end{bmatrix} \begin{pmatrix} \mathbf{q}_{k} \\ \mathbf{x}_{b} \end{pmatrix} = \begin{pmatrix} \mathbf{0} \\ \mathbf{f}(t) + \mathbf{r}(t) \end{pmatrix}$$
(59)

The vector  $\mathbf{r}(t)$  is the unknown equal and opposite reaction force that will be applied by an adjacent connecting structure, and  $\mathbf{\Lambda}_{kk}$  is a diagonal matrix of squared natural frequencies of the fixed-interface modes. For FEA models with a very detailed mesh at the interface, there may be many thousands of DOF at the boundary requiring far too many constraint modes,  $\mathbf{\Psi}$ . A reduction of these boundary coordinates,  $\mathbf{x}_b$ , is sought using the approach in [82] by performing a second modal analysis. This is done by first assembling all the linear CB models from Eq. (59) following the classical CB approach [74, 76]. Without loss of generality, coupling two linear subcomponents denoted with superscripts (A) and (B) produces the equations of motion of the assembly

$$\begin{bmatrix} \mathbf{I}_{k_{A}k_{A}}^{(A)} & \mathbf{0} & \hat{\mathbf{M}}_{k_{A}b}^{(A)} \\ \mathbf{0} & \mathbf{I}_{k_{B}k_{B}}^{(B)} & \hat{\mathbf{M}}_{k_{B}b}^{(B)} \\ \hat{\mathbf{M}}_{bk_{A}}^{(A)} & \hat{\mathbf{M}}_{bk_{B}}^{(B)} & \hat{\mathbf{M}}_{bb}^{(A)} + \hat{\mathbf{M}}_{bb}^{(B)} \end{bmatrix} \begin{bmatrix} \ddot{\mathbf{q}}_{k_{A}}^{(A)} \\ \ddot{\mathbf{q}}_{k_{B}}^{(B)} \\ \ddot{\mathbf{x}}_{b} \end{bmatrix} + \begin{bmatrix} \boldsymbol{\Lambda}_{k_{A}k_{A}}^{(A)} & \mathbf{0} & \mathbf{0} \\ \mathbf{0} & \boldsymbol{\Lambda}_{k_{B}k_{B}}^{(B)} & \mathbf{0} \\ \mathbf{0} & \mathbf{0} & \hat{\mathbf{K}}_{bb}^{(A)} + \hat{\mathbf{K}}_{bb}^{(B)} \end{bmatrix} \begin{bmatrix} \mathbf{q}_{k_{A}}^{(A)} \\ \mathbf{q}_{k_{B}}^{(B)} \\ \mathbf{x}_{b} \end{bmatrix} = \begin{bmatrix} \mathbf{0} \\ \mathbf{0} \\ \mathbf{f}(t) \end{bmatrix}$$
(60)

A second modal analysis is performed on the linear mass and stiffness matrices corresponding to the boundary DOF,  $\mathbf{x}_h$ , in Eq. (60) by solving the eigenvalue problem

$$\left(\left(\hat{\mathbf{K}}_{bb}^{(A)} + \hat{\mathbf{K}}_{bb}^{(B)}\right) - \omega_r^2 \left(\hat{\mathbf{M}}_{bb}^{(A)} + \hat{\mathbf{M}}_{bb}^{(B)}\right) \psi_{CC,r} = \mathbf{0}$$
(61)

These boundary mode shape vectors,  $\Psi_{CC,r}$ , are then truncated and used to assemble the  $N_b \times N_c$  matrix  $\Psi_{CC}$ . The work in [82] uses this transformation to further reduce the assembly equations of motion in Eq. (60). However, this dissertation is interested in reducing the number

of constraint modes used to describe the interface in the CB transformation in Eq. (58), so  $\Psi_{CC}$  reduces the interface DOF as,

$$\mathbf{x} = \begin{cases} \mathbf{x}_i \\ \mathbf{x}_b \end{cases} = \begin{bmatrix} \mathbf{\Phi}_{ik} & \mathbf{\Psi}_{ib} \\ \mathbf{0} & \mathbf{I} \end{bmatrix} \begin{bmatrix} \mathbf{I} & \mathbf{0} \\ \mathbf{0} & \mathbf{\Psi}_{CC} \end{bmatrix} \begin{cases} \mathbf{q}_k \\ \mathbf{q}_c \end{cases} = \begin{bmatrix} \mathbf{\Phi}_{ik} & \hat{\mathbf{\Psi}}_{ic} \\ \mathbf{0} & \hat{\mathbf{\Psi}}_{bc} \end{bmatrix} \begin{Bmatrix} \mathbf{q}_k \\ \mathbf{q}_c \end{cases} = \mathbf{T}_{CC} \mathbf{q}_{CC}$$
(62)

 $\hat{\Psi}$  is now the  $N \times N_c$  matrix of characteristic constraint modes that capture the "characteristic" motion of the interface for a single subcomponent due to its connection to other subcomponents. The total number of generalized coordinates in the vector  $\mathbf{q}_{CC}$  becomes  $m = N_k + N_c$ , and the  $N \times m$  matrix  $\mathbf{T}_{CC}$  contains the fixed-interface modes and now the characteristic constraint modes. The generalized coordinates in the  $m \times 1$  vector  $\mathbf{q}_{CC}$  have significantly fewer DOF than total number of N physical DOF in Eq. (54), and the number of CB modal coordinates in Eq. (58).

# 5.3 Reduced Subcomponent Models with Geometric Nonlinearity

Without loss of generality, the modal basis for a subcomponent model is denoted with the matrix T and generalized coordinates q without the subscripts, as the following reduction procedure applies for any of the three modal bases given by Eqs. (55), (58), and (62). In order to reduce the full order, geometrically nonlinear model in Eq. (54), again the displacements, x, are sorted to the boundary and interior DOF as,

$$\begin{bmatrix} \mathbf{M}_{ii} & \mathbf{M}_{ib} \\ \mathbf{M}_{bi} & \mathbf{M}_{bb} \end{bmatrix} \begin{bmatrix} \ddot{\mathbf{x}}_{i} \\ \ddot{\mathbf{x}}_{b} \end{bmatrix} + \begin{bmatrix} \mathbf{K}_{ii} & \mathbf{K}_{ib} \\ \mathbf{K}_{bi} & \mathbf{K}_{bb} \end{bmatrix} \begin{bmatrix} \mathbf{x}_{i} \\ \mathbf{x}_{b} \end{bmatrix} + \begin{bmatrix} \mathbf{f}_{NL,i}(\mathbf{x}) \\ \mathbf{f}_{NL,b}(\mathbf{x}) \end{bmatrix} = \begin{bmatrix} \mathbf{0} \\ \mathbf{f}(t) \end{bmatrix}$$
(63)

The general transformation matrix, T, is substituted into Eq. (63), and premultiplied by  $T^T$  to create the reduced subcomponent equations of motion

$$\hat{\mathbf{M}}\ddot{\mathbf{q}} + \hat{\mathbf{K}}\mathbf{q} + \mathbf{T}^{\mathrm{T}} \begin{cases} \mathbf{f}_{NL,i}(\mathbf{T}\mathbf{q}) \\ \mathbf{f}_{NL,b}(\mathbf{T}\mathbf{q}) \end{cases} = \mathbf{T}^{\mathrm{T}} \begin{cases} \mathbf{0} \\ \mathbf{f}(t) + \mathbf{r}(t) \end{cases}$$
(64)

where

$$\hat{\mathbf{M}} = \mathbf{T}^{\mathsf{T}} \begin{bmatrix} \mathbf{M}_{ii} & \mathbf{M}_{ib} \\ \mathbf{M}_{bi} & \mathbf{M}_{bb} \end{bmatrix} \mathbf{T}$$
 (65)

$$\hat{\mathbf{K}} = \mathbf{T}^{\mathrm{T}} \begin{bmatrix} \mathbf{K}_{ii} & \mathbf{K}_{ib} \\ \mathbf{K}_{bi} & \mathbf{K}_{bb} \end{bmatrix} \mathbf{T}$$
 (66)

Note that, when implementing this for the free-interface modal basis in Eq. (55), the reduced modal mass and stiffness matrices ( $\hat{\mathbf{M}}$  and  $\hat{\mathbf{K}}$ ) are diagonal. It is assumed that the subcomponent FEA models are created in a commercial software package, so the unknown nonlinear modal restoring force can be defined generally as

$$\mathbf{T}^{\mathrm{T}} \begin{cases} \mathbf{f}_{NL,i}(\mathbf{T}\mathbf{q}) \\ \mathbf{f}_{NL,b}(\mathbf{T}\mathbf{q}) \end{cases} = \mathbf{\theta}(q_1, q_2, ..., q_m)$$
(67)

The nonlinear function  $\theta(q_1,q_2,...,q_m)$  depends on each of the modal coordinates,  $\mathbf{q}$ , in the reduction basis. Many common large displacement strain models [1, 4] have shown that  $\mathbf{f}_{NL}(\mathbf{x})$  is expressible as a quadratic and cubic polynomial function, therefore the same functional form will hold for the modal form of the equations, as done earlier in Chapter 3. Therefore, the  $r^{\text{th}}$  row of the nonlinear modal restoring force is given as,

$$\theta_r(q_1, q_2, \dots, q_m) = \sum_{i=1}^m \sum_{j=i}^m B_r(i, j) q_i q_j + \sum_{i=1}^m \sum_{j=i}^m A_r(i, j, k) q_i q_j q_k$$
(68)

The nonlinear stiffness coefficients  $A_r$  and  $B_r$  are not explicitly available when the FEA models are built directly in a commercial software package, so one of the indirect approaches from Chapter 3 is used to determine these values.

This work uses the Implicit Condensation and Expansion method in [103] to estimate unknown coefficients by applying a series of static forces to the full, nonlinear FEA substructure model in Eq. (54). The FEA software performs the static analyses to determine the resulting deformations to a permutation of static forces that are the sums and differences of either one, two or three of the subcomponent modes in  $\mathbf{T}$ . For example, the  $c^{th}$  static force combination of the  $r^{th}$ ,  $s^{th}$ , and  $v^{th}$  mode shapes can be arbitrarily defined as

$$\mathbf{F}_{c} = \begin{bmatrix} \mathbf{K}_{ii} & \mathbf{K}_{ib} \\ \mathbf{K}_{bi} & \mathbf{K}_{bb} \end{bmatrix} \left( \mathbf{T}_{r} \hat{f}_{r} + \mathbf{T}_{s} \hat{f}_{s} + \mathbf{T}_{v} \hat{f}_{v} \right)$$
(69)

The load scaling factors  $\hat{f}_r$ ,  $\hat{f}_s$ , and  $\hat{f}_v$  correspond to the force amplitude applied for the mode in the  $r^{\text{th}}$ ,  $s^{\text{th}}$ , and  $v^{\text{th}}$  column of the matrix  $\mathbf{T}$ , and  $\mathbf{F}_c$  is an  $N \times 1$  static force vector for the  $c^{\text{th}}$  load case. Note that the linear combinations of mode shapes in  $\mathbf{F}_c$  are premultiplied by the stiffness matrix instead of the mass matrix since the fixed-interface modes are orthogonal with respect to  $\mathbf{K}$  and not  $\mathbf{M}$ . A set of these force permutations and the computed responses are used with the unconstrained least squares approach [19] to fit the unknown coefficients  $A_r$  and  $B_r$ . More details on this fitting procedure can be found in [19], and more specific details on the load scaling and force permutations can be found in [19, 105] or in Chapter 3.

There is an upfront CPU cost incurred by the ICE procedure as a result of the static analyses required to fit the modal equations. The number of load cases to fit the coefficients in Eq. (68) scales as

# load cases = 
$$2m + \frac{2m!}{(m-2)!} + \frac{4m!}{3(m-3)!}$$
 (70)

where again *m* is the total number of modes used in the basis. One advantage of the ICE procedure is that only bending type modes need to be included in the transformation matrix **T** since the effects of membrane-bending coupling are implicitly captured in the coefficients, hence reducing the total number of static load cases. Since the ICE basis does not contain any membrane or axial type motions, the expansion process discussed in Section 3.7 and in [103, 105] can be used as a post processing step to accurately recover the in-plane deformations caused by the geometric nonlinearity, allowing these models to more accurately predict strains and stresses.

Once the coefficients of the subcomponent modal models have been computed, the equations of motion are then cast into the form proposed by Nash [117] to facilitate coupling. First, the quadratic and cubic terms in Eq. (68) are separated into two nonlinear restoring force vectors,  $\boldsymbol{\beta}$  and  $\boldsymbol{\alpha}$ , respectively, as

$$\boldsymbol{\beta} = \begin{bmatrix} \beta_1 & \beta_2 & \dots & \beta_m \end{bmatrix}^T \quad \text{where} \quad \beta_r = \sum_{i=1}^m \sum_{j=i}^m B_r(i, j) q_i q_j$$
 (71)

$$\boldsymbol{\alpha} = \begin{bmatrix} \alpha_1 & \alpha_2 & \dots & \alpha_m \end{bmatrix}^T \quad \text{where} \quad \alpha_r = \sum_{i=1}^m \sum_{j=i}^m \sum_{k=j}^m A_r(i,j,k) q_i q_j q_k$$
 (72)

These vectors are then differentiated with respect to each generalized coordinate in order to produce the quadratic and cubic stiffness matrices as,

$$\mathbf{N}_{1}(\mathbf{q}) = \frac{\partial \mathbf{\beta}}{\partial \mathbf{q}} = \begin{bmatrix} \frac{\partial \mathbf{\beta}}{\partial q_{1}} & \frac{\partial \mathbf{\beta}}{\partial q_{2}} & \dots & \frac{\partial \mathbf{\beta}}{\partial q_{m}} \end{bmatrix}$$
(73)

$$\mathbf{N}_{2}(\mathbf{q}) = \frac{\partial \mathbf{\alpha}}{\partial \mathbf{q}} = \begin{bmatrix} \frac{\partial \mathbf{\alpha}}{\partial q_{1}} & \frac{\partial \mathbf{\alpha}}{\partial q_{2}} & \dots & \frac{\partial \mathbf{\alpha}}{\partial q_{m}} \end{bmatrix}$$
(74)

The ROM in Eq. (64) is then rewritten in matrix form with the nonlinear stiffness matrices in Eqs. (73) and (74) as,

$$\hat{\mathbf{M}}\ddot{\mathbf{q}} + \hat{\mathbf{K}}\mathbf{q} + \frac{1}{2}\mathbf{N}_{1}(\mathbf{q})\mathbf{q} + \frac{1}{3}\mathbf{N}_{2}(\mathbf{q})\mathbf{q} = \mathbf{T}^{\mathrm{T}} \begin{cases} \mathbf{0} \\ \mathbf{f}(t) + \mathbf{r}(t) \end{cases}$$
(75)

## 5.4 Coupling Nonlinear Subcomponent Models

The subcomponent models in Eq. (75) are then coupled to any adjacent nonlinear (or possibly linear) substructure(s). This is done by forming the unconstrained equations of motion for an assembly. Without loss of generality, two ROMs can be assembled as,

$$\begin{bmatrix} \hat{\mathbf{M}}^{(A)} & \mathbf{0} \\ \mathbf{0} & \hat{\mathbf{M}}^{(B)} \end{bmatrix} \begin{bmatrix} \ddot{\mathbf{q}}^{(A)} \\ \ddot{\mathbf{q}}^{(B)} \end{bmatrix} + \begin{bmatrix} \hat{\mathbf{K}}^{(A)} & \mathbf{0} \\ \mathbf{0} & \hat{\mathbf{K}}^{(B)} \end{bmatrix} \begin{bmatrix} \mathbf{q}^{(A)} \\ \mathbf{q}^{(B)} \end{bmatrix} + \frac{1}{2} \begin{bmatrix} \mathbf{N}_{1}^{(A)}(\mathbf{q}^{(A)}) & \mathbf{0} \\ \mathbf{0} & \mathbf{N}_{1}^{(B)}(\mathbf{q}^{(B)}) \end{bmatrix} \begin{bmatrix} \mathbf{q}^{(A)} \\ \mathbf{q}^{(B)} \end{bmatrix} +$$

$$+ \frac{1}{3} \begin{bmatrix} \mathbf{N}_{2}^{(A)}(\mathbf{q}^{(A)}) & \mathbf{0} \\ \mathbf{0} & \mathbf{N}_{2}^{(B)}(\mathbf{q}^{(B)}) \end{bmatrix} \begin{bmatrix} \mathbf{q}^{(A)} \\ \mathbf{q}^{(B)} \end{bmatrix} = \begin{bmatrix} \mathbf{T}^{(A)^{T}} \begin{bmatrix} \mathbf{0} \\ \mathbf{f}^{(A)}(t) + \mathbf{r}^{(A)}(t) \end{bmatrix} \\ \mathbf{T}^{(B)^{T}} \begin{bmatrix} \mathbf{0} \\ \mathbf{f}^{(B)}(t) + \mathbf{r}^{(B)}(t) \end{bmatrix}$$

The reaction forces  $\mathbf{r}(t)$  at each interface DOF are unknown, but must be included in order to satisfy force equilibrium at the interface.

Compatibility requires that the coordinates at the interface be equal, meaning that  $\mathbf{x}_b^{(A)} = \mathbf{x}_b^{(B)}$  at the connection DOF (note that this is satisfied with  $\mathbf{q}_c^{(A)} = \mathbf{q}_c^{(B)}$  when using characteristic constraint modes). These constraint equations plus the unconstrained equations of motion in Eq. (76) fully characterize the assembled system. Every solution found in terms of the constrained coordinates  $\mathbf{q}^{(A)}$  and  $\mathbf{q}^{(B)}$  must always satisfy compatibility and force equilibrium,

making these equations inconvenient to deal with (although this is possible and has been implemented in various parallel computing algorithms [118]). This is addressed by defining the substructure coupling matrix L and using it to eliminate the redundant DOF in Eq. (76). The constrained coordinates can be transformed to a set of unconstrained coordinates as,

Then, by substituting Eq. (77) into Eq. (76) and pre-multiplying by  $\mathbf{L}^T$ , the equations of motion for the assembly become

$$\mathbf{L}^{T} \begin{bmatrix} \hat{\mathbf{M}}^{(A)} & \mathbf{0} \\ \mathbf{0} & \hat{\mathbf{M}}^{(B)} \end{bmatrix} \mathbf{L} \dot{\mathbf{q}}_{u} + \mathbf{L}^{T} \begin{bmatrix} \hat{\mathbf{K}}^{(A)} & \mathbf{0} \\ \mathbf{0} & \hat{\mathbf{K}}^{(B)} \end{bmatrix} \mathbf{L} \mathbf{q}_{u} + \frac{1}{2} \mathbf{L}^{T} \begin{bmatrix} \mathbf{N}_{1}^{(A)} (\mathbf{q}^{(A)}) & \mathbf{0} \\ \mathbf{0} & \mathbf{N}_{1}^{(B)} (\mathbf{q}^{(B)}) \end{bmatrix} \mathbf{L} \mathbf{q}_{u}$$

$$+ \frac{1}{3} \mathbf{L}^{T} \begin{bmatrix} \mathbf{N}_{2}^{(A)} (\mathbf{q}^{(A)}) & \mathbf{0} \\ \mathbf{0} & \mathbf{N}_{2}^{(B)} (\mathbf{q}^{(B)}) \end{bmatrix} \mathbf{L} \mathbf{q}_{u} = \mathbf{L}^{T} \begin{bmatrix} \mathbf{T}_{A}^{(A)T} \begin{bmatrix} \mathbf{0} \\ \mathbf{f}(t)^{(A)} \end{bmatrix} \\ \mathbf{T}^{(B)T} \begin{bmatrix} \mathbf{0} \\ \mathbf{f}(t)^{(B)} \end{bmatrix}$$

The reaction forces disappear after premultiplying by  $\mathbf{L}^{T}$ , and the unconstrained coordinates  $\mathbf{q}_{u}$  always satisfy compatibility, as discussed in [54, 73, 74]. The assembled equations of motion in Eq. (78) can be created in terms of the connectivity matrix  $\mathbf{L}$ , and each of the subcomponent ROMs identified in the previous subsection. The free or forced response to a given initial condition or time varying external force can be integrated using these nonlinear differential equations at a significantly lower cost than directly integrating a full order FEA model of the assembly. The modal substructuring methodology is demonstrated in Chapter 6 by computing the nonlinear normal modes of the ROM in Eq. (78) with various combinations of component modes included in basis in either Eqs. (55), (58), or (62).

# 6 Applications of Nonlinear Modal Substructuring

### 6.1 Coupling Two Beams with Geometric Nonlinearity

The modal substructuring approach is demonstrated here by coupling two geometrically nonlinear beams with simple supports; a schematic of this is shown in Fig. 31. These two beams represent simplified, scaled models of adjacent skin panels on an aircraft that could be used to predict the nonlinear vibrations caused by extreme pressure and acoustic loads during flight. Each substructure (A) and (B) was modeled in Abaqus® using B31 Euler-Bernoulli beam elements; the 9-inch (229 mm) beam had a total of 119 DOF, and the 6-inch (152 mm) beam had 89 DOF. The full FEA model of the total structure (C) was also constructed in Abaqus® in order to provide truth data to validate the modal convergence of the substructuring approaches. The subcomponents have the material properties of structural steel with a Young's modulus of 29,700 ksi (204.8 GPa), shear modulus of 11,600 ksi (80 GPa), and a mass density of 7.36·10<sup>-4</sup> lb-s<sup>2</sup>/in<sup>4</sup> (7,870 kg/m³). Both beams had cross sectional dimensions of 0.031 inches (0.787 mm) thick by 0.5 inches (12.7 mm) wide.

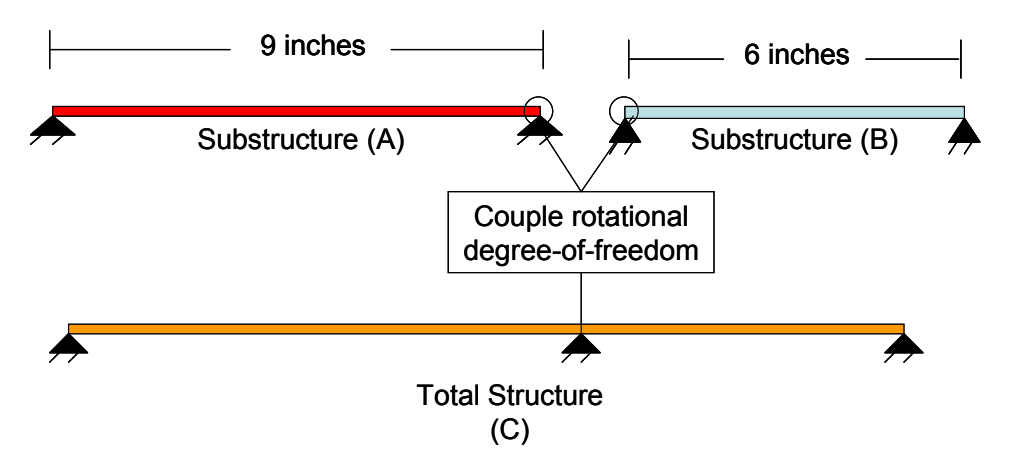


Figure 31. Schematic of coupling of two geometrically nonlinear beams with simply supported boundary conditions.

In the following subsection, the modal convergence of two *linear* substructuring approaches (i.e. when  $\mathbf{f}_{NL}(\mathbf{x}) = \mathbf{0}$  for each subcomponent model in Eq. (63)) are compared when using the CB modal basis in Eq. (58), and the other with the free-interface modes in Eq. (55). In Section 6.1.2, the *nonlinear* substructuring approach is demonstrated on the same example problem, except that  $\mathbf{f}_{NL}(\mathbf{x}) \neq \mathbf{0}$ . The nonlinear subcomponent ROMs with CB modes are referred as CB-NLROMs, and those created with free-interface modes are referred as NLROMs. Note that the interface between each beam had only one rotational DOF, therefore each CB basis required only a single constraint mode, and no reduction at the interface could be performed using characteristic constraint modes.

### **6.1.1** Linear Substructuring

The linear models of the 9-inch (229 mm) and 6-inch (152 mm) beams were used to predict the linear normal modes of the total structure (C) using a free-interface modal substructuring approach and a Craig-Bampton substructuring approach. One typically includes modes up to 1.5 to 2.0 times the maximum frequency of interest in the subcomponent ROMs. The linear natural frequencies for the first thirteen modes (all bending) of each subcomponent beam model are given in Table 9, along with the exact natural frequencies of the full finite element model of the total structure (C). The first 5 modes of the total structure are taken to be the modes of interest, covering a frequency range from 0 to 500 Hz.

Table 9. Exact linear natural frequencies of finite element models in Fig. 31.

	Simply Support B	Beam (A): 9 inch	Simply Support E	<b>Total Structure</b>	
Mode Number	Free-Interface	Fixed-Interface	Free-Interface	Fixed-Interface	<b>(C)</b>
1	34.85 Hz	54.44 Hz	78.41 Hz	122.5 Hz	42.50 Hz
2	139.4 Hz	176.5 Hz	313.8 Hz	397.3 Hz	97.73 Hz
3	313.8 Hz	368.4 Hz	706.4 Hz	829.5 Hz	162.7 Hz
4	558.2 Hz	630.4 Hz	1,257 Hz	1,420 Hz	313.8 Hz
5	872.7 Hz	962.8 Hz	1,966 Hz	2,170 Hz	382.1 Hz
6	1,258 Hz	1,366 Hz	2,835 Hz	3,080 Hz	588.0 Hz
7	1,714 Hz	1,840 Hz	3,866 Hz	4,153 Hz	762.5 Hz
8	2,241 Hz	2,385 Hz	5,059 Hz	5,389 Hz	930.0 Hz
9	2,840 Hz	3,003 Hz	6,417 Hz	6,791 Hz	1,257 Hz
10	3,511 Hz	3,693 Hz	7,942 Hz	8,361 Hz	1,392 Hz
11	4,256 Hz	4,457 Hz	9,636 Hz	10,100 Hz	1,766 Hz
12	5,074 Hz	5,295 Hz	11,500 Hz	12,020 HZ	2,060 Hz
13	5,966 Hz	6,208 Hz	13,540 Hz	14,110 Hz	2,333 Hz

To be conservative with the target range of 500 Hz, the linear substructuring analysis started by including subcomponent modes (either free-interface or fixed-interface) with frequencies up to 1,000 Hz. Additional cutoff frequencies were considered, namely 2,000 and 4,000 Hz, in order to evaluate the modal convergence as additional modes were included in the basis. These high frequency basis vectors will be especially important for the nonlinear substructuring case in Section 6.1.2, since higher frequency modes may become coupled to the lower frequency modes at large response amplitudes. The resulting percent errors of each predicted natural frequency are given in Table 10 for each linear substructuring approach with various subcomponent mode frequency ranges. The exact frequencies of the FEA model of the total structure (C) are used to compute these errors.

Table 10. Percent error of the predicted linear natural frequencies of the total structure (C) using subcomponent models that include modes up to 1,000 Hz, 2,000 Hz and 4,000 Hz.

Total Structure (C)	% Error with subcomponent modes up to		% Error with subcomponent modes up		% Error with subcomponent modes up	
Mode Number	1,000 Hz		to 2,000		to 4,000 Hz	
	Free-Interface	CB Modes	Free-Interface	CB Modes	Free-Interface	CB Modes
	Modes		Modes		Modes	
1	3.2	5.5·10 <sup>-4</sup>	2.1	5.2·10 <sup>-4</sup>	1.5	5.1.10-4
2	5.5	1.6·10 <sup>-4</sup>	3.5	2.4·10 <sup>-4</sup>	2.4	3.1·10 <sup>-4</sup>
3	9.3	1.9·10 <sup>-3</sup>	5.4	1.3·10 <sup>-3</sup>	3.6	$1.2 \cdot 10^{-3}$
4	2.8·10 <sup>-6</sup>	$2.5 \cdot 10^{-2}$	$3.4 \cdot 10^{-6}$	$4.1 \cdot 10^{-3}$	$3.7 \cdot 10^{-6}$	$4.5 \cdot 10^{-4}$
5	15	$3.4 \cdot 10^{-3}$	8.7	$1.5 \cdot 10^{-3}$	5.6	1.1·10 <sup>-3</sup>
6	5.2	0.10	2.7	1.6·10 <sup>-2</sup>	1.8	$1.4 \cdot 10^{-3}$
7	7.4	0.30	4.2	4.1·10 <sup>-2</sup>	2.8	$4.2 \cdot 10^{-3}$
8	N/A	0.22	8.2	2.6·10 <sup>-2</sup>	4.7	2.3·10 <sup>-3</sup>

When including subcomponent modes up to 1,000 Hz, the free-interface approach found a maximum frequency error of 15 % in the 5<sup>th</sup> assembly mode. As expected, this basis was not well suited for this example since the kinematics of the subcomponent do not account for deformation at the rotational interface [74], and one would need far more free-interface modes before the basis could begin to properly describe this motion. Interestingly, because the lengths of the two beams have a ratio 1.5:1, the 4<sup>th</sup> mode of the assembly is perfectly described by combining one free-interface mode of each, so its natural frequency is estimated very precisely using this basis. The CB approach with fixed-interface modes up to 1,000 Hz produced a far more accurate assembly model because of the kinematics supplied by the constraint modes, and had a maximum error of 0.30 % for the 7<sup>th</sup> assembly mode. As expected, out beyond the frequency range of the CB modal basis the errors become quite large; the error in the 9<sup>th</sup> and last predicted mode was 62% (not shown in Table 10).

Including a higher frequency bandwidth, up to 2,000 Hz and 4,000 Hz, improved the modal predictions with the free-interface approach, however the error was still in excess of 5% for the 5<sup>th</sup> mode when including modes up to 4,000 Hz, as compared to 0.0011% for the CB

model. These results show that the CB modal basis performs much better than the free-interface modes, as expected for problems with rigid connections at the interface. For problems with softer connections (e.g. through rubber grommets as in the auto industry), the free-interface modes would be expected to perform better.

#### **6.1.2** Nonlinear Substructuring

The nonlinear modal substructuring approaches with the CB-NLROMs and NLROMs generated with free-interface modes are demonstrated on the example in Fig. 31, but now with the geometric nonlinearity included in each subcomponent model such that  $\mathbf{f}_{NL}(\mathbf{x}) \neq \mathbf{0}$ . The modal convergence of the assembled models was evaluated by comparing its nonlinear normal modes, which were computed from the assembled equations of motion in Eq. (78) using the pseudo-arclength continuation algorithm in [49]. The NNMs were also computed from the full order finite element model of the total structure (C) using the Applied Modal Force (AMF) algorithm in Chapter 2 to provide a truth solution for comparison.

Figures 32 and 33 show the frequency-energy plots (FEPs) of the first five NNMs, where the fundamental frequency of the periodic motion is plotted on the vertical axis, and the total conserved energy (kinetic plus potential) is on the horizontal axis. The energy at which the AMF results reach a transverse displacement of one beam thickness is marked for reference in Fig. 32. As noted in the legend, the substructuring results are shown for three cases: two from assembled CB-NLROMs with fixed-interface modes up to 1,000 Hz and 4,000 Hz, and one with assembled NLROMs that used free-interface modes up to 4,000 Hz. When generating the static loads to fit the nonlinear stiffness coefficients of the ROMs, the best practices with the ICE approach in Chapters 3 and 4 were followed so the CLD scaling factors (from Section 3.5.2) in Eq. (69) were

chosen such that a  $w_{\text{max},r}$  was set to 0.25 times the beam thickness, or  $7.75 \cdot 10^{-3}$  inches (0.197 mm), and the reduction factor from Section 3.5.2 was used to lower the scale of multi-mode forces. It was determined that the unconstrained least squares approach in [19] had to be used to obtain good results with nonlinear substructuring, whereas the results on the monolithic structures in Chapter 4 were less sensitive and used the constrained least squares approach.

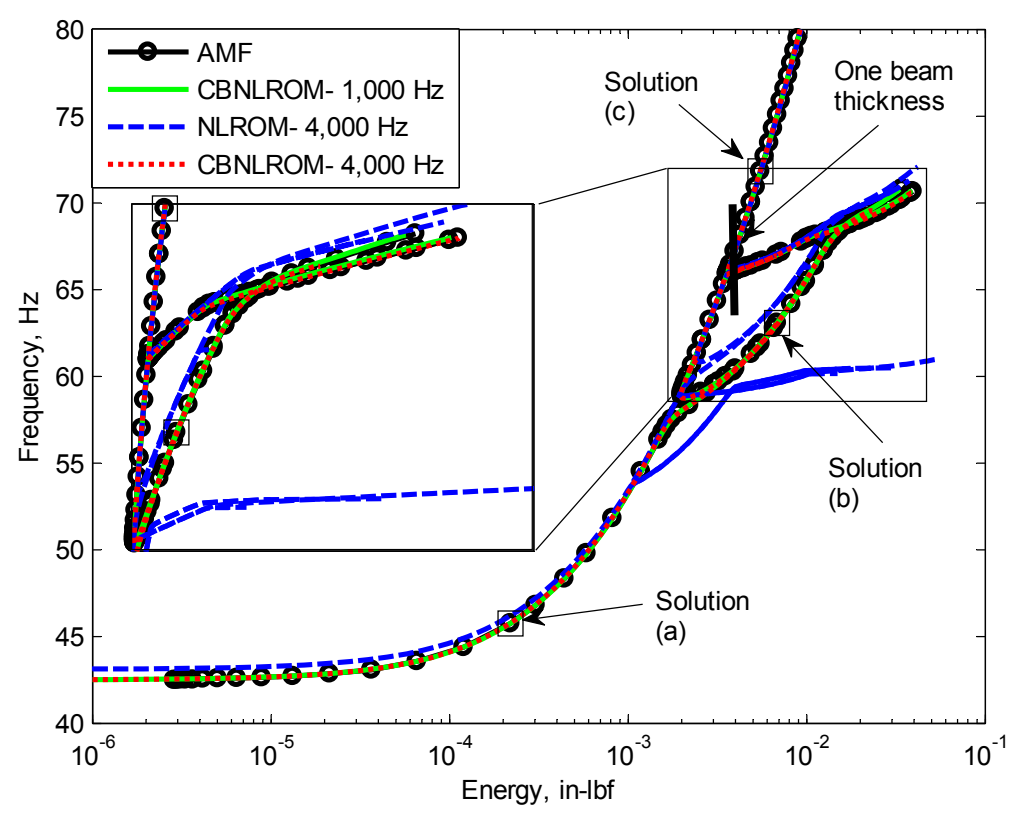


Figure 32. NNM 1 of the beam assembly using (black circles) AMF on the full FEA model of the total structure (C), (green solid) assembled CB-NLROMs with fixed-interface modes up to 1,000 Hz, (blue dashed) assembled NLROMs with free-interface modes up to 4,000 Hz, and (red dotted) assembled CB-NLROMs with fixed-interface modes up to 4,000 Hz.

The first NNM initiated at the first linear mode solution at low energy, and continued to higher response amplitudes as energy increased. These elevated response amplitudes introduced contributions from the nonlinear restoring force, as indicated by the increase in the fundamental frequency on the vertical axis. This hardening behavior is due to the coupling between the

bending and membrane motions, which causes axial stretching when the bending displacements become large enough. Two distinct features were observed in the FEPs of the first NNM in Fig. 32, namely the main backbone curve and the tongues emanating from this backbone. The main backbone traced the NNM at the lowest possible energy for a given frequency, and the tongues indicated the presence of a modal interaction with higher order NNMs at a strict integer ratio of oscillating frequencies. There were two modal interactions computed with NNM 1 using the AMF algorithm. For example, the first one initiated around 58 Hz, which started as a 3:1 interaction with NNM 3, meaning that the third mode oscillated at a frequency three times that of the first mode (note that this time response is shown later in Fig. 34). As the energy increased along this tongue, another tongue extended from the this one at 68 Hz, resulting in an interaction where the 4<sup>th</sup> NNM oscillated at a 5:1 frequency ratio with NNM 1, the 6<sup>th</sup> NNM oscillated at a 7:1 ratio, all while the 3<sup>rd</sup> NNM continued to oscillate at the 3:1 ratio.

The main backbone and two modal interactions along NNM 1 were accurately predicted by the two assembled CB-NLROMs with fixed-interface modes up to 1,000 Hz and 4,000 Hz, as seen by the agreement with the AMF results. Increasing the number of modes in the CB-NLROMs did not appear to change the FEP of NNM 1, so either CB-NLROM model could be confidently used. The assembled NLROMs with free-interface modes up to 4,000 Hz also performed quite well, but was not as accurate as the assembled CB-NLROMs. At low energy, there was slight disagreement in frequency, exactly as predicted by the linear substructuring results in the prior subsection. As the energy increased and the backbone started to bend up in frequency, the assembled NLROMs accurately matched the main backbone of NNM 1. However, the tongues emanating from this backbone were not as accurate, and the assembled NLROM model predicted two new modal interactions that were not present with either the AMF

algorithm or the CB-NLROMs. Since these interactions are strongly dependent on the accuracy of the higher order NNMs involved, these spurious tongues likely came about because the higher NNMs in the NLROM were not sufficiently accurate. Some of the higher NNMs of the assembly are plotted in Fig. 33.

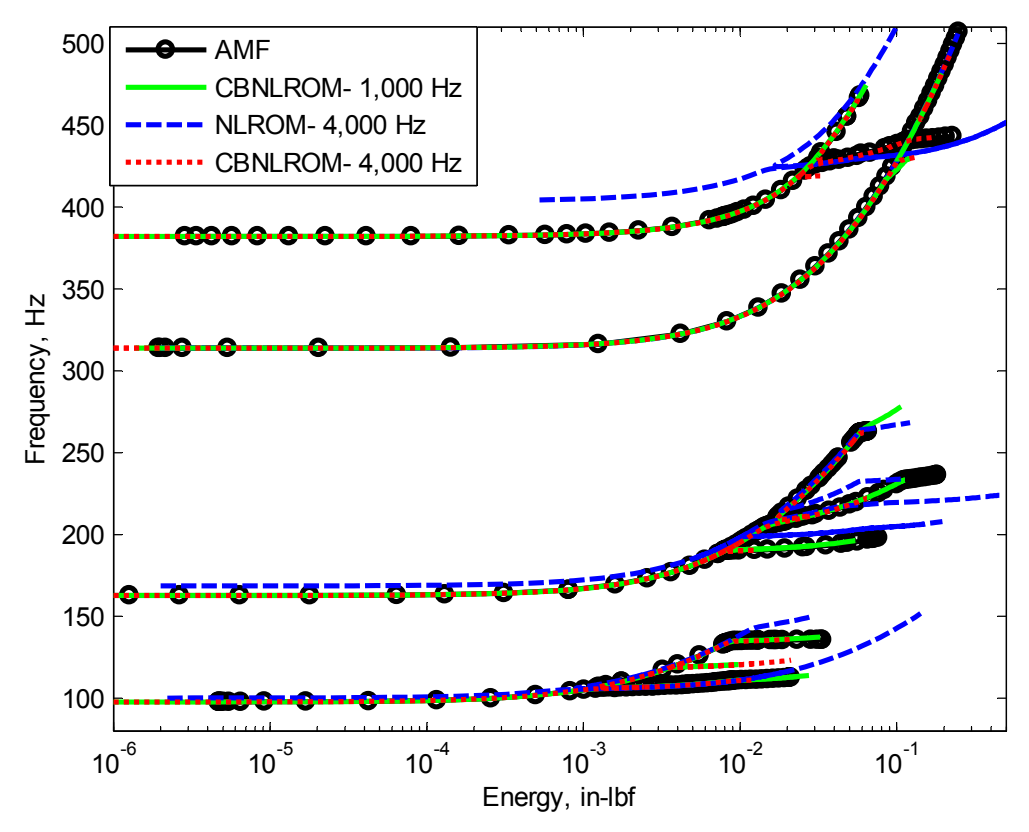


Figure 33. NNMs 2 through 5 of the beam assembly, see caption in Fig. 32 for further detail.

The higher order NNMs, spanning frequencies up to 500 Hz, offer similar conclusions as those seen with the first NNM. Again the FEPs computed with the assembled CB-NLROMs matched very well with FEPs computed with the AMF algorithm. Either CB-NLROM seems adequate, although on NNM 5 the lower order model was unable to predict a modal interaction at 425 Hz. Further investigation revealed that this was a 3:1 modal interaction with NNM 9. In Section 6.2.1 it was found that the 9<sup>th</sup> predicted linear assembly mode was in error of 62 % when

using CB modes up to 1,000 Hz, so it makes sense that this modal interaction would be erroneously predicted. Other than that, there was little difference between the assembled CB-NLROM results with the 1,000 Hz and 4,000 Hz bandwidth, suggesting that both would be adequate for response prediction.

Again the assembled NLROMs with free-interface modes were initially in error at low energy but predicted each NNM quite well as the branch bent upwards in frequency. The modal interactions predicted by these models were not as accurate as the assembled CB-NLROMs for NNMs 2 through 5. As noted previously, because the beam lengths had a 1.5:1 ratio, the fourth linear mode of the assembly was estimated perfectly by the free-interface mode basis. Here one also observes that the corresponding 4<sup>th</sup> NNM is also estimated very precisely using this same basis. The fifth NNM is significantly in error even though the NLROMs included linear modes up to 4,000 Hz. These results would be improved with additional free-interface modes in the basis set, but this was not explored in this work as more modes in the basis would increase the number of static loads needed to extract the NLROM from the finite element model.

Here the assembled CB-NLROMs had either 9 or 17 DOF, and needed a total of 296 and 1,940 load cases, respectively, to create the ROMs of each subcomponent. For example, the CB-NLROM under 1,000 Hz had a 6-mode ROM for the 9-inch beam (5 fixed-interface below 1,000 Hz plus 1 constraint mode), and required 232 static load cases. For the 6-inch beam, the CB-NLROM with 4 modes (3 fixed-interface plus 1 constraint) needed 64 static loads. Thus, the CB-NLROM eventually had 9 DOF after coupling and required 296 static loads to construct. Therefore, this equated to approximately 4 minutes of computational time on a desktop computer with an Intel® Core i7 CPU and 8 GB of RAM, and the 17 DOF model with 1,940 total load cases took about 15 minutes. The assembled NLROMs had 16 DOF, which required a total of

1,538 load cases and 10 minutes of CPU time. Directly building an NLROM of the total structure (C) with modes up to 4,000 Hz (equivalent to 17 bending modes) would require a total of 6,018 load cases, or 121 minutes. For reference, each NNM curve computed from the FEA model of the total structure (C) using AMF would take anywhere between 2-4 hours on the computer mentioned, whereas computing it from any ROM would take approximately 2-4 minutes.

The accuracy of these two nonlinear substructuring approaches was further evaluated by comparing the time histories at three points on the FEP in Fig. 32, which are marked as solutions (a), (b) and (c). When comparing the NNMs, the solution at the same energy level as the AMF solution was selected for the NNM of each assembled ROM. Solutions (a) and (c) were chosen to show how the response evolved along the main backbone as energy in the response increased, and solution (b) shows a response on one of the tongues in order to highlight how the beam vibrates during a modal interaction. The physical response over one period was projected onto the predicted linear modes of the assembly, which were first normalized to a unit maximum displacement in order to give the resulting modal amplitudes units of inches, and the resulting time histories of the three most dominant modes are shown in Fig. 34.

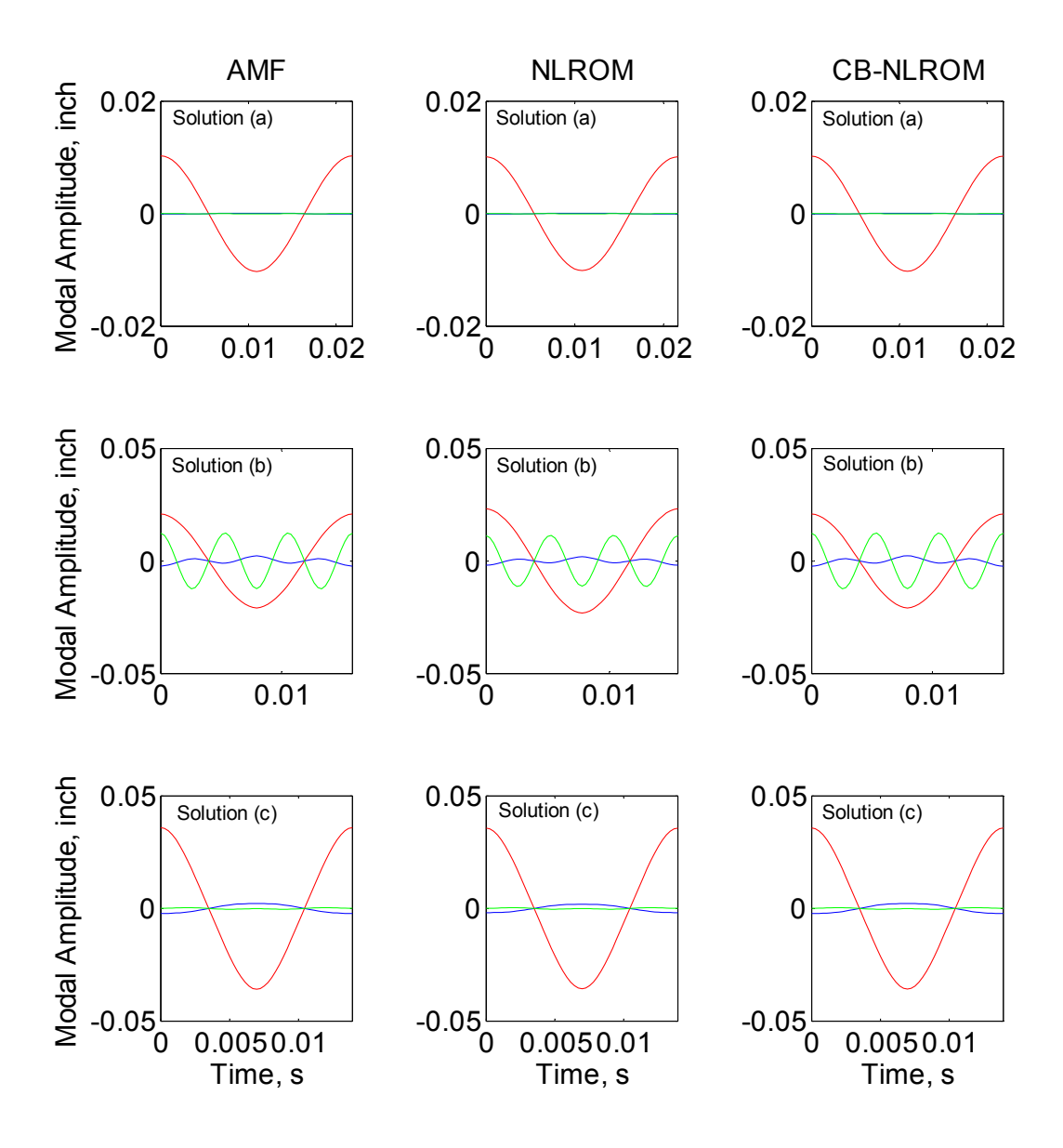


Figure 34. Time histories of the three responses marked on NNM 1 in Fig. 32, where the physical response was projected onto the unit displacement normalized modes of the assembly. The lines represent the three most dominant modes in these responses: (red) mode 1, (blue) mode 2, and (green) mode 3. Each model included subcomponent modes up to 4,000 Hz.

The time histories of solutions (a) and (c) along the backbone of NNM 1 reveal that the first linear mode dominates the response, and the results predicted by the assembled NLROMs and CB-NLROMs agree very well, although the frequency of the assembled NLROMs at point (a) was slightly higher. Solution (b) occurred along the 3:1 interaction with NNM 3, explaining

why the third bending mode oscillated at a frequency three times that of the fundamental frequency dominated by mode 1. The assembled CB-NLROMs and NLROMs predicted the response at this modal interaction very well in comparison to the AMF result, although there was slight disagreement with the frequency and maximum amplitudes predicted by the assembled NLROMs. Even at locations where the FEP seems to be in slight disagreement, the time history of the assembled NLROMs appeared to have good accuracy.

Figure 35 compares the maximum deformation shapes of the beam assembly (i.e. when all DOF have zero velocity) for each of the marked solutions in Fig. 32. The color bar for each deformation shows the log of the in-plane displacement magnitude at each node (note that the in-plane displacements were typically a thousand times smaller than the transverse). For the nonlinear modal substructuring methods, the membrane displacements had to be expanded using the expansion approach reviewed in Section 3.7 for the CB-NLROMs and NLROMs, since all of the subcomponent modes used to build the ROMs were bending modes.

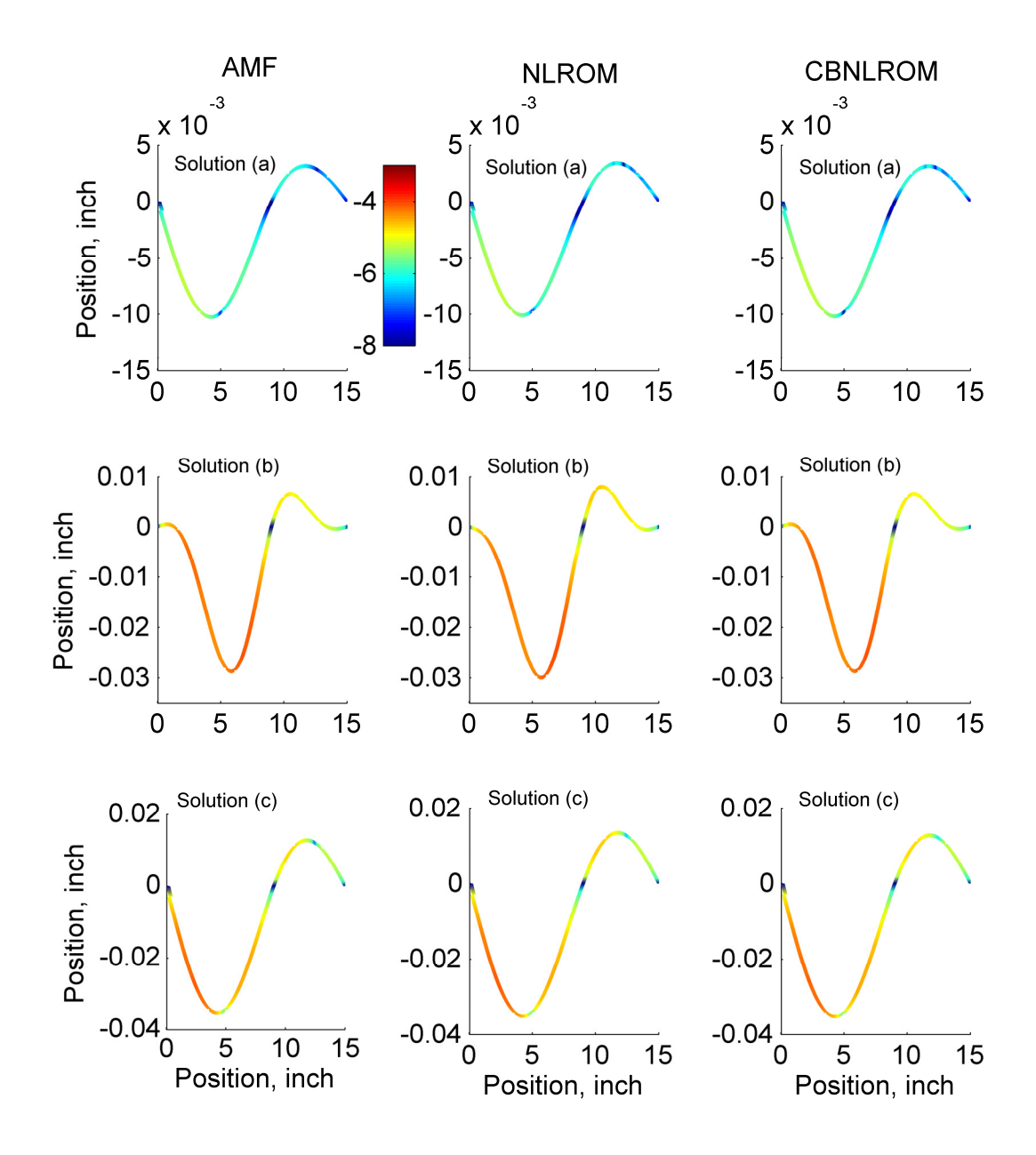


Figure 35. Maximum deformation shapes of NNM 1 in Fig. 32 using the (left column) AMF algorithm, (middle column) assembled NLROMs with free-interface modes up 4,000 Hz and (right column) assembled CB-NLROMs with fixed-interface modes up 4,000 Hz. The color bar gives the log of the absolute value of in-plane displacement at each node.

The deformation shapes and the magnitude of the in-plane displacements computed with both the NLROM and CB-NLROM approaches are in very good agreement with the NNMs computed with AMF. However, there was one notable difference between the NLROM and AMF predictions in solution (b) near the support on the left end of the beam. Both the shape and

the amount of axial stretching at this location are somewhat inaccurate and this could pose a problem if this was a region where failure was likely. The CB-NLROM method agreed very closely with AMF at most points, clearly showing its capability of predicting these in-plane displacements using the expansion approach, allowing for more accurate modeling of the stresses. A summary of the maximum percent error in the transverse and in-plane displacements is provided in Table 11.

Table 11. Maximum percent error of in-plane and transverse displacement of solutions in Fig. 35.

	Maximum % Er	ror CB-NLROMs	Maximum % Error NLROMs		
Solution Index	In-plane	Transverse	In-plane	Transverse	
(a)	2.34	0.137	2.76	0.535	
(b)	0.169	0.0405	2.18	2.91	
(c)	0.632	0.0450	1.39	0.428	

The CB-NLROM substructuring approach is capable of producing highly accurate predictions of the NNMs, even when including fixed-interface modes up to only 2.0 times the bandwidth of interest. While the assembled NLROMs built with free-interface modes were much less accurate, it also gave quite acceptable results for many of the NNMs over much of the frequency range of interest. In the next section, the CB-NLROM approach is demonstrated on another example where a modifying element was attached to one of the axial DOF of a 9-inch (229 mm) long beam.

# 6.2 Coupling Geometrically Nonlinear Beam to Axial Spring Element

The CB-NLROM modal substructuring technique is now demonstrated on a structural modification problem where a linear spring element was coupled to a geometrically nonlinear beam, as shown in Fig. 36. This example again represents a simplified model of an aircraft panel but instead with in-plane elastic boundary conditions. The geometrically nonlinear beam studied

here was 9 inches (229 mm) in length, with a cross section of 0.5 inches (12.7 mm) wide by 0.031 inches (0.787 mm) thick. The Abaqus® model was modeled with forty B31 Euler-Bernoulli beam elements, resulting in a total of 120 DOF. It was constructed of the same structural steel used in Section 6.1. The modifying axial spring attached to the left end had a stiffness of  $K_{ax} = 25,575$  lbf/inch (4,479 kN/m), which was half of the axial stiffness of the beam. The full FEA model of the geometrically nonlinear beam connected to the in-plane spring was also constructed in Abaqus® in order to compute the true NNMs of the assembly using the AMF algorithm.

Note that the assembly of NLROMs with free-interface modes would not work with this particular example, since the modal basis would only consist of bending type free-interface modes. For flat beams, the bending motions are completely decoupled from any axial motion, so these shapes have zero entries for each axial DOF. As a result, coupling an axial element through a bending only basis would not change the stiffness of the assembled equations. In theory, one could augment a set of axial modes to the basis, but this was not explored in this work. The CB-NLROM approach accounts for the in-plane kinematics explicitly with a single constraint mode, which is the shape resulting from a unit displacement applied to the axial DOF at the left end of the beam.

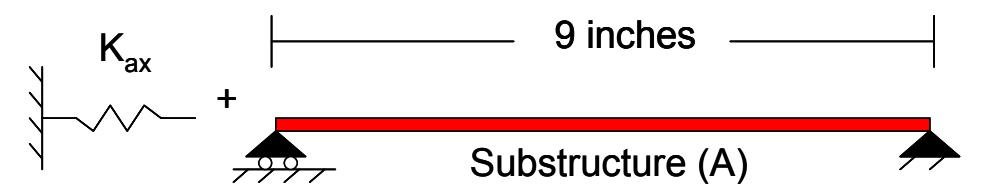


Figure 36. Schematic of the modification of a geometrically nonlinear beam with an axial spring element having a stiffness of  $K_{ax} = 25,575$  lbf/in (4,479 kN/m).

The fixed-interface modes for the beam in Fig. 36 were exactly those of the free-interface modes of the 9-inch (229 mm) simply supported beam studied in Section 6.1; the linear natural

frequencies of those modes were given in Table 9. The bandwidth of interest for the assembly of the nonlinear beam and spring is 500 Hz. Once again, two CB models were created including fixed-interface modes up to 1,000 Hz and 4,000 Hz. Substructuring was then used to assemble these models to the axial spring to obtain a model for the structure of interest. The first three NNMs were then computed from the modified CB-NLROMs and are shown below in Fig. 37. The CLD scaling factors from Section 3.5.2 for the loads in Eq. (69) were chosen such that a  $w_{\text{max},r}$  was set to 0.25 times the beam thickness for each fixed-interface mode (which were all bending), and 0.001 times the beam thickness for the one axial constraint mode. The in-plane nature of the constraint mode warrants a much smaller forcing amplitude compared to the fixed-interface bending modes. When the constraint mode was forced by a large amount, for example on the order of 0.25 times the beam thickness, the static solutions in the FEA software would not converge.

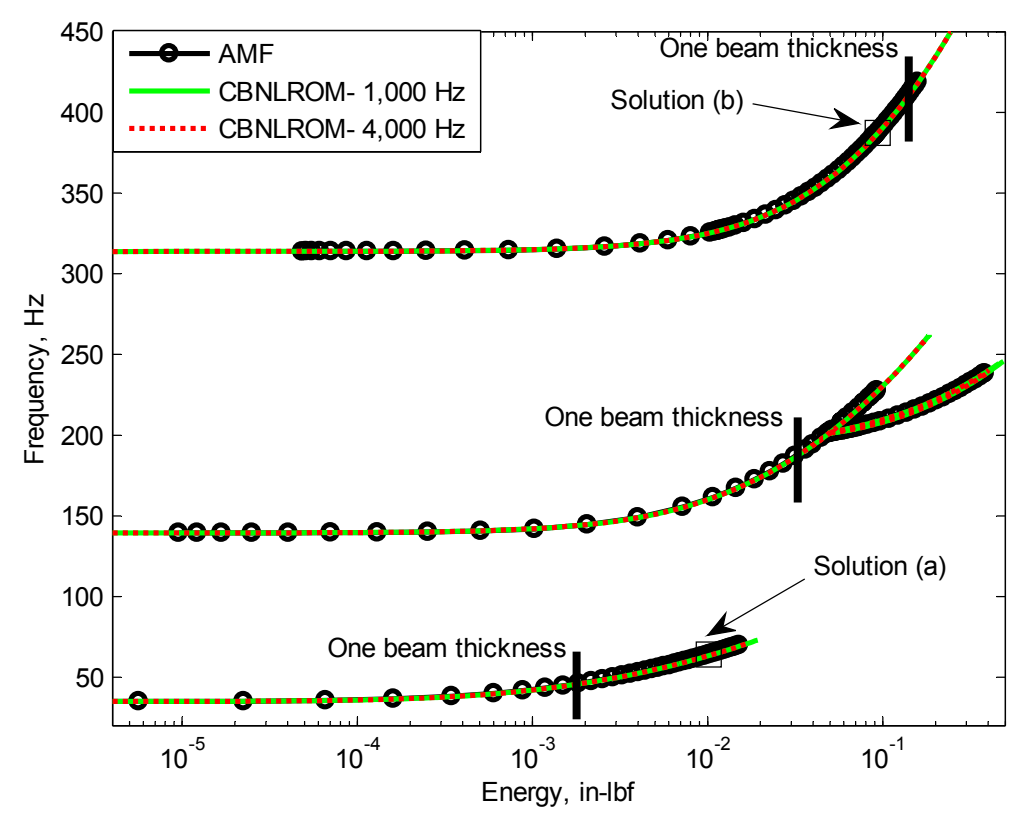


Figure 37. NNMs 1 through 3 of the modified nonlinear beam using (black circles) AMF on the full FEA model, and assembled CB-NLROMs with fixed-interface modes up to (green solid) 1,000 Hz, and (red dotted) 4,000 Hz.

The backbones of each NNM predicted by the two assembled CB-NLROMs agree very well with the AMF results, and these ROMs even captured the modal interaction along NNM 2, starting at 201 Hz, which was a 3:1 interaction with NNM 4. The agreement between the 1,000 Hz basis and 4,000 Hz basis showed that the CB-NLROMs sufficiently converged with subcomponent modes up to 2.0 times the frequency of interest so it was not necessary to include modes up to 8.0 times the frequency range of interest. Of course, other modal interactions could emerge along these NNMs, as seen with the results in the previous section, and would require a larger basis set to capture the higher order NNMs involved in the interaction. The maximum deformation shape of the beam for the solutions marked, (a) and (b), in Fig. 37 are shown in Fig. 38. The membrane displacements were again recovered using the expansion process reviewed in

Section 3.7 in order to accurately compare the in-plane motions predicted by the full order assembly.

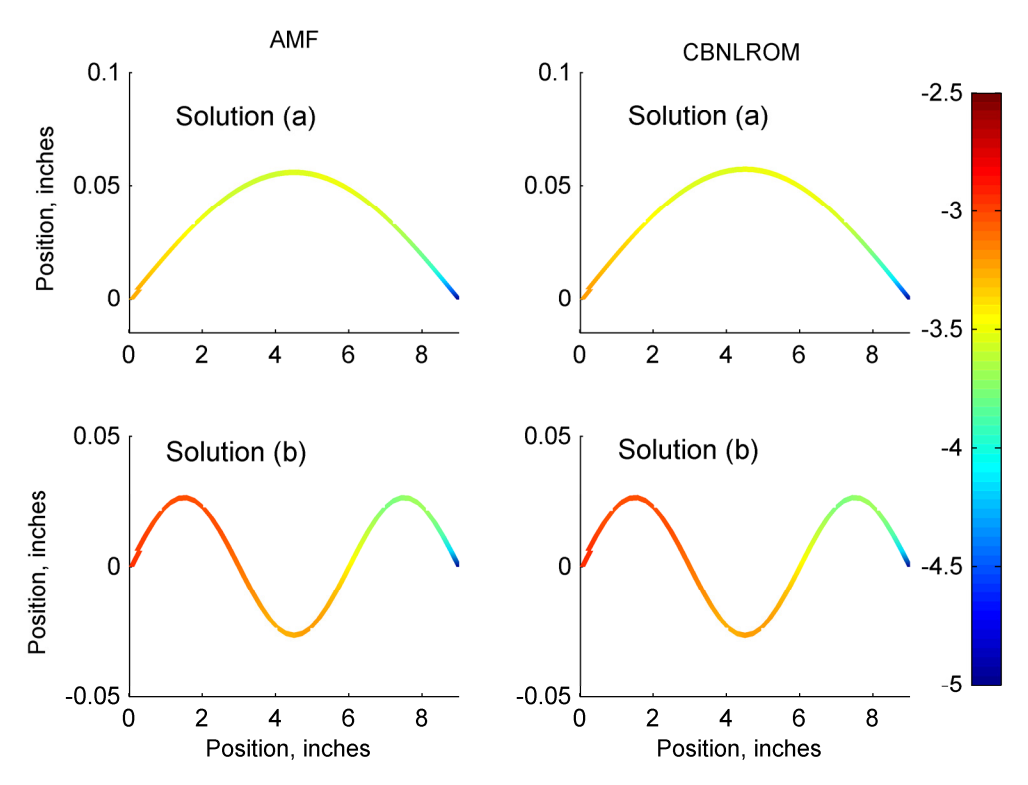


Figure 38. Maximum deformation shapes along NNM 1 and 3 in Fig. 37 using the (left column) AMF method and (right column) CB-NLROM substructuring with fixed-interface modes up 4,000 Hz. The color bar gives the log of the absolute value of in-plane displacement at each node.

The comparison between the two deformation shapes show excellent agreement between each other, both in the bending displacements and the magnitude of the in-plane displacements. The assembled CB-NLROMs can be used with confidence to accurately predict the strains and stresses of the subcomponents along the NNM branches. Each CB-NLROM was reduced to 6 DOF and 11 DOF, respectively, for the 1,000 Hz and 4,000 Hz basis, again providing an order of magnitude reduction from the full order model. To create these it was necessary to compute the nonlinear static response to 232 and 1562 load cases, which required about 3 minutes and 14 minutes, respectively, on the quad-core Intel i7 desktop computer used in this work. However, once the ROMs have been created they can be used together with springs of various stiffnesses to

very quickly evaluate how the axial boundary condition changes the NNMs or to compute the response of the structure. Hence, one could save many hours of computation by using the substructuring approach to perform design studies, even for this relatively simple structure.

## 6.3 Coupling Two Plates with Geometric Nonlinearity

The modal substructuring approach was applied to the assembly of two geometrically nonlinear, flat plates coupled to one another along a continuous interface. Each plate had simple supports at all nodes around the edges, and was modeled in Abaqus®. A schematic of these FEA models is shown in Fig. 39, where the two substructures were coupled at all x, y, and z rotational DOF along a shared edge. The 9 inch by 9 inch (229 mm by 229 mm) plate was modeled with 1,296 S4R shell elements (a 36×36 grid), while the 9 inch by 6 inch (229 mm by 152 mm) plate had a total of 864 S4R shell elements. Each plate had a uniform thickness of 0.031 inches (0.787 mm); thin-walled structures such as these can experience large deformations even while the materials remain within their linear elastic range. The material properties were those of structural steel having a Young's modulus of 29,700 ksi (204.8 GPa), shear modulus of 11,600 ksi (80 GPa), and mass density of 7.36·10<sup>-4</sup> lb-s<sup>2</sup>/in<sup>4</sup> (7,870 kg/m<sup>3</sup>). A total of 37 nodes were along the connection points, meaning there were 111 DOF at the interface.

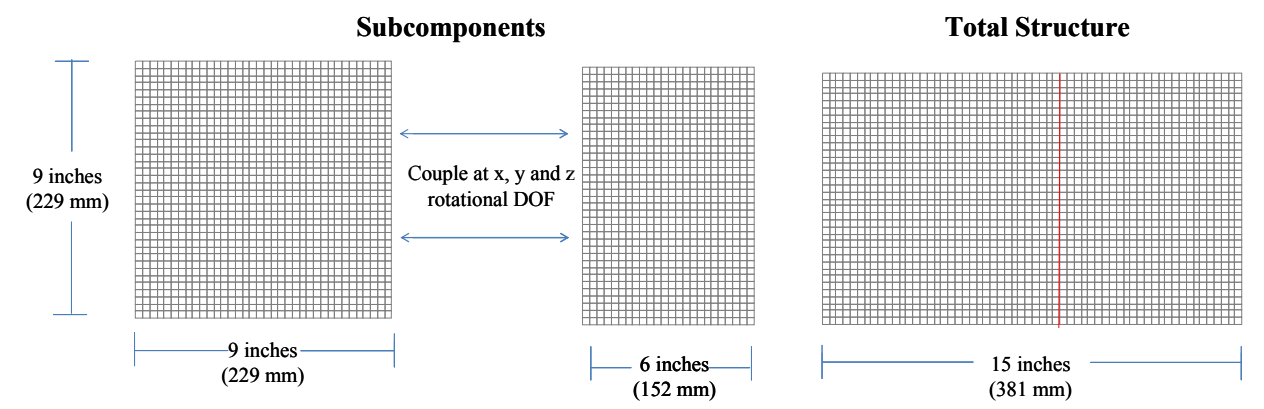


Figure 39. Schematic of coupling two geometrically nonlinear plates with simple supports at all edges. The FEA model of the total structure has simple supports at all edges and DOF along the red line where to two plates join.

In Section 6.3.1, the modal convergence of a *linear* substructuring approach (i.e. when  $\mathbf{f}_{NL}(\mathbf{x}) = \mathbf{0}$  for each subcomponent model in Eq. (63)) is performed using the fixed-interface modes with characteristic constraint modes in Eq. (62) and the Craig-Bampton modal basis in Eq. (58). In Section 6.3.2, the *nonlinear* substructuring approach is demonstrated on the same example problem, except that  $\mathbf{f}_{NL}(\mathbf{x}) \neq \mathbf{0}$ . The nonlinear subcomponent ROMs with fixed-interface and characteristic constraint (CC) modes are referred as CC-NLROMs. Note that the interface between the plates had 111 rotational DOF/constraint modes, therefore the CB basis would require far to many static load cases to fit a nonlinear ROM with Implicit Condensation and Expansion, so this approach was not pursued on this problem.

## 6.3.1 Linear Substructuring

The linear FEA models of the plates were first used to determine how many characteristic constraint modes would be needed for the *linear* substructuring problem, which provides insight into the basis selection for the nonlinear substructuring problem. Table 12 gives the natural frequencies and mode shapes of the fixed-interface and characteristic constraint modes for each subcomponent model. The exact modes of the full FEA model of the assembly are shown in the

far right column to provide a reference solution against which to compare the substructuring results that will be presented later.

Table 12. Linear subcomponent modes used with the CC mode reduction.

Mode Number	Fixed-interface modes: 9"x9" plate	Fixed-interface modes: 9"x6" plate	Characteristic constraint modes	Truth modes of total structure	
1	87.1 Hz	156.8 Hz	140.2 Hz	78.4 Hz	
2	190.6 Hz	254.4 Hz	420.9 Hz	135.1 Hz	
3	216.6 Hz	430.1 Hz	930.7 Hz	185.7 Hz	
4	317.7 Hz	449.5 Hz	1660 Hz	203.0 Hz	
5	371.4 Hz	547.0 Hz	2610 Hz	239.5 Hz	
6	420.3 Hz	685.2 Hz	3785 Hz	306.4 Hz	
7	494.6 Hz	717.4 Hz	5196 Hz	365.7 Hz	
8	521.5 Hz	915.3 Hz	6853 Hz	368.2 Hz	
9	630.0 Hz	965.6 Hz	8769 Hz	419.7 Hz	
10	696.1 Hz	1014 Hz	10.96 kHz	434.1 Hz	
11	700.6 Hz	1021 Hz	13.44 kHz	474.4 Hz	
12	749.8 Hz	000 000 000 1183 Hz	16.24 kHz	485.5 Hz	

For this example, the frequency range of interest was 0-500 Hz, so the first 12 modes of the total structure in Table 12 were taken as target modes. A typical rule of thumb for linear substructuring is to include subcomponent modes up to 1.5 to 2.0 times this range. Even though the characteristic constraint modes have associated eigenfrequencies from the secondary modal analysis in Eq. (61) in Section 5.2.3, this rule of thumb is not well established for these modes. When deciding which CC modes to retain in the basis, it was determined that these should be selected such that the accuracy of the CB substructuring approach was preserved. This was done by computing the maximum percent frequency errors between the modes predicted by the assembled CB ROMs, and those from the assembly of truncated CC ROMs. This is demonstrated on the linear plates with subcomponent fixed-interface modes up to 750 Hz, 1,000 Hz and 1,500 Hz, or 1.5, 2.0 and 3.0 times the frequency band of interest, respectively. The maximum of the percent frequency error between all modes predicted by the assembled CC ROMs and the assembled CB ROMs is shown in Fig. 40 as CC modes were added to the basis. As the number of CC modes increases the error precipitously falls down below 0.01%, hence for each case the number of CC modes included was chosen such that the maximum percent error in the linear frequencies fell below 0.01 %. Returning to Table 12, one can see that the maximum frequency of the CC modes that were included is well beyond the frequency range of interest in each case.

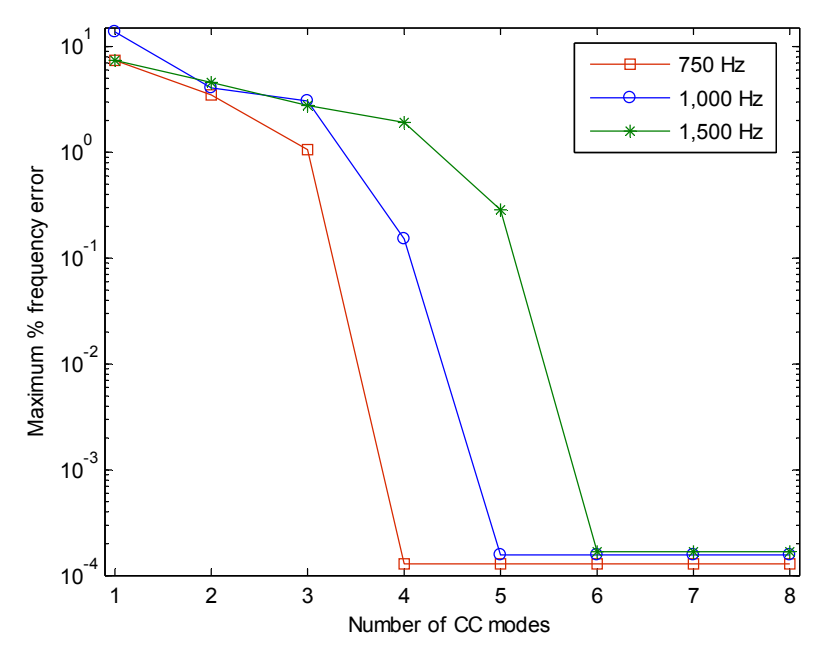


Figure 40. Maximum percent error of the assembly modes predicted by the CB ROMs and the CC ROMs as the number of CC modes were increased in the basis. The lines represent the number of fixed-interface modes included in each ROM: up to (red squares) 750 Hz, (blue circles) 1,000 Hz and (green asterisks) 1,500 Hz.

Hence, four, five and six CC modes were included in the CC ROM basis for the cases where the fixed-interface modes were included up to 750 Hz, 1,000 Hz, and 1,500 Hz, respectively. Even after truncating the CC modes in this manner, the resulting model still provides the same predictive accuracy as the full assembled CB ROMs, which have 111 constraint modes. The total number of DOF in each of these reduced order models was then 23, 30, and 44 DOF. The percent frequency errors in Table 13 compare the predicted modes with those of the full FEA model of the total structure, providing insight into the accuracy of these assembled CC ROMs (and ultimately the CB substructuring approach). The lowest order ROM predicted the assembly modes up to 500 Hz very well including linear modes up to only 1.5 times the frequency band of interest; the largest frequency error was 0.39 % in the 11<sup>th</sup> mode. Additional modes in the basis lowered the frequency error further, as expected.

Table 13. Percent frequency error of the first 12 assembly modes predicted by the assembled CC ROMs and the full FEA model of the total structure.

Total Structure Mode Number	% Error with 4 CC modes and up to 750 Hz fixed-interface modes	% Error with 5 CC modes and up to 1,000 Hz fixed- interface modes	% Error with 6 CC modes and up to 1,500 Hz fixed- interface modes
Wiode Number			
1	$4.4 \cdot 10^{-4}$	$1.7 \cdot 10^{-4}$	$6.7 \cdot 10^{-5}$
2	$7.2 \cdot 10^{-3}$	$4.8 \cdot 10^{-3}$	$4.0 \cdot 10^{-3}$
3	$1.2 \cdot 10^{-3}$	$-1.8 \cdot 10^{-4}$	$-1.3 \cdot 10^{-3}$
4	$7.4 \cdot 10^{-3}$	$4.0 \cdot 10^{-3}$	$2.8 \cdot 10^{-3}$
5	$1.4 \cdot 10^{-2}$	$6.8 \cdot 10^{-3}$	$8.5 \cdot 10^{-4}$
6	$1.9 \cdot 10^{-2}$	$9.8 \cdot 10^{-3}$	$2.3 \cdot 10^{-3}$
7	0.16	$6.2 \cdot 10^{-2}$	$2.7 \cdot 10^{-2}$
8	$5.7 \cdot 10^{-3}$	$3.8 \cdot 10^{-3}$	$1.7 \cdot 10^{-3}$
9	$2.0 \cdot 10^{-2}$	$1.1 \cdot 10^{-2}$	$2.1 \cdot 10^{-3}$
10	$1.5 \cdot 10^{-2}$	$5.7 \cdot 10^{-3}$	$2.4 \cdot 10^{-3}$
11	0.39	0.18	$3.3 \cdot 10^{-2}$
12	$2.4 \cdot 10^{-2}$	$1.3 \cdot 10^{-2}$	$3.1 \cdot 10^{-3}$

For a linear system, the CC ROMs with modes up to 750 Hz and 4 CC modes would be sufficient for response prediction. In the next subsection, all of these bases are used to compare the nonlinear substructuring approach since additional modes might be necessary to capture the dynamics of the nonlinear assembly. The same modal bases are used when generating the CC-NLROMs of the geometrically nonlinear plates in Fig. 39, and the convergence of the nonlinear substructuring results is evaluated using nonlinear normal modes.

## **6.3.2** Nonlinear Substructuring

The CC-NLROMs of the two plate models were generated with the same set of fixed-interface and characteristic constraint modes used in the linear analysis (fixed-interface modes up to 750 Hz, 1,000 Hz and 1,500 Hz with 4, 5 and 6 CC modes, respectively). The force amplitudes  $\hat{f}$  for the static loads in Eq. (69) are typically chosen such that when a single-mode force (e.g.  $\mathbf{F}_r = \mathbf{K}\mathbf{T}_{CC,r}\hat{f}_r$ ) is applied to the linear FEA model, the maximum displacement is on the order of one thickness. For the CC-NLROMs generated here, each mode in the  $\mathbf{T}_{CC}$  basis in Eq. (62) was scaled to force the linear system to a maximum displacement of 0.25 times the

thickness, or 7.75·10<sup>-3</sup> inches (0.197 mm). The details on the scaling are found in Section 3.5.2. Once the coefficients in Eq. (68) were identified, the CC-NLROMs were coupled and the equations of motion in Eq. (78) were used to compute the NNMs using the pseudo-arclength continuation algorithm in [49]. The first three NNMs of the assembled CC-NLROMs are compared with the NNMs of the full FEA model of the total structure in Fig. 41. The full order model NNMs were computed using the applied modal force (AMF) algorithm Chapter 2, but these curves were quite expensive since the model had >10,000 DOF. These provide a few reference solutions along the backbone to help validate the accuracy and convergence of the assembled CC-NLROMs, analogous to the comparison of linear normal modes in the previous subsection.

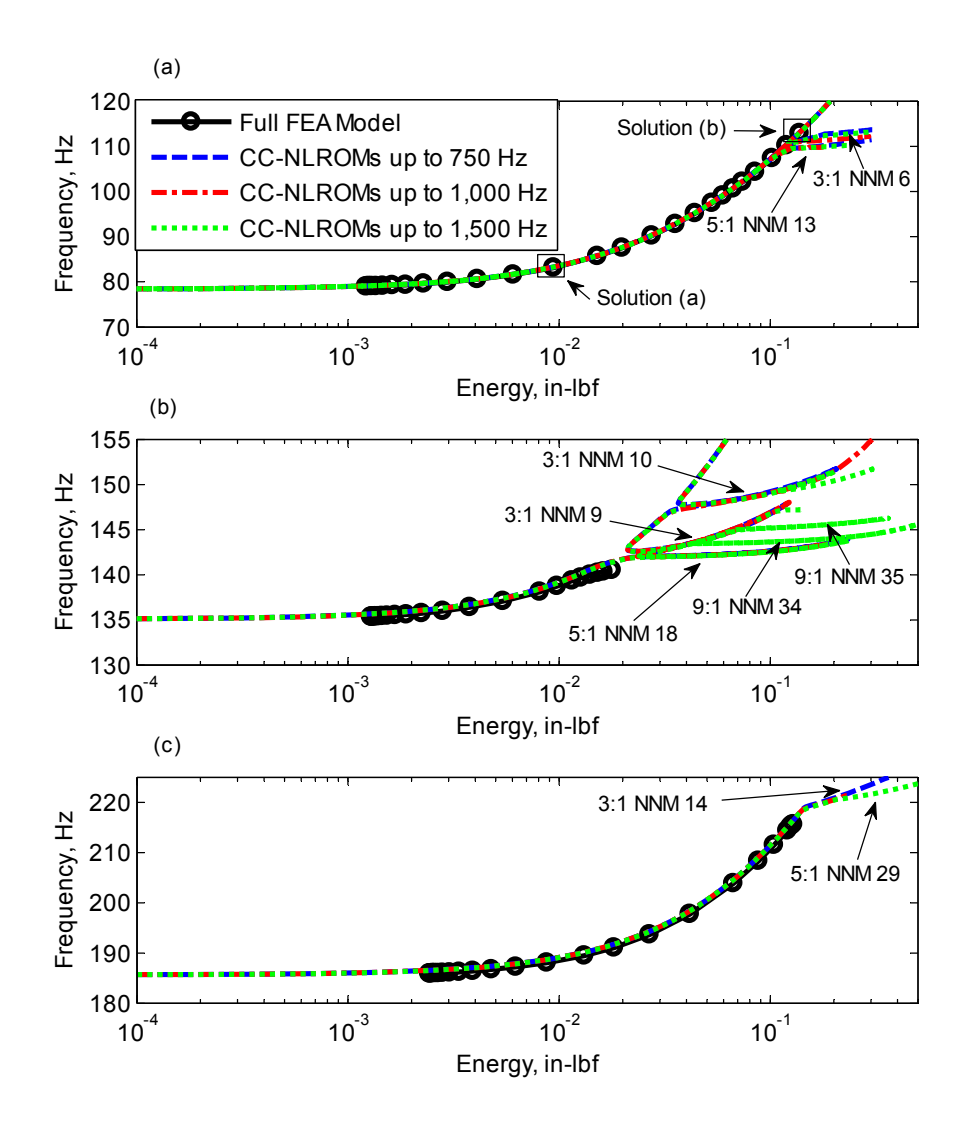


Figure 41. Frequency-energy plots of (a) NNM 1, (b) NNM 2 and (c) NNM 3 for the assembly of two plates in Fig. 39. Each curve was computed from the (black dotted) full order model of the total structure, assembled CC-NLROMs with fixed-interface modes up to (blue dashed) 750 Hz, (red dash-dotted) 1,000 Hz, and (green dotted) 1,500 Hz.

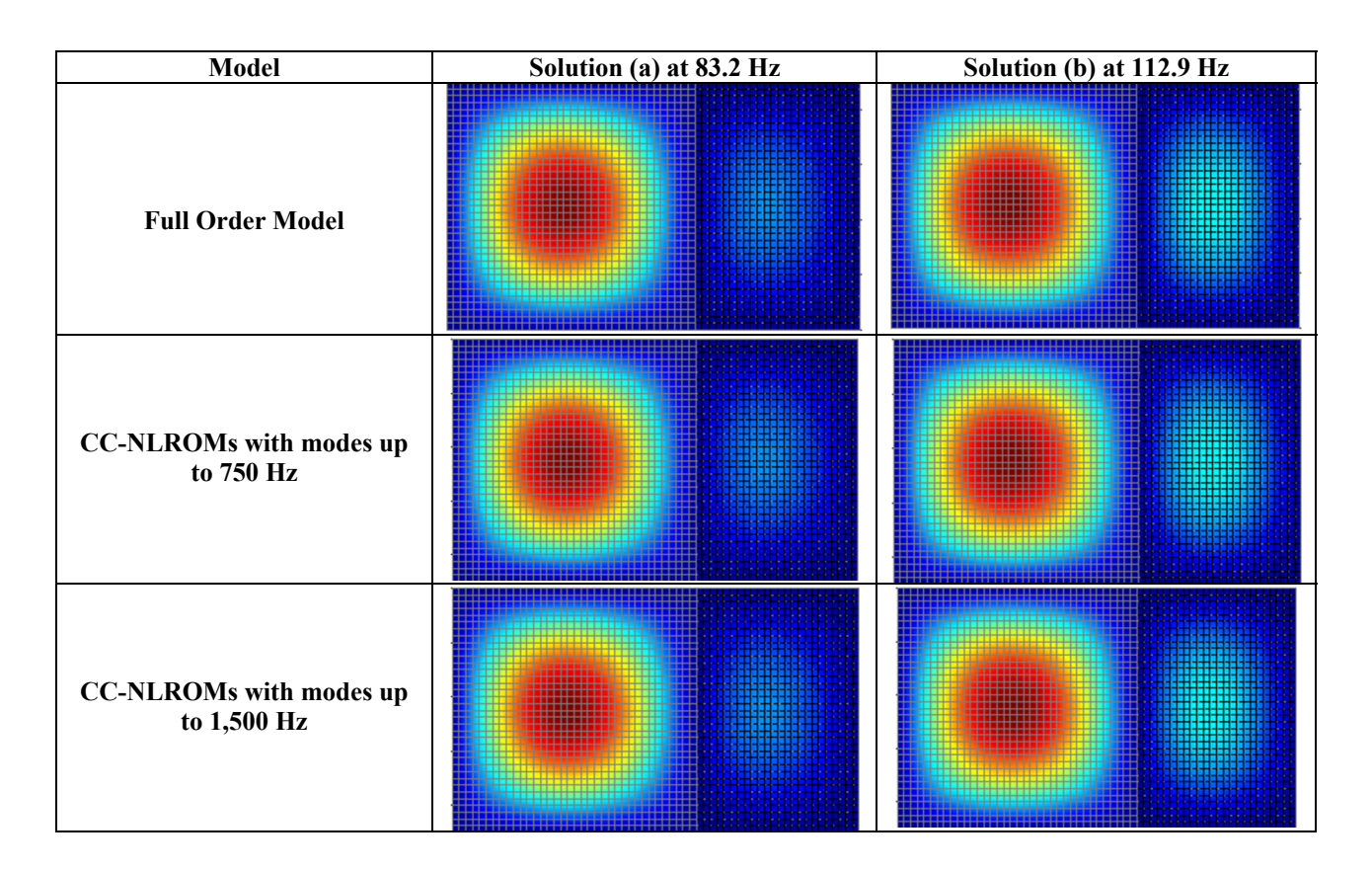
The first three NNMs of the plate assembly exhibit hardening nonlinear behavior as indicated by the increase in frequency with an increase in response energy; this is due to the membrane-bending coupling induced by large bending deformations. Each NNM branch in Fig. 41 started at a linear mode solution at low energy (or response amplitude), but increasing displacement amplitudes exercised the nonlinear restoring force in the equations of motion,

changing the dynamic response. There are two notable features of the NNM branches in Fig. 41, namely the backbone, which occurs at the lowest possible energy for a given frequency, and the tongues, which emanate from the backbone. Each tongue corresponds to a modal interaction with other NNMs of the model that oscillate at a strict integer ratio of frequencies (see [25, 38] for further discussion of these solutions). AMF was run in a manner that caused all of its solutions (black circles) to remain along the main backbone; further computations would be needed to capture these modal interactions.

The main backbones predicted by all of the assembled CC-NLROMs agree very well with those of the full order model, suggesting that even the lowest order model (with fixedinterface modes up to 750 Hz and 4 CC modes) could be used for accurate response prediction. Adding fixed-interface and CC modes to the basis did slightly affect the modal interactions predicted by the ROMs. For example, in Fig. 41c the modal interaction near 220 Hz started as a 3:1 interaction with NNM 14 (i.e. mode 14 oscillates at a frequency 3 times the fundamental frequency of ~220 Hz). The 750 Hz assembly of CC-NLROMs (blue dashed) continued along this tongue towards higher energies, whereas the 1,500 Hz assembly (green dotted) continued along a new tongue corresponding to a 5:1 interaction with NNM 29. Since the 750 Hz model only had 23 DOF it would not be able to capture NNM 29, meaning that higher order ROMs were needed to capture this tongue. Similar observations are made in Fig. 41b with the tongues emanating from the 3:1 interaction with NNM 9. The 1,500 Hz assembly of CC-NLROMs captured the 9:1 interactions with NNMs 34 and 35, both of which were not captured with the lower order models. An infinite number of these interactions can occur along the backbone of the NNM, and it is hard to determine the effect of these solutions on the accuracy of the ROMs and their intended use.

The higher order NNMs 4 through 10 computed with the 750 Hz and 1,500 Hz models were all in agreement along the backbones, however NNM 11 was the first to show a slight offset between the two models (these results are not shown for brevity). The nonlinear modal convergence study helps identify when a sufficient number of modes have been included in the basis for the frequency bandwidth of interest. To further compare each model, the maximum out-of-plane displacements (i.e. when the velocity is zero) are shown in Table 14 for the solutions marked (a) and (b) in Fig. 41a, showing how the deformation shapes evolve along the backbone of NNM 1. The deformations predicted by the models agree very well with one another, as expected from the agreement with the frequency-energy plots shown earlier. The deformation shapes changed as the energy increased along the backbone showing that more vibration energy was in the smaller 9 inch by 6 inch (229 mm by 152 mm) plate at solution (b) as compared with solution (a), which was taken near the linear regime. The shapes all agree very well suggesting that either CC-NLROM would adequately capture the response of the assembly near these two points.

Table 14. Table comparing the out-of-plane maximum deformation shapes of solutions (a) and (b) marked along NNM 1 in Fig. 41.



The NNMs computed from the undamped equations of motion in Eq. (78) have an intimate connection to the forced steady state response of the damped system, as these undamped NNMs form the backbone to the forced response curves as discussed in Section 1.2. Resonance of the damped response occurs in the neighborhood of the NNM when the damping forces exactly cancel out the harmonic forcing function. Therefore, by accurately capturing the NNMs, the damped forced response near resonance, which is when the structure is at its greatest risk of failure, will also be accurate. Hence, the results presented above suggest that either of the CC-NLROMs would accurately capture the forced response of the panel near resonance.

During the course of this research, it was questioned whether it was truly important to capture the nonlinear stiffness of the characteristic constraint modes and their nonlinear

couplings to the other modes. It was hypothesized that these terms might be negligible, in which case one could simply create a ROM from the fixed-interface structure, augment it with traditional, linear CC modes, and compute the response of the assembly. To test this hypothesis, a separate modeling strategy was explored during this research where each nonlinear subcomponent ROM was estimated fixing all of the boundary DOF in the FEA model in Eq. (63), computing the nonlinear modal model from it using only the fixed-interface modes, and appending the linear CC modes. These subcomponent models are referred to here as fixed-interface NLROMs (FI-NLROMs), and were assembled in the same way as the CC-NLROMs in Section 5.4. This approach was motivated by the potential computational savings obtained by only requiring static force permutations in Eq. (69) in the shapes of the fixed-interface modes, and not the static constraint modes. For example, for the ROMs of the 9 by 9 inch (229 mm by 229 mm) plate with fixed-interface modes up to 1,500 Hz, this would require only 15,226 load cases instead of 30,914 for the CC-NLROM. Unfortunately, this approach was found to produce an inaccurate estimate of the first NNM, as shown in Fig. 42.

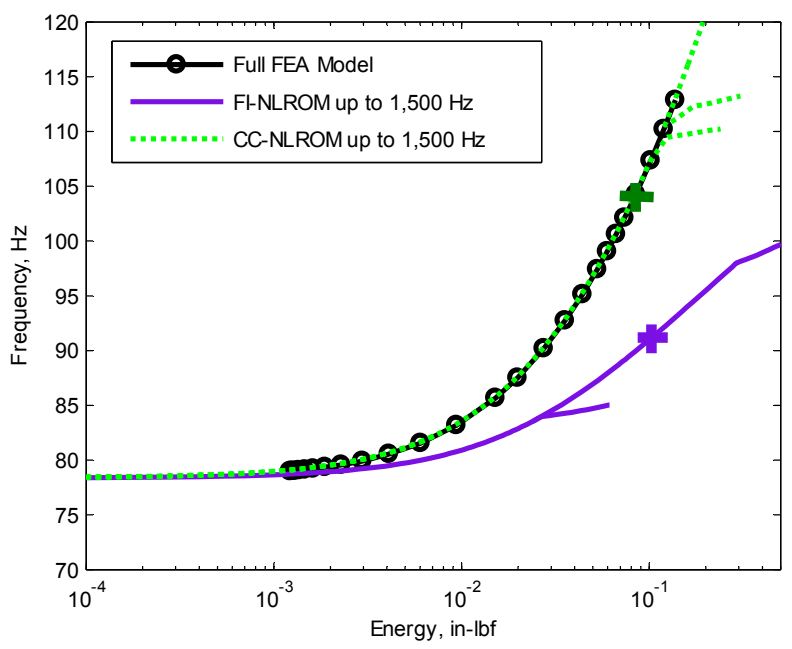


Figure 42. Frequency-energy plots of NNM 1 for the assembly of two plates. Each curve was computed from (black dotted) full order model of the total structure, (green dotted) assembled CC-NLROMs and (purple solid) assembled FI-NLROMs with fixed-interface modes up to 1,500 Hz.

The NNM predicted by the assembled FI-NLROMs with fixed-interface modes up to 1,500 Hz (and 6 linear CC modes) clearly disagrees with that predicted by the assembled CC-NLROMs with the same basis and the reference solutions from the full FEA model. In order to quantify the importance of these results, the energy balance technique in [38, 55, 56] was used to compute the force amplitude required to excite resonance of the damped system with a single-point harmonic forcing function. In this calculation, each mode of the FI-NLROMs and CC-NLROMs was assumed to have 0.1% modal damping, which is near the damping level observed experimentally for similar structures [19]. A point force was applied at the midpoint of the 9 inch by 9 inch (229 mm by 229 mm) plate in the out-of-plane direction. This analysis predicted that a point force with an amplitude of 9.6·10<sup>-3</sup> lbf (4.3·10<sup>-2</sup> N) would excite resonance of the assembled FI-NLROMs at 90 Hz, resulting in a peak displacement of 0.0328 inches (0.833 mm). The calculations with the more accurate ROM predicted that this force amplitude would actually

produce resonance at a significantly higher frequency (104.3 Hz) with a smaller peak displacement of 0.0295 inches (0.749 mm). The corresponding locations are marked with an (+) in Fig. 42. The accuracy of the modeling strategy and its resulting NNMs have a strong connection to the accuracy the various forced response predictions.

The AMF algorithm took on the order of 2 to 3 days to compute each NNM of the 12,861 DOF full order model of the assembly using a desktop computer with an Intel® Core i7 CPU and 8 GB of RAM, so only a few "truth" solutions were available for comparison throughout this section. Each NNM from the CC-NLROM substructuring approach took anywhere from 15-30 minutes to compute, depending on the parameters used in the stepsize controller and the size of the ROM. The upfront cost to run the static analyses for each CC-NLROM is summarized in Table 15, along with the cost estimate if all 111 static constraint modes were used in the basis without any interface reduction (note that this would be the CB-NLROM approach used in Sections 6.1 and 6.2). For example, creating the CC-NLROMs with fixed-interface modes up to 1,500 Hz and 6 CC modes would require a total of 42,436 static load cases, taking 46 hours on the desktop computed mentioned earlier, and the equivalent CB-NLROMs would require 5,808,336 static loads and 248 days of CPU time. The interface reduction reduced the number of static loads required by ICE approach to identify each subcomponent model, making the modal substructuring approach feasible. For reference, creating an NLROM of the full plate assembly using the approach in Chapter 3 with linear modes up to 500 Hz and 1,500 Hz (a total of 12 and 41 modal DOF, respectively) would require 2,048 static loads (4 hours) and 88,642 static loads (173 hours), respectively. In practice, this model would likely need more than modes up to 500 Hz to accurately capture all the NNMs in the 0-500 Hz frequency range, however this serves as the lower bound to the cost estimate.

Table 15. Computational cost associated with the identification of nonlinear subcomponent models using ICE.

	Fixed-interface modes up to 750 Hz		Fixed-interface modes up to 1,000 Hz		Fixed-interface modes up to 1,500 Hz	
Model	CB-NLROM	CC-NLROM	CB-NLROM	CC-NLROM	CB-NLROM	CC-NLROM
	·123 DOF	·16 DOF	·127 DOF	·21 DOF	·134 DOF	·29 DOF
9 inch by 9	.2,451,226	·4,992 loads	.2,699,258	·11,522 loads	·3,172,584	·30,914 loads
inch plate	loads	·6 hours	loads	·14 hours	loads	·37 hours
	·122 days		·134 days		·158 days	
	·118 DOF	·11 DOF	·120 DOF	·14 DOF	·126 DOF	·21 DOF
9 inch by 6	.2,163,176	·1,562 loads	.2,275,520	·3,304 loads	.2,635,752	·11,522 loads
inch plate	loads	·1 hour	loads	·3 hours	loads	·9 hours
	·74 days		·78 days		·90 days	

### 6.4 Summary

This chapter presented three case studies demonstrating the nonlinear modal substructuring approaches in Chapter 5 on geometrically nonlinear finite element models. The results on the two geometrically nonlinear beam examples showed that the assembled CB-NLROMs (built with fixed-interface and constraint modes) reproduced the NNMs of interest very well when the basis included modes up to twice the frequency band of interest. For the NLROM method (using free-interface modes), there were still noticeable errors with modes up to 8.0 times the bandwidth, but overall the results agreed well with the truth model and may have been adequate for many purposes. For applications with softer connections, the free-interface basis would be expected to perform better. An advantage of the CB-NLROM method is that the CB basis can readily include axial kinematics, so one can readily perform design studies to assess the effect of the in-plane stiffness of the mounting structure. One foreseeable pitfall to the CB modal basis, however, is the fact that it could require a very large number of constraint modes to capture the kinematics of a continuous interface with many interface DOF, hence motivating the use of characteristic constraint modes.

The substructuring approach with CC-NLROMs (built with fixed-interface and characteristic constraint modes) was demonstrated in Section 6.3 by coupling two thin plates

with geometric nonlinearity. The NNMs were computed from the assembled CC-NLROMs generated with an increasing number of fixed-interface and characteristic constraint modes. The results showed excellent agreement along the backbone predicted by each ROM and the full order model. The only difference with the higher order ROMs were the modal interactions along the NNM, which are associated with interactions involving higher order modes. The results showed how the maximum deformation shapes evolved along the backbone of NNM 1, providing valuable insight into the evolution of the stress fields experienced by the system at various resonant conditions. The interface reduction with characteristic constraint modes drastically reduced the number of DOF describing the interface, hence lowering the upfront computational cost associated with the identification of the nonlinear stiffness coefficients in the subcomponent models. The assembly of CC-NLROMs was orders of magnitude smaller compared to the full order finite element model yet maintain acceptable accuracy.

A substructuring approach has the advantage of dealing with several small, simpler subcomponent models compared to one large complicated model. Often during the development and analysis of structural components, most design changes occur at a subcomponent level, therefore a modal substructuring approach makes it easier to update one subcomponent model rather than the entire model of the assembly. This work has relied exclusively on the NNMs to judge the quality of the assembled ROMs. The author and his colleagues advocate the use of this approach because the NNMs provide a load-independent characterization of the nonlinear model and yet they have been shown to be intimately connected to the response of the structure to various types of loading [25, 35, 40, 41]. For all of the cases studied here, the true NNMs were calculated by the AMF algorithm in Chapter 2, but this algorithm becomes quite expensive for large finite element models. Fortunately, the results shown here suggest that the NNMs tend to

converge as additional modes are added to the subcomponent basis, so the NNMs could be used as a convergence metric without a comparison to the truth model.

### 7 Conclusions

The dynamic reduction strategies used throughout this work have shown to be very sensitive to a number of modeling decisions, such as the number and type of modes in the basis, and the scaling amplitudes of the static loads used to fit the nonlinear stiffness coefficients. In this dissertation, a novel approach to evaluate the convergence of these geometrically nonlinear reduced order models was developed based on their undamped nonlinear normal modes. This work also proposed a modal substructuring framework to create a reduced order model of a large, complicated structure by first dividing it into smaller subcomponent models, building ROMs of each using the Implicit Condensation and Expansion approach, and assembling these by satisfying compatibility and force equilibrium.

The accuracy of candidate ROMs was evaluated in Chapter 4 by comparing the NNMs from the reduced equations to those computed from the full order FEA model using the Applied Modal Force (AMF) algorithm in Chapter 2. Two geometrically nonlinear systems were studied in Chapter 4 with the Implicit Condensation and Expansion and Enforced Displacement approaches, and valuable insight was revealed about the sensitivities of the scaling methods and mode selection. The reference NNMs from the full order models provided confirmation that the ROMs were converging to the true solution, giving confidence in the ability of the NNM to provide a reliable convergence metric. In the applications of interest (e.g. complicated FEA models with many DOF), the solution of the full order model will be too expensive to compute, but the case studies presented here provide guidance regarding the load amplitudes to try and illustrate how sensitive the results can be to load cases and modal basis selection. A third case study on a simply supported beam with an impacting spring was presented in Chapter 4 to

demonstrate the convergence metric on a system with non-smooth nonlinearities where the NNMs from the full order model were not available. The ROMs were generated with an increasing number of linear vibrations modes and a single discontinuous basis function [113], and the NNMs appeared to converge along the backbone but not along the internal resonances. The importance of the internal resonances was evaluated by comparing the response of the ROMs to the full order model for both an impulsive load and a random input. These results suggest that a ROM that accurately captured the backbone (and also included a similar density of internal resonances) would be adequate to predict the random and transient response, although no formal proof was developed in this work.

A nonlinear modal substructuring approach for geometrically nonlinear structures was developed in Chapter 5 by first creating subcomponent ROMs with the Implicit Condensation and Expansion method [19, 103] using either free-interface modes, fixed-interface plus constraint modes, or fixed-interface plus characteristic constraint modes [82]. Once the subcomponent ROMs were identified, they were assembled to provide a reduced order model of the global assembly that accounts for geometric nonlinearity. The results in Chapter 6 evaluated the accuracy of the nonlinear substructuring approaches with three case studies involving geometrically nonlinear FEA models. The free-interface and fixed-interface plus constraint mode basis was used to couple two nonlinear beams at a shared rotational DOF, revealing that the latter basis had better convergence properties. One advantage of the fixed-interface plus constraint mode basis was that it readily included axial kinematics, so it was demonstrated on a structural modification problem where a linear spring element was coupled to a geometrically nonlinear beam at an axial DOF. This approach allows one to modify the in-plane elastic boundary conditions and assess the effect of the in-plane stiffness on the mounting structure. A

final case study involving two geometrically nonlinear plates demonstrated that the size of the interface could be reduced by more than an order of magnitude using characteristic constraint modes. For the subcomponent models with 6 CC modes and fixed-interface modes up to 1,500 Hz, this reduced the number of static load cases down to 42,436 (or 46 hours of CPU time) from the 5,808,336 (248 days) that would have been needed without the interface reduction. An equivalent ROM created from the full FEA model of the assembly with modes up to 500 Hz and 1,500 Hz would have required 2,048 static load permutations of 12 modes (4 hours) and 88,642 static load permutations of 41 modes (173 hours), respectively. Creating a reduced order model with substructuring allows one to build ROMs of simpler subcomponent models that could potentially require fewer modes than the ROM approach on the full order model (Chapter 3), however this will strongly depend on the number of basis vectors needed to accurately capture the response.

The NNMs serve as a signature of the equations of motion that clearly and concisely describe the dynamics of the system, and provide a metric that is independent of external loads making it ideal for comparisons between a set of candidate ROMs of geometrically nonlinear FEA models. This dissertation showed that even if the true NNM solutions from the AMF algorithm from Chapter 2 were not available, the convergence of the NNMs would still provide a powerful comparison metric. One advantage to the NNM is that they provide valuable insight into the dynamics of the system and to the response to various load environments. For example, the intimate connection between the NNMs and the harmonically forced, damped response suggest that a ROM that is able to accurately predict the NNMs can also predict the resonance of the lightly damped system [25, 34-39, 55, 56], a situation where the structure will be most likely to fail. The ROMs of a geometrically nonlinear FEA model can be created either directly from

the FEA model of the assembled structure, or from an assembly of subcomponent ROMs. Either way, the NNMs help to evaluate the accuracy and convergence of the reduce equations to give the user confidence in the ability of the ROM to make efficient and accurate response predictions.

### 8 Future Work

### 8.1 Substructuring of Thermal-Structural Models

The modal substructuring approach developed in this dissertation only applies to the nonlinear structural model of the system of interest. In extreme load environments during high speed flight [21, 22], coupled structural-thermal interactions may strongly influence the nonlinear response and the reduced order model of these structures would need to capture the appropriate physics (e.g. see [119, 120]). The substructuring framework could be extended to assemble a set of thermal-structural reduced order models with relatively little variation from the approach developed in this dissertation. The coupled ROMs would provide more accurate response predictions if aerothermal effects are expected to influence the response of the global assembly of interest (e.g. full order model of a high speed aircraft), allowing for more computationally efficient time simulations of models involving coupled physics.

# 8.2 Model Updating

This work demonstrated that nonlinear normal modes are valuable as a convergence metric, since they provide insight into the accuracy of the reduced order models. Recent studies have used undamped NNMs as an amplitude dependent metric to make comparisons between experimentally identified NNMs and those predicted by a numerical/analytical model [109, 110]. The nonlinear modal parameters (e.g. energy dependent frequencies, deformation shapes, etc..) could be used to define an optimization function, or cost function, for a model updating scheme. Kuether and Allen [121] recently developed an algorithm based on numerical integration and shooting that validates the NNMs from reduced order models by using the initial conditions from the ROM as a initial guess to the shooting function in the AMF algorithm in Chapter 2. If the

shooting function is satisfied, then this confirms the accuracy of the ROM at a given energy level without having to run the AMF algorithm on the full model. This shooting algorithm could be utilized in a model updating algorithm based on the energy dependent modal parameters to validate the full order, nonlinear finite element model with experimental NNMs.

This new model updating approach would provide insight into how each parameter of the FEA model affects the nonlinear dynamic response of the structure. The NNMs have an intimate connection to the forced response and can help guide specific design modifications to obtain the desired nonlinear response. For example, imagine that a structure is exposed to a large, random force that strongly excites frequencies near the first NNM. One could modify the characteristics of the first NNM in the energy range of interest with changes to the structural design to lower the overall response amplitudes and hence the stress fields that dictate the life of the structure.

## 8.3 Connection Between NNMs and Response Prediction

Nonlinear normal modes were used throughout this work to identify how changes to the reduced order model affected the dynamics of the resulting model. The frequency-energy curves gave qualitative insight into the ability of the model to capture the NNM(s) of the full order model, however the lack of superposition makes it difficult to find a quantitative connection. More work is needed to determine which NNMs must be accurate to compute responses due to various load environments (e.g. transient, random, etc...) and especially to establish a quantitative link between the accuracy of the NNMs and response metrics of interest. Recently, Ardeh [33] began to explore the role of NNMs in the reconstruction of a system's response through the development of connecting functions. His work could eventually lead to this quantitative connection but for now one should consider quantitative metrics based on the response while using the nonlinear modes to provide qualitative insight.

## Appendix – Publications of PhD work

### **Journal Papers**

- Kuether, R.J. and M.S. Allen, "A Numerical Approach to Directly Compute Nonlinear Normal Modes of Geometrically Nonlinear Finite Element Models," *Mechanical Systems and Signal Processing*, vol. 46, pp. 1-15, 2014.
- **Kuether, R.J.**, B.J. Deaner, J.J. Hollkamp, and M.S. Allen, "Evaluation of Geometrically Nonlinear Reduced Order Models with Nonlinear Normal Modes," *AIAA Journal*, (submitted).
- **Kuether, R.J.**, M.S. Allen, and J.J. Hollkamp "Modal Substructuring of Geometrically Nonlinear Finite Element Models," *AIAA Journal*, (submitted).
- **Kuether, R.J.**, M.S. Allen, and J.J. Hollkamp "Modal substructuring of geometrically nonlinear finite element models with interface reduction," *AIAA Journal*, (in preparation).
- Kuether, R.J., L. Renson, T. Detroux, C. Grappasonni, G. Kerschen, and M.S. Allen "Nonlinear Normal Modes, Modal Interactions, and Isolated Resonance Curves," *Journal of Sound and Vibration*, (submitted).

#### **Conference Papers**

- D.A. Ehrhardt, R. J. Kuether, and M. S. Allen, "Nonlinear Normal Modes in Finite Element
  Model Validation of Geometrically Nonlinear Flat and Curved Beams," in 56th AIAA/ASME/
  ASCE/AHS/ASC Structures, Structural Dynamics, and Materials Conference, Kissimmee, Florida,
  January 2015
- Kuether, R.J. and M.S. Allen, "Validation of Nonlinear Reduced Order Models with Time
   Integration Targeted at Nonlinear Normal Modes," in 33<sup>rd</sup> International Modal Analysis Conference
   (IMAC XXXIII), Orlando, Florida, February 2015
- L.C.M. Guerin, R.J. Kuether, and M.S. Allen, "Considerations for Indirect Parameter Estimation in Nonlinear Reduced Order Models," in 33<sup>rd</sup> International Modal Analysis Conference (IMAC XXXIII), Orlando, Florida, February 2015

- J. D. Schoneman, M. S. Allen, and R. J. Kuether, "Relationships between Nonlinear Normal Modes and Response to Random Inputs," in 55th AIAA/ASME/ASCE/AHS/ASC Structures, Structural Dynamics, and Materials Conference, National Harbor, Maryland, January 2014
- Kuether, R.J. and M.S. Allen, "Substructuring with Nonlinear Reduced Order Models and Interface Reduction with Characteristic Constraint Modes," in 55<sup>th</sup> AIAA/ASME/ASCE/AHS/ASC Structures, Structural Dynamics and Materials Conference (SDM), National Harbor, Maryland, January 2014
- Kuether, R.J. and M.S. Allen, "Craig-Bampton Substructuring for Geometrically Nonlinear Subcomponents," in 32<sup>nd</sup> International Modal Analysis Conference (IMAC XXXII), Orlando, Florida, February 2014
- **Kuether, R.J.**, M.R. Brake, and M.S. Allen, "Evaluating Convergence of Reduced Order Models Using Nonlinear Normal Modes," in 32<sup>nd</sup> International Modal Analysis Conference (IMAC XXXII), Orlando, Florida, February 2014
- Kuether, R.J. and M.S. Allen, "Nonlinear Modal Substructuring of Systems with Geometric Nonlinearities," in 54<sup>th</sup> AIAA/ASME/ASCE/AHS/ASC Structures, Structural Dynamics and Materials Conference (SDM), Boston, Massachusetts, April 2013
- Kuether, R.J. and M.S. Allen, "Structural Modification of Nonlinear FEA Subcomponents Using Nonlinear Normal Modes," in 31<sup>st</sup> International Modal Analysis Conference (IMAC XXXI), Garden Grove, California, February 2013
- Kuether, R.J. and M.S. Allen, "Computing Nonlinear Normal Modes Using Numerical Continuation and Force Appropriation," in ASME 2012 International Design Engineering Technical Conferences
   & Computers and Information in Engineering Conference (IDETC/CIE), Chicago, Illinois, 2012
- Allen, M.S., R.J. Kuether, B.J. Deaner and M.W. Sracic, "A Numerical Continuation Method to Compute Nonlinear Normal Modes Using Modal Coordinates," in 53<sup>rd</sup> AIAA/ASME/ASCE/AHS/ASC Structures, Structural Dynamics and Materials Conference (SDM), Honolulu, Hawaii, April 2012

Allen, M.S. and R.J. Kuether, "Substructuring with Nonlinear Subcomponents: A Nonlinear Normal Mode Perspective," in 30<sup>th</sup> International Modal Analysis Conference (IMAC XXX), Jacksonville, Florida, February 2012

### References

- [1] M. A. Crisfield, Nonlinear finite element analysis of solids and structures. Volume 1: Essentials. New York: John Wiley and Sons, 1991.
- [2] P. F. Pai and S. Y. Lee, "Non-linear structural dynamics characterization using a scanning laser vibrometer," *Journal of Sound and Vibration*, vol. 264, pp. 657-687, 2003.
- [3] P. F. Pai and A. H. Nayfeh, "A fully nonlinear theory of curved and twisted composite rotor blades accounting for warpings and three-dimensional stress effects," *International Journal of Solids and Structures*, vol. 31, pp. 1309-1340, 1994.
- [4] M. A. Crisfield, *Nonlinear finite element analysis of solids and structures. Volume 2: Advanced Topics*. New York: John Wiley and Sons, 1991.
- [5] P. B. Gonçalves, R. M. Soares, and D. Pamplona, "Nonlinear vibrations of a radially stretched circular hyperelastic membrane," *Journal of Sound and Vibration*, vol. 327, pp. 231-248, 2009.
- [6] R. A. Schapery, "An engineering theory of nonlinear viscoelasticity with applications," *International Journal of Solids and Structures*, vol. 2, pp. 407-425, 1966.
- [7] M. F. Beatty and Z. Ziliang, "Finite amplitude and free vibrations of a body supported by incompressible, nonlinear viscoelastic shear mountings," *International Journal of Solids and Structures*, vol. 27, pp. 355-370, 1991.
- [8] M. R. Brake, "A hybrid approach for the modal analysis of continuous systems with discrete piecewise-linear constraints," *Journal of Sound and Vibration*, vol. 330, pp. 3196-3221, 2011.
- [9] M. R. Brake, "The effect of the contact model on the impact-vibration response of continuous and discrete systems," *Journal of Sound and Vibration*, vol. 332, pp. 3849-3878, 2013.
- [10] D. P. Hess, A. Soom, and C. H. Kim, "Normal vibrations and friction at a Hertzian contact under random excitation: Theory and experiments," *Journal of Sound and Vibration*, vol. 153, pp. 491-508, 1992.
- [11] E. L. B. van de Vorst, D. H. van Campen, A. de Kraker, and R. H. B. Fey, "Periodic solutions of a multi-DOF beam system with impact," *Journal of Sound and Vibration*, vol. 192, pp. 913-925, 1996.
- [12] W. D. Iwan, "A Distributed-Element Model for Hysteresis and Its Steady-State Dynamic Response," *Journal of Applied Mechanics*, vol. 33, pp. 893-900, 1966.
- [13] D. J. Segalman, "A Four-Parameter Iwan Model for Lap-Type Joints," *Journal of Applied Mechanics*, vol. 72, pp. 752-760, September 2005.
- [14] W. Y. Tseng and J. Dugundji, "Nonlinear Vibrations of a Buckled Beam Under Harmonic Excitation," *Journal of Applied Mechanics*, vol. 38, pp. 467-476, 1971.

- [15] W. Lacarbonara, A. Nayfeh, and W. Kreider, "Experimental Validation of Reduction Methods for Nonlinear Vibrations of Distributed-Parameter Systems: Analysis of a Buckled Beam," *Nonlinear Dynamics*, vol. 17, pp. 95-117, 1998/10/01 1998.
- [16] K. D. Murphy, L. N. Virgin, and S. A. Rizzi, "Experimental snap-through boundaries for acoustically excited, thermally buckled plates," *Experimental Mechanics*, vol. 36, pp. 312-317, 1996.
- [17] R. Quiroz, J. Embler, R. Jacobs, G. Tzong, and S. L. Liguore, "Predictive Capability for Hypersonic Structural Response and Life Prediction: Phase II Detailed Design of Hypersonic Cruise Vehicle Hot-Structure," AFRL-RQ-WP-TR-2012-0265, Feburary 2012.
- [18] B. Zuchowski, "Predictive Capability for Hypersonic Structural Response and Life Prediction: Phase II Detailed Design of Hypersonic Cruise Vehicle Hot-Structure," AFRL-RQ-WP-TR-2012-0280, May 2012.
- [19] R. W. Gordon and J. J. Hollkamp, "Reduced-Order Models for Acoustic Response Prediction," AFRL-RB-WP-TR-2011-3040, Jul. 2011.
- [20] R. D. Blevins, I. Holehouse, and K. R. Wentz, "Thermoacoustic loads and fatigue of hypersonic vehicle skin panels," *Journal of Aircraft*, vol. 30, pp. 971-978, 1993.
- [21] A. J. Culler and J. J. McNamara, "Studies on Fluid-Thermal-Structural Coupling for Aerothermoelasticity in Hypersonic Flow," *AIAA Journal*, vol. 48, pp. 1721-1738, 2010.
- [22] A. J. Culler and J. J. McNamara, "Impact of Fluid-Thermal-Structural Coupling on Response Prediction of Hypersonic Skin Panels," *AIAA Journal*, vol. 49, pp. 2393-2406, 2011.
- [23] J. J. Hollkamp, R. W. Gordon, and S. M. Spottswood, "Nonlinear modal models for sonic fatigue response prediction: a comparison of methods," *Journal of Sound and Vibration*, vol. 284, pp. 1145-63, 2005.
- [24] M. P. Mignolet, A. Przekop, S. A. Rizzi, and S. M. Spottswood, "A review of indirect/non-intrusive reduced order modeling of nonlinear geometric structures," *Journal of Sound and Vibration*, vol. 332, pp. 2437-2460, 2013.
- [25] G. Kerschen, M. Peeters, J. C. Golinval, and A. F. Vakakis, "Nonlinear normal modes. Part I. A useful framework for the structural dynamicist," *Mechanical Systems and Signal Processing*, vol. 23, pp. 170-94, 2009.
- [26] Y. S. Lee, G. Kerschen, A. F. Vakakis, P. Panagopoulos, L. Bergman, and D. M. McFarland, "Complicated dynamics of a linear oscillator with a light, essentially nonlinear attachment," *Physica D: Nonlinear Phenomena*, vol. 204, pp. 41-69, 2005.
- [27] A. F. Vakakis, "Non-linear normal modes (NNMs) and their applications in vibration theory: an overview," *Mechanical Systems and Signal Processing*, vol. 11, pp. 3-22, 1997.
- [28] R. D. Cook, D. S. Malkus, M. E. Plesha, and R. J. Witt, *Concepts and Applications of Finite Element Analysis*, Fourth ed.: John Wiley and Sons, 2002.
- [29] R. M. Rosenberg, "Normal modes of nonlinear dual-mode systems," *Journal of Applied Mechanics*, vol. 27, pp. 263–268, 1960.
- [30] S. W. Shaw and C. Pierre, "Normal Modes for Non-Linear Vibratory Systems," *Journal of Sound and Vibration*, vol. 164, pp. 85-124, 1993.
- [31] H. A. Ardeh and M. S. Allen, "Instantaneous Center Manifolds and Nonlinear Modes of Vibration," presented at the ASME 2012 International Design Engineering Technical Conferences IDETC/CIE, Chicago, Illinois, 2012.

- [32] S. A. Neild and D. J. Wagg, Applying the method of normal forms to second-order nonlinear vibration problems vol. 467, 2011.
- [33] H. A. Ardeh, "Geometrical Theory of Nonlinear Modal Analysis," Ph.D Dissertation, University of Wisconsin-Madison, 2014.
- [34] M. Peeters, G. Kerschen, and J. C. Golinval, "Dynamic testing of nonlinear vibrating structures using nonlinear normal modes," *Journal of Sound and Vibration*, vol. 330, pp. 486-509, 2011.
- [35] M. Peeters, G. Kerschen, and J. C. Golinval, "Modal testing of nonlinear vibrating structures based on nonlinear normal modes: Experimental demonstration," *Mechanical Systems and Signal Processing*, vol. 25, pp. 1227-1247, 2011.
- [36] A. Cammarano, T. L. Hill, S. A. Neild, and D. J. Wagg, "Bifurcations of backbone curves for systems of coupled nonlinear two mass oscillator," *Nonlinear Dynamics*, vol. 77, pp. 311-320, 2014/07/01 2014.
- [37] R. J. Kuether and M. S. Allen, "Computing Nonlinear Normal Modes using Numerical Continuation and Force Appropriation," presented at the ASME 2012 International Design Engineering Technical Conferences IDETC/CIE, Chicago, Illinois, 2012.
- [38] R. J. Kuether, L. Renson, T. Detroux, C. Grappasonni, G. Kerschen, and M. S. Allen, "Nonlinear Normal Modes, Modal Interactions and Isolated Resonance Curves," *Journal of Sound and Vibration* (submitted), 2014.
- [39] A. F. Vakakis, L. I. Manevitch, Y. V. Mikhlin, V. N. Pilipchuk, and A. A. Zevin, *Nonlinear Modes and Localization in Nonlinear Systems*. New York: Wiley, 1996.
- [40] R. J. Kuether, M. R. Brake, and M. S. Allen, "Evaluating Convergence of Reduced Order Models Using Nonlinear Normal Modes," presented at the 32nd International Modal Analysis Conference (IMAC XXXII), Orlando, Florida, 2014.
- [41] J. D. Schoneman, M. S. Allen, and R. J. Kuether, "Relationships between Nonlinear Normal Modes and Response to Random Inputs," in *55th AIAA/ASME/ASCE/AHS/ASC Structures, Structural Dynamics, and Materials Conference*, National Harbor, MD, 2014.
- [42] H. A. Ardeh and M. S. Allen, "Investigating Cases of Jump Phenomena in a Nonlinear Oscillatory System," presented at the 31st International Modal Analysis Conference (IMAC XXXI), Garden Grove, California, 2013.
- [43] W. Lacarbonara, G. Rega, and A. H. Nayfeh, "Resonant non-linear normal modes. Part I: analytical treatment for structural one-dimensional systems," *International Journal of Non-Linear Mechanics*, vol. 38, pp. 851-872, 2003.
- [44] A. H. Nayfeh, *Introduction to perturbation techniques*. New York: Wiley, 1981.
- [45] A. H. Nayfeh and D. T. Mook, *Nonlinear Oscillations*. New York: John Wiley and Sons, 1979.
- [46] B. Cochelin and C. Vergez, "A high order purely frequency-based harmonic balance formulation for continuation of periodic solutions," *Journal of Sound and Vibration*, vol. 324, pp. 243-262, 2009.
- [47] J. C. Slater, "A numerical method for determining nonlinear normal modes," *Nonlinear Dynamics*, vol. 10, pp. 19-30, 1996.
- [48] R. Arquier, S. Bellizzi, R. Bouc, and B. Cochelin, "Two methods for the computation of nonlinear modes of vibrating systems at large amplitudes," *Computers & Computers & Computers*, vol. 84, pp. 1565-1576, 2006.

- [49] M. Peeters, R. Viguié, G. Sérandour, G. Kerschen, and J. C. Golinval, "Nonlinear normal modes, Part II: Toward a practical computation using numerical continuation techniques," *Mechanical Systems and Signal Processing*, vol. 23, pp. 195-216, 2009.
- [50] O. Brüls and P. Eberhard, "Sensitivity analysis for dynamic mechanical systems with finite rotations," *International Journal for Numerical Methods in Engineering*, vol. 74, pp. 1897-1927, 2008.
- [51] G. Kerschen, M. Peeters, J. C. Golinval, and C. Stephan, "Nonlinear normal modes of a full-scale aircraft," *AIAA Journal of Aircraft*, vol. 50, pp. 1409-1419, 2013.
- [52] M. S. Allen, R. J. Kuether, B. J. Deaner, and M. W. Sracic, "A Numerical Continuation Method to Compute Nonlinear Normal Modes Using Modal Coordinates," in *53rd AIAA/ASME/ASCE/AHS/ASC Structures, Structural Dynamics, and Materials Conference*, Honolulu, Hawaii, 2012.
- [53] R. J. Kuether and M. S. Allen, "A numerical approach to directly compute nonlinear normal modes of geometrically nonlinear finite element models," *Mechanical Systems and Signal Processing*, vol. 46, pp. 1-15, 2014.
- [54] J. H. Ginsberg, *Mechanical and Structural Vibrations: Theory and Applications*, 1st ed. New York: John Wiley and Sons, 2001.
- [55] T. L. Hill, A. Cammarano, S. A. Neild, and D. J. Wagg, "An Analytical Method for the Optimisation of Weakly Nonlinear Systems," presented at the 9th International Conference on Structural Dynamics EURODYN 2014, Porto, Portugal, 2014.
- [56] T. L. Hill, A. Cammarano, S. A. Neild, and D. J. Wagg, "Interpreting the Forced Response of a Two-Degree-of-Freedom Nonlinear Oscillator using Backbone Curves," *Journal of Sound and Vibration* (submitted), 2014.
- [57] M. Nash, "Nonlinear Structural Dynamics by Finite Element Modal Synthesis," in *Department of Aeronautics*, Ph.D. Dissertation, Imperial College, The University of London, 1977.
- [58] Y. Shi and C. Mei, "A finite element time domain modal formulation for large amplitude free vibrations of beams and plates," *Journal of Sound and Vibration*, vol. 193, pp. 453-464, 1996.
- [59] P. Tiso, E. Jansen, and M. Abdalla, "Reduction method for finite element nonlinear dynamic analysis of shells," *AIAA Journal*, vol. 49, pp. 2295-2304, 2011.
- [60] D. J. Segalman and C. R. Dohrmann, "A Method for Calculating the Dynamics of Rotating Flexible Structures, Part 1: Derivation," *Journal of Vibration and Acoustics*, vol. 118, pp. 313-317, 1996.
- [61] D. J. Segalman, C. R. Dohrmann, and A. M. Slavin, "A Method for Calculating the Dynamics of Rotating Flexible Structures, Part 2: Example Calculations," *Journal of Vibration and Acoustics*, vol. 118, pp. 318-322, 1996.
- [62] A. A. Muravyov and S. A. Rizzi, "Determination of nonlinear stiffness with application to random vibration of geometrically nonlinear structures," *Computers & Structures*, vol. 81, pp. 1513-1523, 2003.
- [63] J. J. Hollkamp, R. W. Gordon, and S. M. Spottswood, "Nonlinear Sonic Fatigue Response Prediction from Finite Element Modal Models: A Comparison with Experiments," in *44th AIAA/ASME/ASCE/AHS/ASC Structures, Structural Dynamics, and Materials Conference*, American Institute of Aeronautics and Astronautics, 2003.

- [64] R. J. Kuether, B. J. Deaner, J. J. Hollkamp, and M. S. Allen, "Evaluation of Geometrically Nonlinear Reduced Order Models with Nonlinear Normal Modes," *AIAA Journal* (submitted), 2014.
- [65] S. A. Rizzi and A. Przekop, "The Effect of Basis Selection on Static and Random Acoustic Response Prediction Using a Nonlinear Modal Simulation," NASA TP-2005-213943, 2005.
- [66] S. A. Rizzi and A. Przekop, "System identification-guided basis selection for reduced-order nonlinear response analysis," *Journal of Sound and Vibration*, vol. 315, pp. 467-485, 2008.
- [67] K. Kim, A. G. Radu, X. Q. Wang, and M. P. Mignolet, "Nonlinear reduced order modeling of isotropic and functionally graded plates," *International Journal of Non-Linear Mechanics*, vol. 49, pp. 100-110, 2013.
- [68] J. J. Hollkamp, R. W. Gordon, and S. M. Spottswood, "Nonlinear sonic fatigue response prediction from finite element modal models: a comparison with experiments," in *Proceedings of the 44th AIAA/ASME/ASCE/AHS/ASC Structures, Structural Dynamics, and Materials Conference*, 2003.
- [69] M. I. McEwan, J. R. Wright, J. E. Cooper, and A. Y. T. Leung, "A Combined Modal/Finite Element Analysis Technique for the Dynamic Response of a Non-linear Beam to Harmonic Excitation," *Journal of Sound and Vibration*, vol. 243, pp. 601-624, 2001.
- [70] J. J. Hollkamp and R. W. Gordon, "Reduced-order models for nonlinear response prediction: Implicit condensation and expansion," *Journal of Sound and Vibration*, vol. 318, pp. 1139-1153, 2008.
- [71] L. C. M. Guerin, R. J. Kuether, and M. S. Allen, "Considerations for Indirect Parameter Estimation in Nonlinear Reduced Order Models," presented at the 33rd International Modal Analysis Conference (IMAC XXXIII), Orlando, Florida, 2015.
- [72] R. Perez, X. Q. Wang, and M. P. Mignolet, "Nonintrusive Structural Dynamic Reduced Order Modeling for Large Deformations: Enhancements for Complex Structures," *Journal of Computational and Nonlinear Dynamics*, vol. 9, pp. 031008-031008, 2014.
- [73] D. de Klerk, D. J. Rixen, and S. N. Voormeeren, "General framework for dynamic substructuring: History, review, and classification of techniques," *AIAA Journal*, vol. 46, pp. 1169-1181, 2008.
- [74] R. R. J. Craig and A. J. Kurdila, *Fundamentals of Structural Dynamics*, 2nd ed. New York: John Wiley and Sons, 2006.
- [75] W. C. Hurty, "Dynamic analysis of structural systems using component modes," *AIAA Journal*, vol. 3, pp. 678-685, 1965/04/01 1965.
- [76] R. R. J. Craig and M. C. C. Bampton, "Coupling of Substructures for Dynamic Analysis," *AIAA Journal*, vol. 6, pp. 1313-1319, 1968.
- [77] J. R. R. Craig and C.-J. Chang, "On the use of attachment modes in substructure coupling for dynamic analysis," in *18th Structural Dynamics and Materials Conference*, ed: American Institute of Aeronautics and Astronautics, 1977.
- [78] S. Rubin, "Improved Component-Mode Representation for Structural Dynamic Analysis," *AIAA Journal*, vol. 13, pp. 995-1006, 1975/08/01 1975.
- [79] R. M. Hintz, "Analytical Methods in Component Modal Synthesis," *AIAA Journal*, vol. 13, pp. 1007-1016, 1975/08/01 1975.

- [80] R. H. MacNeal, "A hybrid method of component mode synthesis," *Computers & Structures*, vol. 1, pp. 581-601, 1971.
- [81] P. Blelloch and H. Vold, "Orthogonality and large models what's the problem?," presented at the 23rd International Modal Analysis Conference (IMAC XXXI), Orlando, FL, 2005.
- [82] M. P. Castanier, Y. Tan, and C. Pierre, "Characteristic Constraint Modes for Component Mode Synthesis," *AIAA Journal*, vol. 39, pp. 1182-1187, 2001.
- [83] D. M. Tran, "Component mode synthesis methods using interface modes. Application to structures with cyclic symmetry," *Computers & Structures*, vol. 79, pp. 209-222, 2001.
- [84] W. Witteveen and H. Irschik, "Efficient Mode Based Computational Approach for Jointed Structures: Joint Interface Modes," *AIAA Journal*, vol. 47, pp. 252-263, 2009/01/01 2009.
- [85] E. Budak and H. Nevzat Özgüven, "Iterative receptance method for determining harmonic response of structures with symmetrical non-linearities," *Mechanical Systems and Signal Processing*, vol. 7, pp. 75-87, 1993.
- [86] M. D. Cömert and H. N. Ozguven, "A Method for Forced Harmonic Response of Substructures Coupled by Nonlinear Elements," in *13th International Modal Analysis Conference (IMAC XIII)*, Nashville, Tennessee, 1995.
- [87] J. V. Ferreira and D. J. Ewins, "Nonlinear receptance coupling approach based on describing functions," in *14th International Modal Analysis Conference (IMAC XIV)*, Dearborn, MI, 1996.
- [88] J. V. Ferreira and D. J. Ewins, "Multi-harmonic nonlinear receptance coupling approach," in *15th International Modal Analysis Conference (IMAC XV)*, Orlando, FL, 1997, pp. 27-33.
- [89] T. Kalaycıoğlu and H. N. Özgüven, "Nonlinear structural modification and nonlinear coupling," *Mechanical Systems and Signal Processing*, vol. 46, pp. 289-306, 2014.
- [90] K. Watanabe and H. Sato, "Development of Nonlinear Building Block Approach," *Journal of Vibration, Acoustics, Stress, and Reliability in Design,* vol. 110, pp. 36-41, 1988.
- [91] P. Apiwattanalunggarn, S. W. Shaw, and C. Pierre, "Component mode synthesis using nonlinear normal modes," *Nonlinear Dynamics*, vol. 41, pp. 17-46, 2005.
- [92] Y. H. Chong and M. Imregun, "Coupling of non-linear substructures using variable modal parameters," *Mechanical Systems and Signal Processing*, vol. 14, pp. 731-746, 2000.
- [93] R. J. Kuether and M. S. Allen, "Nonlinear Modal Substructuring of Systems with Geometric Nonlinearities," in *54th AIAA/ASME/ASCE/AHS/ASC Structures, Structural Dynamics, and Materials Conference*, Boston, Massachusetts, 2013.
- [94] R. J. Kuether and M. S. Allen, "Structural Modification of Nonlinear FEA Subcomponents Using Nonlinear Normal Modes," presented at the 31st International Modal Analysis Conference (IMAC XXXI), Garden Grove, California, 2013.
- [95] R. W. Clough and E. L. Wilson, "Dynamic analysis of large structural systems with local nonlinearities," *Computer Methods in Applied Mechanics and Engineering*, vol. 17–18, Part 1, pp. 107-129, 1979.
- [96] H. D. Nelson, W. L. Meacham, D. P. Fleming, and A. F. Kascak, "Nonlinear Analysis of Rotor-Bearing Systems Using Component Mode Synthesis," *Journal of Engineering for Gas Turbines and Power*, vol. 105, pp. 606-614, 1983.

- [97] G. Verros and S. Natsiavas, "Ride Dynamics of Nonlinear Vehicle Models Using Component Mode Synthesis," *Journal of Vibration and Acoustics*, vol. 124, pp. 427-434, 2002.
- [98] W. S. Yoo and E. J. Haug, "Dynamics of Flexible Mechanical Systems Using Vibration and Static Correction Modes," *Journal of Mechanical Design*, vol. 108, pp. 315-322, 1986.
- [99] J. Becker and L. Gaul, "CMS Methods for Efficient Damping Prediction for Structures with Friction," presented at the 26th International Modal Analysis Conference (IMAC XXVI), Orlando, Florida, 2008.
- [100] F. Wenneker, "Component Mode Synthesis for geometrically nonlinear structures," MSc. Thesis, Delft University of Technology, 2013.
- [101] F. Wenneker and P. Tiso, "A Substructuring Method for Geometrically Nonlinear Structures," in *32nd International Modal Analysis Conference (IMAC XXXII)*, Orlando, Florida, 2014, pp. 157-165.
- [102] R. A. Perez, "Multiscale Reduced Order Models for the Geometrically Nonlinear Response of Complex Structures," Ph.D Dissertation, Arizona State University, 2012.
- [103] J. J. Hollkamp and R. W. Gordon, "Reduced-order models for nonlinear response prediction: Implicit condensation and expansion," *Journal of Sound and Vibration*, vol. 318, pp. 1139-1153, 2008.
- [104] R. J. Kuether and M. S. Allen, "Craig-Bamptom Substructuring for Geometrically Nonlinear Subcomponents," presented at the 32nd International Modal Analysis Conference (IMAC XXXII), Orlando, Florida, 2014.
- [105] R. J. Kuether, M. S. Allen, and J. J. Hollkamp, "Modal Substructuring of Geometrically Nonlinear Finite Element Models," *AIAA Journal* (submitted), 2014.
- [106] R. J. Kuether and M. S. Allen, "Substructuring with Nonlinear Reduced Order Models and Interface Reduction with Characteristic Constraint Modes," in *55th AIAA/ASME/ASCE/AHS/ASC Structures, Structural Dynamics, and Materials Conference*, National Harbor, MD, 2014.
- [107] R. J. Kuether, M. S. Allen, and J. J. Hollkamp, "Modal substructuring of geometrically nonlinear finite element models with interface reduction," *AIAA Journal* (in preparation), 2014.
- [108] R. W. Gordon, J. J. Hollkamp, and S. M. Spottswood, "Nonlinear response of a clamped-clamped beam to random base excitation," presented at the Eighth International Conference on Recent Advances in Structural Dynamics, University of Southampton, Southampton, UK, 2003.
- [109] D. Ehrhardt, R. Harris, and M. Allen, "Numerical and Experimental Determination of Nonlinear Normal Modes of a Circular Perforated Plate," presented at the 32nd International Modal Analysis Conference (IMAC XXXII), Orlando, Florida, 2014.
- [110] C. Grappasonni, J. P. Noel, and G. Kerschen, "Subspace and nonlinear-normal-modes-based identification of a beam with softening-hardening behaviour," presented at the 32nd International Modal Analysis Conference (IMAC XXXII), Orlando, Florida, 2014.
- [111] A. Przekop, X. Guo, and S. A. Rizzi, "Alternative modal basis selection procedures for reduced-order nonlinear random response simulation," *Journal of Sound and Vibration*, vol. 331, pp. 4005-4024, 2012.
- [112] X. Q. Wang, R. A. Perez, M. P. Mignolet, R. Capillon, and C. Soize, "Nonlinear reduced order modeling of complex wing models," in 54th AIAA/ASME/ASCE/AHS/ASC

- Structures, Structural Dynamics, and Materials Conference, Boston, Massachusetts, 2013.
- [113] D. J. Segalman, "Model reduction of systems with localized nonlinearities," *Transactions of ASME. Journal of Computational and Nonlinear Dynamics*, vol. 2, pp. 249-66, 2007.
- [114] R. W. Gordon and J. J. Hollkamp, "Reduced-Order Modeling of the Random Response of Curved Beams using Implicit Condensation," in 47th AIAA/ASME/ASCE/AHS/ASC Structures, Structural Dynamics, and Materials Conference, Newport, Rhode Island, 2006.
- [115] S. M. Spottswood, R. W. Gordon, and J. J. Hollkamp, "On the use of Reduced-Order Models for a Shallow Curved Beam under Combined Loading," in 49th AIAA/ASME/ASCE/AHS/ASC Structures, Structural Dynamics, and Materials Conference, Schaumburg, Illinois, 2008.
- [116] R. W. Gordon and J. J. Hollkamp, "Reduced-Order Models for Acoustic Response Prediction of a Curved Panel," in 52nd AIAA/ASME/ASCE/AHS/ASC Structures, Structural Dynamics, and Materials Conference, Denver, Colorado, 2011.
- [117] M. Nash, "Nonlinear Structural Dynamics by Finite Element Modal Synthesis," Ph.D Dissertation, Department of Aeronautics, Imperial College, 1977.
- [118] G. M. Reese, M. K. Bhardwaj, D. J. Segalman, K. F. Alvin, B. J. Driessen, K. Pierson, and T. Walsh, "Salinas: Users Notes," Sandia National Laboratory, Albuquerque, NM SAND1999-2801, 2005.
- [119] J. J. Hollkamp and R. W. Gordon, "Application of Reduced-Order Models for Thermoelastic Trajectory Simulation," in *53rd AIAA/ASME/ASCE/AHS/ASC Structures, Structural Dynamics, and Materials Conference*, Honolulu, Hawaii, 2012.
- [120] R. Perez, X. Wang, and M. P. Mignolet, "Nonlinear reduced-order models for thermoelastodynamic response of isotropic and functionally graded panels," *AIAA Journal*, vol. 49, pp. 630-641, 2011.
- [121] R. J. Kuether and M. S. Allen, "Validation of Nonlinear Reduced Order Models with Time Integration Targeted at Nonlinear Normal Modes," presented at the 33rd International Modal Analysis Conference (IMAC XXXIII), Orlando, Florida, 2015.